Analysis of the orbit determination data of Sentinel satellites for identification of Modeling Errors

ANALYSIS OF THE ORBIT DETERMINATION DATA OF SENTINEL SATELLITES FOR IDENTIFICATION OF MODELING ERRORS

in partial fulfilment of the requirements for the degree of

Master of Science

in Aerospace Engineering

at the Delft University of Technology, to be defended publicly on 20 May 2022.

By

Chinari Subhechha Subudhi

Student number: 5041767

Thesis supervisors: Prof.dr.ir. P.N.A.M. (Pieter) Visser and ir. W.J.F. (Wim) Simons

PREFACE

This Master's thesis is the result of the work conducted in the Astrodynamics and Space missions group of the Space Engineering department of TU Delft to fulfill the requirements of graduating from the MSc Aerospace Engineering, Spaceflight program at TU Delft. This research focused on improving the orbit solutions of Sentinel satellites computed at TU Delft by investigating for the sources of error in the Precise Orbit Determination.

It was a long journey to reach the completion of the thesis which was possible due to the help of several people along the way. I would like to extend my gratitude to my thesis supervisor, Wim Simons, for helping me gain an understanding of the topic and for providing constant support, guidance, and words of encouragement. I would like to thank Prof. Pieter Visser for providing his valuable insights that helped me greatly in the interpretation of the results of the data analysis. I would also like to thank my friends, flatmates, and family for their support and encouragement during the tough times of my thesis.

Chinari Subhechha Subudhi Delft, April 2022

ABSTRACT

The applications for which the data from Earth observation satellites can be used, is dependent on the precision and accuracy of the position of the satellite. Hence, precise orbit determination of satellites is crucial for the success of Earth observation satellites like the Sentinel family of satellites. TU Delft is an analysis center of the Copernicus precise orbit determination Quality Working Group and provides orbit solutions of Sentinel satellites for the external validation of the Sentinel orbits computed by the Copernicus Precise Orbit Determination Service. The GIPSYX/RTGx software is used for orbit determination using a reduced dynamic approach.

Existing research has focused on the overall accuracy of the orbit solutions to improve orbit accuracy. However, knowledge of the overall accuracy cannot provide much information about modeling errors. In this research, a data analysis approach was taken to aid the identification of the sources of errors in TU Delft's precise orbit determination strategy of the Sentinel satellites. From a thorough study of the precise orbit determination strategy, a set of parameters were selected for analysis, and a database was created for each satellite. Data analysis methods were customized to create a data analysis framework for the orbit determination data analysis. This framework was applied to the orbit determination data of Sentinel 1A, 1B, 2A, 2B, 3A, and 3B satellites, and the results were interpreted.

The two most common sources of error speculated were errors in the antenna phase center offset or phase center variations, and errors in the location of the center of mass of the satellite. Recommendations were issued regarding ways to confirm the error sources. A significant (> 95 %) correlation was observed between drag coefficient and geomagnetic activity index (Ap index) which shows the improper modeling of geomagnetic activity in the DTM2000 atmospheric density model.

CONTENTS

Pr	eface	•	V
Ał	ostra	ct	vii
Li	st of	Figures	хi
Li	st of	Tables	xiii
Gl	ossai	ry	xv
1	Intr	roduction	1
	1.2	Sentinel Satellites	1 3 5 6
2	2.1 2.2	Cise Orbit Determination Signal model	7 7 8 8 10
3	3.1	Parameter Selection for Data Analysis. 3.1.1 Creation of Database. Data Analysis methods 3.2.1 Univariate analysis. 3.2.2 Multivariate Analysis.	13 14 16 16 16 19
4	4.1	Univariate analysis	21 21 33 44 44 53 53
5	5.1 5.2	Univariate analysis conclusions Multivariate analysis conclusions Recommendations for future work	

x Contents

A Appendix 67

LIST OF FIGURES

1.1	Sentinel 1 (Credit: ESA)	2
1.2	Sentinel 2 (Credit: ESA/ATG MediaLab)	2
1.3	Sentinel 3 (Credit: ESA/ATG MediaLab)	3
3.1	Box-plot description (Source: Matplotlib documentation)	19
3.2	Violin plot as a combination of boxplot and Kernel Density estimate (Credit:	
	Eryk Lewinson, Violin plots explained)	20
4.1	Sentinel 1 code and phase time series plots	22
4.2	Sentinel 1 β angle, drag coefficient, and Solar Scale factor time series plots	23
4.3	Auto-correlation plots for the β angle, drag coefficient, and solar scale fac-	
	tor of Sentinel 1 satellites	23
4.4	Sentinel 1 empirical acceleration time series plots	25
4.5	Auto-correlation plots for the empirical acceleration of Sentinel 1 satellites	26
4.6	Sentinel 2 code and phase time series plots	27
4.7	Sentinel 2 β angle, drag coefficient, and Solar Scale factor time series plots	27
4.8	Auto-correlation plots for the β angle, drag coefficient, and solar scale fac-	
	tor of Sentinel 2 satellites	28
4.9	Sentinel 2 empirical acceleration time series plots	29
4.10	Auto-correlation plots for the empirical acceleration of Sentinel 2 satellites	30
	Sentinel 3 code and phase time series plots	31
	Sentinel 3 β angle, drag coefficient, and Solar Scale factor time series plots	32
4.13	Auto-correlation plots for the eta angle, drag coefficient, and solar scale fac-	
	tor of Sentinel 3 satellites	32
	Sentinel 3 empirical acceleration time series plots	34
	Auto-correlation plots for the empirical acceleration of Sentinel 3 satellites	35
	Box-plots and violin plots for % valid code measurements	36
	Box-plots and violin plots for % valid phase measurements	37
	Box-plots and violin plots for RMS of code residuals	38
	Box-plots and violin plots for RMS of phase residuals	39
	Box-plots and violin plots for drag coefficient	40
	Box-plots and violin plots for Solar Scale factor	41
	Box-plots and violin plots for Constant radial acceleration	42
	Box-plots and violin plots for Constant cross-track acceleration	43
	Box-plots and violin plots for Once-per-revolution sin C acceleration	44
	Box-plots and violin plots for Once-per-revolution cos C acceleration	45
	Box-plots and violin plots for Once-per-revolution sin L acceleration	46
4.27	Box-plots and violin plots for Once-per-revolution cos L acceleration	47

xii List of Figures

A.1	Periodgram plots for the β angle, drag coefficient, and solar scale factor of	
	Sentinel 1 satellites	67
A.2	Periodgram plots for the empirical acceleration of Sentinel 1 satellites	68
A.3	Periodgram plots for the β angle, drag coefficient, and solar scale factor of	
	Sentinel 2 satellites	69
A.4	Periodgram plots for the empirical acceleration of Sentinel 2 satellites	70
A.5	Periodgram plots for the β angle, drag coefficient, and solar scale factor of	
	Sentinel 3 satellites	71
A.6	Periodgram plots for the empirical acceleration of Sentinel 3 satellites	72

LIST OF TABLES

1.1	POD products accuracy requirement (Source-ESA)	4
4.1	Summary statistics of % of valid code measurements	36
4.2	Summary statistics of % of valid phase measurements	37
4.3		38
4.4	Summary statistics of RMS of phase residuals	39
4.5	Summary statistics of drag coefficient	40
4.6		41
4.7	Summary statistics of Constant radial acceleration	42
4.8	Summary statistics of Constant cross-track acceleration	43
4.9	Summary statistics of Once-per-revolution sin C acceleration	44
4.10	Summary statistics of Once-per-revolution cos C acceleration	45
4.11	Summary statistics of Once-per-revolution sin L acceleration	46
4.12	Summary statistics of Once-per-revolution cos L acceleration	47
4.13	Correlation of % valid code measurements with other parameters	48
4.14	Correlation of % valid phase measurements with other parameters	48
4.15	Correlation of RMS code residuals with other parameters	49
4.16	Correlation of RMS phase residuals with other parameters	50
4.17	Correlation of drag coefficient with other parameters	50
4.18	Correlation of solar scale factor with other parameters	51
4.19	Correlation of constant radial acceleration with other parameters	52
4.20	Correlation of constant cross-track acceleration with other parameters	52
4.21	Correlation of sin C acceleration with other parameters	53
4.22	Correlation of cos C acceleration with other parameters	54
4.23	Correlation of sin L acceleration with other parameters	54
4.24	Correlation of cos L acceleration with other parameters	55
4.25	Correlation of parameters of all Sentinel satellites when they repeat their orbits	55
4.26		56
	Correlation of parameters of A and B satellites when they cover the same	
	ground track.	57
A.1	Correlation matrix for Sentinel 1A	73
		74
A.3		75
A.4	Correlation matrix of Sentinel 2B	76
A.5		77
		78

GLOSSARY

AC Analysis Centre

AMR-C Advanced Microwave Radiometer for Climate

CoM Centre of Mass

CPOD Copernicus Precise Orbit Determination

DORIS Doppler Orbitography and Radiopositioning Inte-

grated by Satellite

ECMWF European Centre for Medium-Range Weather

Forecasts

ERP Earth Radiation Pressure ESA European Space Agency

ESOC European Space Operations Centre

EU European Union

EUMETSAT European Organisation for the Exploitation of Me-

teorological Satellites

GNSS Global Navigation Satellite System

GPS Global Positioning System

LEO Low Earth Orbit

LRA Laser Retroreflector Array
LRR Laser Retro-Reflector

MSI Multi-Spectral Instrument

NRT Near Real Time NTC Non Time Critical

OMI Ozone Monitoring Instrument

POD Precise Orbit Determination PRE Near Real Time Predicted

QWG Quality Working Group

xvi Glossary

RO	Radio Occultation
SAR SLR SPOT SRP STC	Synthetic Aperture Radar Satellite Laser Ranging Satellite Pour l'Observation de la Terre Solar Radiation Pressure Short Time Critical

TROPOMI TROPOspheric Monitoring Instrument

1

INTRODUCTION

1.1. SENTINEL SATELLITES

The European Union started the Earth Observation Programme, namely The Copernicus Programme, to monitor Earth and its atmosphere for the benefit of the citizens of Europe. This programme is funded, coordinated and managed by European Commission in partnership with the EU Member states, ESA, EUMETSAT, ECMWF, EU agencies and Mercator Océan. The programme aims to provide accurate, timely, and easily accessible information to improve the management of the environment, understand and mitigate the effects of climate change and ensure civil security (Source - ESA). It delivers data, information, and services using the satellite Earth observation data and in-situ (nonspace) data which are used for the purpose of land management, the marine environment, atmosphere, emergency response, security, and climate change. The services and data are open-source and are thus used by service providers, public authorities, and international organizations to improve the quality of life for citizens of Europe and around the world.

The satellite Earth observation data is obtained from the space component of the programme, which consists of a set of dedicated satellites - the Sentinel family, and contributing missions consisting of existing commercial and public satellites. The Sentinel satellites were specifically designed to meet the needs of the Copernicus programme.

The first mission of the Sentinel family is the Sentinel-1 which comprises two identical low-Earth polar-orbiting satellites, Sentinel-1A and Sentinel-1B, sharing the same orbital plane. Sentinel-1A was the first Sentinel satellite, launched on 3 April 2014, by a Soyuz rocket to a Sun-synchronous orbit of 693 km altitude. This was followed by the launch of Sentinel-1B on 25 April 2014. They carry a C-band Synthetic Aperture Radar (SAR) which operates on wavelengths not obstructed by cloud cover or lack of illumination and thus can acquire data both day and night time in all weather conditions. The SAR operates in four acquisition modes with different resolutions and coverage for different types of observation. For example, the Extra-Width swath imaging mode is used for maritime, ice, and polar zone operational services where wide coverage and short revisit times are demanded (Source - ESA).



Figure 1.1: Sentinel 1 (Credit: ESA)



Figure 1.2: Sentinel 2 (Credit: ESA/ATG MediaLab)

The Sentinel-2 mission consists of 2 identical satellites, Sentinel-2A and Sentinel-2B, in the same sun-synchronous low-Earth polar orbit, phased at 180°. The satellites carry the Multi-Spectral Instrument (MSI) which can acquire high-resolution multi-spectral images over 13 spectral bands. The MSI provides data for the next generation operational products like land-cover maps, land change detection maps, and geophysical variables. They also provide continuity of data obtained by the SPOT and Landsat series of satellites, thus contributing to Copernicus services and applications such as land management, agriculture, and forestry, disaster control, humanitarian relief operations, risk mapping, and security concerns (Source - ESA).

The Sentinel-3 mission consists of two low-Earth polar-orbiting satellites, Sentinel-3A and Sentinel-3B (Sentinel-3C and Sentinel-3D are yet to be launched), revolving around Earth in a sun-synchronous orbit at an altitude of about 800km. They carry Ocean and Land Colour Instrument (OLCI), Sea and Land Surface Temperature Instrument (SLSTR), SAR Radar Altimeter (SRAL), Microwave Radiometer (MWR) and a Precise Orbit Deter-



Figure 1.3: Sentinel 3 (Credit: ESA/ATG MediaLab)

mination (POD) package (DORIS, GNSS and LRR). The instruments measure sea-surface topography, sea and land surface temperature, and ocean and land surface color with high accuracy and reliability to support ocean forecasting systems, environmental monitoring, and climate monitoring. They also provide continuity in ERS, Envisat and SPOT vegetation data (Source - ESA).

The next in line was the Sentinel - 5 Precursor mission, launched on 13 October 2017 from the Plesetsk Cosmodrone in Russia. It revolves in a near-polar sun-synchronous orbit at an altitude of 824 km. It carries the Tropospheric Monitoring Instrument (TROPOMI), which is a passive grating imaging spectrometer. The main objective of the mission is to make atmospheric measurements with high Spatio-temporal resolution which will be used for monitoring and forecasting climate, air quality, ozone, and UV radiation. It reduces gaps in the availability of atmospheric data products between Aura mission (OMI) and future Sentinel satellites.

The Sentinel-6 mission shall include two satellites, Sentinel-6 Michael Freilich and Sentinel-6B, which will be launched 5 years apart. The first of the two, Sentinel-6 Michael Freilich was launched on a SpaceX Falcon 9 rocket from the Vanderburg Airforce Base, California on 21 November 2020. The satellite revolves in an orbit of inclination of 66 degrees and an altitude of 1336 km. Both the satellites will carry Poseidon-4 SAR radar altimeter, Advanced microwave radiometer for Climate (AMR-C), Global Navigation Satellite System - Radio Occultation (GNSS-RO), DORIS, and Laser Retroreflector Array (LRA). The objectives of the mission are to continue high precision ocean altimetry measurements and to collect high-resolution vertical profiles of temperature and humidity using GNSS RO sounding technique (Source - EUMETSAT).

1.2. Precise Orbit Determination

For the Earth observation missions, one of the factors that determine the accuracy of the instruments such as radars, radiometers, etc is the precision of the position of the satellite (instrument). For example, for mapping the land surface topography, the radar can only give the distance between the surface and the satellite. The position of the satellite dictates what part of the land is mapped and also the land topography with respect

Category	Latency	Orbit Accuracy
	Sentinel-1	
NRT Predicted (AUX_PREORB)	30 mins	1m (2D RMS 1-sigma)
NRT (AUX_REORB)	180 mins	10 cm (2D RMS 1-sigma)
NTC (AUX_POEORB)	20 days	5 cm (3D RMS 1-sigma)
	Sentinel-2	
NRT Predicted (AUX_PREORB)	90 mins before	10 m (2D RMS 3-sigma)
	ANX	
NRT (AUX_RESORB)	30 mins	3 m (3D RMS 1-sigma)
	Sentinel-3	
NRT - S3 POD IPF (SRROE_AX)	30 mins	10 cm radial RMS 1-sigma
		(target of 8 cm)
STC (AUX_MEORB)	1.5 days	4 cm radial RMS 1-sigma (tar-
		get of 3 cm)
NTC (AUX_POEORB)	28 days	3 cm radial RMS 1-sigma (tar-
		get of 2 cm)

Table 1.1: POD products accuracy requirement (Source-ESA)

to the center of Earth. Hence, POD is very crucial for these missions. A combination of POD and the instruments are needed to make accurate observations of the land, sea, and atmosphere of Earth.

The POD algorithms use precise Global Positioning System (GPS) / Global Navigation Satellite System (GNSS) ephemeris, GPS/GNSS observations of the satellite, satellite attitude measurements, and a few other observations depending on the method of POD used, for computing the precise position and velocity of the satellite. If the satellite also carries a DORIS receiver or LRA, the obtained orbit solutions can be independently validated with DORIS and Satellite Laser Ranging (SLR) observations.

The Copernicus Precise Orbit Determination (CPOD) Service, a part of the Copernicus Payload Data Ground Segment of the Sentinel missions, is a consortium led by GMV which is in charge of generating precise orbital products and other auxiliary data files that meet the accuracy and timeliness requirements.

For Sentinel-1, the CPOD products are divided into three categories - Near Real Time (NRT), Near Real Time Predicted (PRE) and Non Time Critical (NTC). Similarly, for Sentinel-2, the CPOD product categories are - NRT and PRE, and that for Sentinel-3 are - NRT, Short Time Critical (STC), and NTC. Each of these products have different timeliness and accuracy requirements for different missions. These requirements are given in Table 1.1. The Accuracy of the CPOD products in the given table are calculated by comparing it with the ESOC products.

The CPOD Quality Working Group (CPOD QWG) is a dedicated group of experts in POD that provide independent solutions for external validation of the POD products and research on improvising the algorithms and models for enhanced orbit solutions. Different Analysis centers (ACs) of the CPOD QWG are routinely computing orbit solutions for Sentinel-1A, 1B, 2A, 2B, 3A and 3B. The list of ACs include

- GMV (Grupo Mecánica del Vuelo, CPOD solution)
- AIUB (Astronomical Institute, University of Bern)
- CLS (Collecte Localisation Satellites)
- CNES (Centre National d'Etudes Spatiales)
- EUM (European Organisation for the Exploitation of Meteorological Satellites)
- DLR (Deutsche Zentrum f
 ür Luft- und Raumfahrt)
- ESOC (European Space Operations Center of ESA)
- GFZ (Deutsches GeoForschungsZentrum)
- JPL (Jet Propulsion Laboratory)
- TUM (Technical University of Munich)
- TUD (Delft University of Technology)

These institutions regularly provide independent orbit solutions for the Sentinel satellites. Every four months, a POD Service Review Report is released by GMV, which presents the methods used by the ACs and models compare the solutions with each other and with the combined solution generated from the orbit solutions of all ACs. For the case of Sentinel-3 satellites, a comparison with respect to SLR observations is also given in the report. These solutions are computed using different software packages and are based on the reduced-dynamic orbit determination approach. GPS data along with knowledge of the signal model and dynamic models of the satellite are used for the computation of solutions.

1.3. Research Questions and Objective

The accuracy of dynamic force models utilized for the orbit determination is one of the major factors that affect the precision of the computed orbits. To compare the accuracy of various combinations of force models, Hackel et al [1] state a comprehensive list of performance indicators.

1. Empirical accelerations and scaling parameters - The empirical accelerations estimated during the reduced-dynamic orbit determination approach are a measure for miss-modeled effects. These accelerations are computed in radial, along-track, and cross-track directions (in constant and once-per-revolution harmonics) for every fixed interval of time (every 10 minutes in the case of TU Delft POD of Sentinel satellites). Thus, its analysis can give information about the direction, and time variability of miss-modeled effects. Non-gravitational force models include a scaling parameter, like the Solar radiation scale factor for SRP, the Earth radiation scale factor for Earth Radiation Pressure, and the coefficient of drag for the atmospheric drag model, which are freely estimated in the reduced dynamic orbit determination approaches. The time variability of these parameters can be explained only by the effects not captured by the force models.

- 2. **Orbit overlaps** If arc length of 30 hours is used for orbit determination, the overlap of 6 hours between two consecutive days provides insights into internal consistency
- 3. **Satellite laser ranging** The SLR residuals, and the SLR-based orbit corrections over an extended data period, provide an external source of validation to assess the quality of orbits for satellites fitted with a laser retro-reflector.
- 4. **Radar Ranging** The radargrammetric distance measurements from the SAR instrument can also provide external validation of orbit quality.

The GPS data residuals can also be used for internal verification since it indicates the quality of the orbit [2]. For the orbits of Sentinel satellites, orbit validation can also be performed by comparing to CPOD Service orbits and those computed by the ACs of the CPOD OWG [3].

All the above-mentioned performance indicators provide insights into the overall orbit accuracy. However, to improve the individual force models, more information about the forces and effects the models are not able to capture is needed. This research focuses on assessing the quality and improving the dynamic model of the satellite. For satellites in low-Earth orbits (LEO), like the Sentinel satellites, the most dominant nonconservative force is the atmospheric drag [4]. One of the major factors influencing drag is solar activity Hence, this thesis will mainly focus on two of the non-conservative force models - Atmospheric drag and SRP.

The main objective of this thesis is to assess the quality of the TU Delft's orbit determination strategy, identify modeling errors, and provide recommendations for its improvement. This objective is split into the following sub-goals.

- Explore time series analysis strategies for analyzing the estimated forces and other
 parameters affecting them. Choose appropriate analysis methods and build a data
 analysis framework to be applied to Sentinel POD data.
- 2. Utilize the results of data analysis to infer from observed trends and obtain information about the effects not taken into account in the models.
- 3. Issue recommendations for improving orbit determination strategy of TU Delft, and for further analysis of the POD strategy.

1.4. OUTLINE

The report is organized as follows. Chapter 2 contains information about the signal and the dynamic models used in the state-of-the-art precise orbit determination strategies and gives an overview of the Sentinel orbit determination at TU Delft. Chapter 3 shows the process of selection of parameters for making a database and gives a detailed overview of the data analysis methods that are customized to analyze the orbit determination data. Chapter 4 contains the results of the analysis, their interpretation, and speculation about the possible sources of error. The chapter 5 concludes the report by taking up the most prominent observations of the analysis, forming hypotheses, and giving recommendations on the steps to be taken to confirm the presented hypothesis. It also contains a few recommendations for future work.

PRECISE ORBIT DETERMINATION

GipsyX/RTGx is the Jet Propulsion Laboratory's (JPL) next-generation software package that uses GNSS, GPS, SLR, and DORIS measurements for positioning, navigation, timing, and Earth science. It uses a Kalman filter approach to obtain a combined estimate of geodetic and geophysical parameters like station coordinates, satellite orbits, Earth orientation, ionospheric and tropospheric delays, etc. The software is also capable of full realization of a dynamic terrestrial reference through analysis and combination of time series of ground station coordinates [5].

The GPS range measurements to the Sentinel satellites are fit into a signal model with the help of precise satellite dynamics to obtain the precise position of the satellite.

2.1. SIGNAL MODEL

The code pseudo-range measurements are based on the pseudo-random-noise added to the transmitted radio signal. During the reception, the received signal is correlated to a PRN signal, with the same PRN number, generated by the receiver. The measured time delay between the two signals is recorded for the one-way range measurement. Because the PRN code repeats itself about once per millisecond and it is unknown which repetition is received, there exists an ambiguity of 293 km in the range. By combining the results of multiple satellites, this ambiguity can easily be solved, since it is much larger than the precision of the solution. Computed pseudo-range in GIPSYX/RTGx is given by [6]

$$R^C = c[(\tilde{t_3} - \bar{t_3}) + (\bar{t_3} - t_3) + (t_3 - t_2) + (t_2 - \bar{t_2}) + (\bar{t_2} - \tilde{t_2}) + B_R] + \rho_{trop} + \rho_{iono}$$
 (2.1)

where,

 $\tilde{t}_3 - \bar{t}_3$ = receiver clock error = receiver time tag receiver proper time,

 $\bar{t_3} - t_3$ = receiver proper time receiver coordinate time,

 $t_3 - t_2$ = receiver coordinate time transmitter coordinate time,

 $t_2 - \bar{t_2}$ = transmitter coordinate time transmitter proper time,

 $\bar{t}_2 - \tilde{t}_2 = \text{transmitter clock error} = \text{transmitter proper time transmitter time tag}$

 B_R = Bias term

c =speed of light

 ρ_{trop} = delay due to the troposphere

 ρ_{iono} = delay due to the ionosphere

In order to get more accurate range measurements, one can also track the phase of the carrier signal. Due to the short repeat pattern, this allows the precision is greatly improved. The modeled value for the carrier phase is the same as the modeled value for pseudo-range, except for the substitution of the carrier phase bias for the pseudo-range bias and the phase correction due to geometric misalignment between transmitter and receiver antennas [6]

$$P^{C} = c[(\bar{t}_{3} - \bar{t}_{3}) + (\bar{t}_{3} - t_{3}) + (t_{3} - t_{2}) + (t_{2} - \bar{t}_{2}) + (\bar{t}_{2} - \bar{t}_{2}) + B_{trn,rec}] + \frac{c}{\omega_{n}} \Delta \Phi_{geo} + \rho_{trop} + \rho_{iono}$$
(2.2)

where,

 $B_{trn,rec}$ = Carrier phase bias term ω_n = nominal transmission frequency and receiver mixing frequency

 $\Delta \Phi_{geo}$ = geometrical correction

2.2. DYNAMIC MODEL

To model the path of a satellite in orbit about the Earth, precise dynamic force models are implemented that include gravitational forces and surface forces on the satellite. Given the initial state (position and velocity at the initial epoch time) for the satellite and the model parameter values, the state can be propagated forward in time. Several models have been developed for determining the motion of satellites in Low Earth orbits since they are affected by various conservative and non-conservative forces on the satellite. These dynamic models shall be used along with the signal model for obtaining orbit solutions using parameter estimation methods.

2.2.1. FORCE MODELS

GIPSYX/RTGx includes the Earth's gravity field as a spherical harmonic expansion to arbitrary degree and order including time variability of these coefficients. Since Earth is not a perfect sphere, a perturbation of about three orders of magnitude smaller than the central gravity force needs to be considered. Gravitational perturbations are also

2.2. DYNAMIC MODEL 9

caused by forces exerted by the Sun and the Moon which is comparable to the perturbations caused due to Earth's oblateness. These lunisolar forces result in time-varying deformation of the solid body of the Earth, called solid Earth tides in addition to the ocean tides, which are also one of contributors to gravitational perturbations [7]. Other third body perturbations from bodies like Jupiter and Venus are much smaller than the perturbations caused by the Sun and the Moon. Hence, the gravitational force model consists of the Earth's gravity field as a spherical harmonic expansion to an arbitrary degree and order and includes the time variability of the coefficients, effects of solid Earth tides, ocean tides, atmospheric gravity, atmospheric tides, Pole tides and also perturbations from bodies like Sun, Moon and nearby planets to precisely model the gravitational forces acting on the satellites. The mass changes due to performing maneuvers are taken into account by implementing a Motor burn model that depends on the burn force vector, and the change in satellite mass due to the maneuver, assuming a constant burn rate for the whole duration.

The non-gravitational forces include atmospheric drag, solar radiation pressure, and Earth radiation pressure. All these forces are dependent on the model of the satellite. Various approaches have been implemented for modeling the satellite, ranging from purely empirical models based on in-orbit behavior to physical models based on structural analysis of the spacecraft. The coefficient of reflection can be different for the surfaces of different materials on board. Taking into account the two different types of reflection - specular and diffuse, is a complex task for purely physical satellite models. Deviations from nominal attitude, inaccurate knowledge of optical properties, and aging of the satellite surfaces lead to the inaccurate presentation of the real-orbit behaviour. The most commonly used are intermediate approaches between physical and empirical models, such as variations of the cannonball models and box wing models. In the case of the cannonball model, the whole satellite is considered to be a sphere, and is divided into sections based on different optical properties [8]. The box-wing model is a combination of flat plates arranged in the form of a box with a connected solar array [9]. Improvements on the traditional box wing model have been demonstrated in [10] and [11] that lead to higher accuracy in prediction.

Solar radiation pressure is a non-conservative force that creates perturbations at all times except during eclipses. This force depends on the surface area of the satellite exposed to sunlight. Hence, the model of the satellite and the accuracy with which the orientation of the satellite is obtained affect the accuracy of the force. Some of the models include the effects of solar eclipses. Though it increases the complexity, better accuracy is achieved. Various empirical models were developed by JPL ([12], [13]) and Centre for Orbit Determination in Europe, CODE ([14],[15]) for accurate representation of the SRP. Due to the differential heating of the components in a satellite, it experiences thermal self radiation that has drag-like characteristics. This effect is very small and is generally represented as a fraction of SRP and in the same direction as SRP [16].

The Sentinel satellites, being in LEO orbit, are highly affected by drag force caused due to the presence of the atmosphere. The drag force is directed opposite to the velocity of the satellite with respect to the atmospheric flux and thus results in the deceleration of the satellite. The main source of error in the drag model is the atmospheric density, which varies greatly with space and time because of complex interactions between so-

2

lar activity and the Earth's atmosphere and magnetic field. The varying altitude of the non-spherical satellites due to the atmospheric particle flux also leads to errors in drag models[7]. Jacchia L. G. [17] developed an empirical model for representing upper atmospheric variability based on satellite drag data. The MSIS model [18] was based on measurement of atmospheric composition by satellites and temperature measurements from the ground-based radars. The Air Force Space Battlelab's High Accuracy Satellite drag model (HASDM) [19] estimates a dynamically varying global density field using the Dynamic Calibration Atmosphere (DCA) algorithm, which solves for the diurnal and semi-diurnal variations of upper atmospheric density in real-time from the observed effects of drag on inactive payload and debris in the upper atmosphere region. The study by Colace et al [20] shows a comparison of the different atmospheric models - Jacchia 1971 [17], Naval Research Laboratory's NRLMSISE-00 [21] and JB2008 [22], the influence of solar variability on the models, and their impact on orbit solutions.

Earth Radiation pressure (ERP) is the consequence of solar flux being reflected and re-emitted from the Earth. It consists of two components - the short-wave optical radiation and the long-wave infra-red radiation. The optical radiation component has the same spectral distribution as SRP, but can be affected by the surface characteristics of Earth and cloud coverage. The infra-red radiation is the near isotropic re-emission of the solar radiation absorbed by Earth and its atmosphere [7]. Martin and Rubincam [23] show the Keplerian elements of the LAGEOS I satellite are significantly affected by Earth albedo. The orbital influence of the ERP, though small, is not negligible, particularly for high eccentricity satellites. The magnitude of the ERP should be approximately equal to 10% to 25% of the direct SRP for most satellites. At very low altitudes (200 to 300 km) the magnitude of ERP can be 35% of the direct solar pressure [24]. The reasons for the small magnitude are the non-isotropic albedo component of Earth being only 40%, the effectiveness of the radiation decreasing with increasing altitude, and a low altitude satellite seeing the earth's radiation coming from a large solid angle which leads to the cancellation of a large fraction of the horizontal momentum of the incident photons [25].

2.3. SENTINEL ORBIT DETERMINATION AT TU DELFT

TU Delft uses the GIPSYX/RTGx software for the precise orbit determination of Sentinel satellites using a reduced-dynamic approach. The Iono-free linear combinations of phase and pseudo-range GPS measurements every 30 seconds are fitted into a signal model (section 2.1) combined with high fidelity dynamical model of the spacecraft by an extended Kalman filter.

The EIGEN-GRGS.RL04.MEAN-FIELD with a linear mean pole is implemented as the gravity field model of Earth, including the effects of solid Earth tides, ocean tides, Earth and Ocean pole tides, and atmospheric gravity. The effects of solid Earth tides, the pole tide, and ocean tides are modeled as variations of harmonic coefficients of the Earth's geopotential. The third body gravitational perturbations (assuming point mass) from all planets of our solar system (and Pluto), the Earth and its Moon, are taken into account. GIPSYX/RTGx uses the latest publicly available JPL Planetary Ephemerides (DE421) to compute the position vector of the third bodies in inertial coordinates.

The Sentinel satellites are represented by the box-wing model in the orbit determination. The model has six planar surfaces that make up the spacecraft bus, and two planar components to describe the front and rear surfaces of the solar array. Each surface is specified with its area, specularity, diffusivity, and a unit normal vector. The box-wing model is used in conjunction with the component solar radiation pressure [26] model to compute the effects of solar radiation pressure on the Sentinel satellites. The contribution due to one of the flat surfaces of the Sentinel box-wing model is computed in the component solar radiation pressure model by the following equation [6].

$$F = -A\cos\theta \left[2\left(\frac{\delta}{3} + \rho\cos\theta\right)\hat{n} + (1-\rho)\hat{s} \right]$$
 (2.3)

where,

 $A = \text{panel area}(m^2)$

 \hat{n} = unit normal of the surface

 \hat{s} = unit vector from the plate to the Sun

 θ = the angle between the normal and source vectors

 δ = diffusivity

 ρ = specularity

For 6 surfaces, The equation for the acceleration due to Solar Radiation pressure is given by

$$\ddot{r} = -C_{\odot} f P_{\odot} \frac{1AU^2}{r_{\odot}^2} \frac{1}{m} \sum_{i=1}^{6} F_i$$
 (2.4)

where,

 C_{\odot} = Shadow factor, from the shadow model

f =Solar Radiation scale factor, referred to as solar scale factor

$$P_{\odot}$$
 = Solar Radiation pressure at 1AU $\left(\frac{Solar\,Constant}{Speed\,of\,Light} \approx 4.56X10^{-6}Nm^{-2}\right)$

 r_{\odot} = Distance between satellite and Sun

m =mass of satellite

GIPSYX/RTGx implements a shadow model, which uses the radii of the Sun, Earth, and Moon for conical shadowing with umbra and penumbra regimes. The Moon is modeled as a sphere and the Earth is modeled as an oblate spheroid. The shadow model computes the fraction of sunlight impinging on the satellite, which is called the shadow factor. The shadow factor is 1 when the vehicle is in clear view of the Sun, 0 during umbra, and varies between 0 and 1 during penumbra. This shadow model accounts for eclipses and thus improves the accuracy of the solar radiation pressure model.

The acceleration of the satellite (box-wing model) due to long-wave (LW) infra-red flux emitted by Earth, and the short-wave (SW) visible flux reflected from Earth is computed according to Knocke et al, 1988 [24]. The atmospheric drag (Sum of contributions of all 6 surfaces of the box-wing model of the satellite) is computed from the following equation.

$$a_{drag} = \frac{1}{2m} C_d \sum_{i=1}^{6} S_i \rho v_i^2 \hat{v}_i$$
 (2.5)

where, m is the mass of the satellite, C_d is the coefficient of drag estimated independently during the POD, S_i is the cross-sectional area of the i_{th} surface of the satellite determined by the attitude of the satellite, ρ is the atmospheric density obtained from an atmospheric density model, and v_i is the velocity vector of the i_{th} surface of the satellite relative to the atmosphere. The DTM2000 is used as an atmospheric density model for computing the atmospheric drag. The DTM2000 is a semi-empirical model that describes the temperature, density, and composition of the Earth's thermosphere.

Even the most precise force models are limited in their accuracy due to factors like imperfect non-conservative force models, uncertainty in the knowledge of satellite orientation, material properties, surface temperature, etc. Hence, empirical accelerations are implemented to account for unmodeled or miss-modeled forces. GIPSYX/RTGx allows the user to prescribe constant and once-per-revolution empirical accelerations along any of the spacecraft coordinate systems. At TU Delft, steady and once-per-revolution empirical accelerations in radial, cross-track, and along-track directions of the spacecraft are estimated.

EXPERIMENTAL SETUP

A detailed analysis of the solar radiation pressure and the drag force estimated during the orbit determination is the focus of this thesis. This chapter focuses on investigating the factors affecting the forces, exploring different data analysis methods, and building a framework for the analysis of the orbit determination of all Sentinel satellites.

The solar radiation pressure is mainly dependent on satellite mass, the surface area exposed to the Sun, solar flux reaching the satellite, eclipse conditions, and satellite surface material (reflectivity, diffusivity, and specularity) [7]. The satellite mass changes due to the execution of maneuvers. There is an uncertainty in the knowledge of the mass of the satellite due to the assumption of a constant burn rate, even though the maneuver start and stop time are perfectly known. Hence, this uncertainty affects the solar radiation pressure accuracy. The surface area exposed to the Sun is subject to uncertainties in the knowledge of satellite orientation and satellite physical model. Incident solar flux is dependent on atmospheric conditions (for LEO satellites), and solar activity, both of which are very difficult to model precisely. Solar activity can be deduced from $F_{10.7}$ cm flux, Mg II index, S_{10} index, solar flare data, and various other parameters. Uncertainties in eclipse conditions are due to neglecting the oblateness and atmosphere of the occulting body in the shadow model. The materials used in the construction of satellites are subject to changes in their reflectivity over time, and thus introduce uncertainties in impulse transfer due to absorption or reflection of sunlight.

Atmospheric drag modeling is very challenging due to three main reasons [7]. Firstly, the atmospheric density is not known very accurately. The modeling of complex dynamics and properties of the Earth's atmosphere is challenging. Secondly, modeling the drag force requires detailed knowledge of the interaction of the spacecraft surfaces with neutral gas and charged particles present in the atmosphere. The third reason is that the time-varying satellite orientation with respect to the atmospheric particle flux must be taken into account.

The constituents of the atmosphere vary with altitude which must be taken into account in the density model. Solar radiation influences atmospheric density. A diurnal variation in atmospheric density is observed due to the solar ultraviolet radiation heat-

ing, which also varies with the geographic latitude. The extreme ultraviolet radiation from the Sun has a short-term 27-day period due to rotation of the Sun and a long-term 11-year Sunspot cycle, whose effects can be accounted for by the 10.7 radiation index $(F_{10.7})$ measured in $W/m^2/s$. The corpuscular solar wind can cause short-term fluctuations in the atmospheric density. Geomagnetic storms occur due to variations in the solar wind that causes major disturbances in Earth's magnetosphere. This increases the temperature, and chemical constituency of the atmosphere, thus causing variations in atmospheric density.

The drag coefficient describes the interaction of spacecraft surface material with the atmosphere. Hence the drag coefficient depends on the molecular weight, the temperature of the impinging particles, and thus the chemical constituents of the atmosphere. Therefore, it is estimated freely in the orbit determination process.

3.1. PARAMETER SELECTION FOR DATA ANALYSIS

This section states the parameters that will be used for the analysis of the solar radiation pressure model and the atmospheric drag model, which is the focus of this thesis. These parameters are either representative of the factors affecting the two forces under investigation or are affected when there are unmodeled or miss-modeled errors.

 $F_{10.7}$ flux is the measurement of the total emission at a wavelength of 10.7 cm from all sources present on the solar disk, made over 1 hour. The wavelengths in the region of 10 cm are sensitive to conditions in the upper chromosphere and at the base of the corona, thus being an excellent indicator of solar activity [27]. Due to the elliptical orbit of the Earth around the Sun, the observed flux values are affected by the changing Sun-Earth distance. However, for our analysis, an indicator of solar activity is required, which should not ideally be affected by Earth-Sun distance. Hence, for our analysis, the adjusted $F_{10.7}$ flux [28] is used, which is the observed flux multiplied by the square of Earth-Sun distance in astronomical units.

The Mg II index is the daily measurement of the solar ultraviolet variability. It is a ratio of the irradiances, the average of three consecutive wavelength samples at the core of the unresolved Mg II h k doublet at 280 nm, and the average of two pairs of consecutive wavelengths equally spaced approximately 3 nm from the core wavelength. Since the Mg II index is the ratio of irradiances at nearby wavelengths, it is less prone to instrumental effects and long-term degradation [29]. Hence, it is one of the most valuable qualitative indices of solar activity used by astrophysicists and geophysicists. The Mg II index data is obtained from the Universität Bremen Satellite Data and Science Group [30].

 S_{10} index is an activity indicator of the integrated 26-34 nm solar irradiance measured by the Solar Extreme-ultraviolet Monitor (SEM) instrument on the NASA/ESA Solar and Heliospheric Observatory (SOHO) satellite. These irradiances represented by the S_{10} index are extreme ultraviolet line emissions dominated by the chromospheric He II line at 30.4 nm with contributions from other chromospheric and coronal lines. These photon emissions on reaching the Earth are observed in the thermosphere by atomic oxygen above 200 km altitude [31]. The S_{10} index data is obtained from the Archive of solar and geomagnetic indices for drag calculation by the Heliogeophysical Prediction Service Laboratory [32].

Sunspots are temporary phenomena on the photosphere of the Sun that appear vis-

ibly as dark spots compared to surrounding regions. They are caused by intense magnetic activity, which inhibits convection by an effect comparable to the eddy current brake, forming areas of reduced surface temperature. Rapid changes in the magnetic field alignment of sunspot groups' associated active regions are the most likely sources of significant space weather events such as solar flares, CMEs, radiations storms, and radio bursts. Sunspots are related to net energy retained by the planet. Fewer sunspots are associated with cooling, and more sunspots with warming [33]. The SESC sunspot number is computed according to the Wolf Sunspot number, R = k(10G + N), where G is the number of sunspot groups, N is the number of individual sunspots in all groups visible on the solar disk and k denotes a correction factor that compensates for differences in observational techniques and instruments used by the observers. The sunspot region information used to compute the daily sunspot number incorporates reports from as many as six observatories. These reports are used to form a composite picture of each individual region, including sunspot number, area, and classification, taking into account such factors as the time of observation and the quality of seeing. The SESC sunspot number data is obtained from the Space Weather Prediction Center [28].

The $F_{10.7}$ flux, Mg II index, S_{10} index and Sunspot number are strongly correlated with each other (Pearson correlation >0.7). The variables measure different aspects of solar activity and thus are all taken into account in the analysis.

Geomagnetic indices are a measure of geomagnetic activity, which is the response of the Earth's magnetosphere and ionosphere to solar forcing. They play a significant role in describing the magnetic configuration of the Earth's ionized environment. The K-index itself is a three-hour-long quasi-logarithmic local index of the geomagnetic activity at the given location and time compared to a calm day curve. A magnetometer measures the maximum deviation of the horizontal component of the magnetic field at its location and reports this. The global Kp-index is then determined with an algorithm that puts the reported K-values of every station together. The Kp-index ranges from 0 to 9 where a value of 0 means that there is very little geomagnetic activity and a value of 9 means extreme geomagnetic storming. Because of the non-linear relationship of the K-scale to magnetometer fluctuations (quasi-logarithmic), the average geomagnetic activity does not correspond to the average of a set of K-indices. Hence, every 3-hour K-value is converted back into a linear scale called the a-index, which is expressed in ap units (1ap = 2nT). The average from 8 daily a-values gives us the Ap index of a certain day. The Ap-index is thus a geomagnetic activity index where days with high levels of geomagnetic activity have a higher daily Ap-value. The Ap index values are obtained from the GFZ German Research Centre for Geosciences [34].

Coronal Mass Ejections (CMEs) can induce geomagnetic storms, which can have a more significant effect on Earth compared to a solar flare. CMEs produce a shock wave that can produce energetic particles as it travels through the interplanetary space. However, due to the unavailability of recent data for quantifying CMEs, they are not included in the analysis.

 β angle is the angle between the Earth-Sun Vector and the satellite orbit plane. According to the observations by Van den IJssel [35], the β angle was correlated with GPS residuals of GRACE-A orbits. Hackel et al [1] observe a correlation of the β angle with the scaling parameter of the solar radiation pressure for the TerraSAR-X satellite. The

observations will be carried out for the Sentinel satellite orbits computed at TUD to understand the necessity of modeling the effects of β angle in the dynamic model for orbit determination.

The constant and once-per-revolution empirical accelerations compensate for modeling errors. Hence, analysis of the empirical accelerations estimated during the orbit determination can give insights into the nature of the modeling error, which can be of help in determining the source of the errors.

GIPSYX/RTGx assumes a constant burn rate for maneuvers. Hence, the motor burn model has errors since a constant burn rate is not practical. There are uncertainties in knowledge of direction of thrust applied, change in mass, and orientation of the satellite, which leads to a sub-optimal estimation of maneuvers. Maneuvers are included in the analysis to investigate if they have a correlation with the quality of our estimates.

3.1.1. CREATION OF DATABASE

The orbits are estimated using the GIPSYX/RTGx software with the TU Delft configuration, for Sentinel 1A, 1B, 2A, 2B, 3A, and 3B for all days for which data is available. The orbit determination configuration for all satellites is kept the same (as given in section 2.3). All empirical accelerations are enabled except for the constant along-track acceleration.

The data obtained from the orbit determination in GIPSYX/RTGx was explored. Scripts were written to visualize the data for each day in the form of plots, to obtain additional data like the β and orbit angle of the satellite, to obtain daily weighed average and RMS of parameters, and to aggregate all the data into a single database for each satellite.

A database is created for each satellite with the following parameters sampled daily-date, percentage of phase, and code observations used in estimation (Code %, Phase %), GPS phase, and code RMS residuals for the estimation of the position of a day (RMS_C , RMS_P), drag coefficient (C_d), solar scale factor (f), the number of maneuvers during the day, β angle at 12 noon (β), 7 empirical acceleration values averaged over the day (constant and once-per-revolution accelerations in radial, cross-track, and along-track directions - H, C, L, sin C, cos C, sin L, cos L), $F_{10.7}$ flux, Mg II index, S_{10} index, and Ap index. Since the constant along-track empirical acceleration (L) estimation is switched off in the orbit determination configuration, its value remains 0.

3.2. Data Analysis methods

The analysis of the orbit determination is done by Exploratory data analysis, which is split into 2 parts - univariate, and multivariate analysis.

3.2.1. UNIVARIATE ANALYSIS

The important aspects of time series analysis are understanding the seasonality, trend, cyclicality, and randomness in the data. To look for seasonality, trends, and the cyclicality, time series, and auto-correlation plots will be made for the drag coefficient, solar-scale parameter, β angle, and the six empirical acceleration values of Sentinel 1A, 1B, 2A, 2B, 3A, and 3B.

The sample auto-correlation function r_k at lag k is given by [36]

$$r_k = \frac{\sum_{t=k+1}^n (X_t - \bar{X})(X_{t-k} - \bar{X})}{\sum_{t=1}^n (X_t - \bar{X})^2}$$
(3.1)

A plot of r_k vs k is called an autocorrelation plot or correlogram. It shows the degree of similarity of a time series with the lagged version of itself. If a high autocorrelation value (peak) is observed at regular lag intervals, it points to seasonality or cyclicality in the data.

The distribution of a quantitative variable can be characterized by its central tendency, spread, skewness, and kurtosis.

The two main measures of central tendency are mean, median, and mode. The arithmetic mean is the sum of all data values divided by the number of values. The median is the middle value after all values have been put in an ordered list. Mode is the most frequent value of the distribution. For symmetric distributions, the mean and median coincide. For asymmetric distributions, the mean is skewed towards the peak of the distribution. In symmetric unimodal distribution (single-peak), the mode equals both the mean and the median. In a skewed unimodal distribution, the mode and the median are on the two different sides of the mean. In a multimodal distribution, the highest mode is not well representative of the central tendency.

The spread of the data distribution is represented by the variance and standard deviation. The variance is the average of squares of individual deviations from the mean. The standard deviation is the square root of the variance. The higher the standard deviation, the bigger the spread of data.

Skewness is the measure of the asymmetry of the distribution. The skewness (g_1) of a dataset is given by

$$G_1 = \frac{m_3}{m_2^{3/2}} \tag{3.2}$$

where, m_3 is the third moment of dataset, and m_2 is the variance. Since we only have a sample of the whole population of dataset, sample skewness (G_1) is computed [37].

$$G_1 = \frac{\sqrt{n(n-1)}}{(n-2)}g_1 \tag{3.3}$$

where n is the sample size. A unimodal distribution is said to positively skewed (skewed right), if the right tail of the distribution is longer than the left. If the skewness is less than -1 or greater than 1, the distribution is said to be highly skewed. A distribution is moderately skewed if the skewness is between -1 and -1/2 or between 1/2 and 1. For skewness values between -1/2 and 1/2, the distribution is approximately symmetric.

The database is just a sample of the whole population. The sample can be skewed even if the population is actually symmetric. Hence, the test statistic(Z_{G_1}) is calculated [37].

$$Z_{G_1} = \frac{G_1}{SES} \tag{3.4}$$

$$Z_{G_1} = \frac{G_1}{SES}$$
 (3.4)
 $SES = \sqrt{\frac{6n(n-1)}{(n-2)(n+1)(n+3)}}$

where, SES is the Standard error of Skewness. If Z_{G_1} is less than -2, the population is very likely to be skewed negatively. If Z_{G_1} is greater than 2, the population is very likely to be skewed positively. If Z_{G_1} is between -2 and 2, you cannot reach any conclusion about the skewness of the population.

Kurtosis is a measure of the height and sharpness of the peak with respect to the rest of the data. The excess kurtosis (g_2) is computed in the following way.

$$g_2 = \frac{m_4}{m_2^2} - 3 \tag{3.6}$$

where, m_4 is the fourth moment of dataset. Since we only have a sample of the whole population of dataset, sample excess kurtosis (G_2) is computed [37].

$$G_2 = \frac{n-1}{(n-2)(n-3)}[(n+1)g_2 + 6]$$
(3.7)

A normal distribution has an excess kurtosis of 0 and is called a mesokurtic distribution. If the kurtosis is negative, it is called a platykurtic distribution and its central peak is lower and broader, and its tails are thinner compared to a normal distribution. A distribution with positive kurtosis has a higher and sharper central peak with fatter tails compared to the normal distribution and is called a leptokurtic distribution.

Since the database is just a sample of the whole population, even though the population is a normal distribution, the sample excess kurtosis may be non-zero. Hence, the test statistic (Z_{G_2}) is computed [37].

$$Z_{G_2} = \frac{G_2}{SEK} \tag{3.8}$$

$$Z_{G_2} = \frac{G_2}{SEK}$$
 (3.8)
 $SEK = 2(SES)\sqrt{\frac{n^2 - 1}{(n-3)(n+5)}}$ (3.9)

where SEK is the Standard error of Kurtosis. If Z_{G_2} is less than -2, it is very likely for the population to have a negative excess kurtosis. If Z_{G_2} is more than 2, the population has a good likelihood of having positive excess kurtosis. If Z_{G_2} is between -2 and 2, no conclusion can be reached about the kurtosis of the population.

The mean, median, standard deviation, sample skewness, test statistic of sample skewness, sample kurtosis, and test statistic of sample kurtosis will be calculated for the GPS code and phase residuals, drag coefficient, solar-scale parameter, β angle, and the six empirical acceleration values of Sentinel 1A, 1B, 2A, 2B, 3A, and 3B.

The statistics of the distribution of the parameters in the dataset give a quantitative and objective view. In addition to it, we look into the distribution graphically to get the full picture of the data and analyze it subjectively.

The boxplot is a way of displaying the dataset based on five numbers - Minimum, Maximum, Medium, First quartile, and third quartile. The figure 3.1 shows the details of the box-plot representation. The box extends from the first quartile (Q1) to the third quartile (Q3) of the data, with a line at the median. The whiskers extend from the box by 1.5x the interquartile range (IQR). Flier points are those past the end of the whiskers. Minimum is the smallest data point. Maximum is the largest data point. The Median

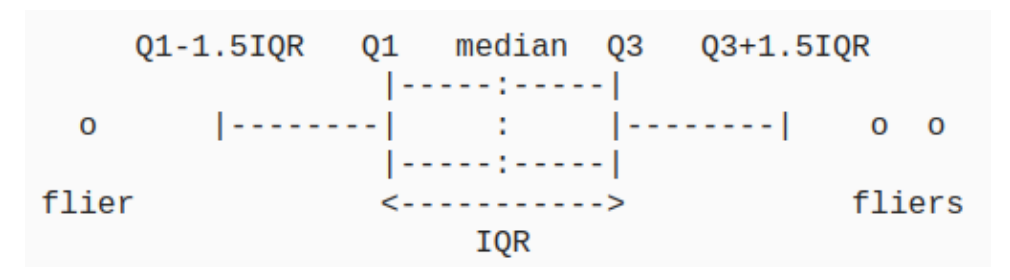


Figure 3.1: Box-plot description (Source: Matplotlib documentation)

is the middle value of the ordered list of data. The first quartile is the middle number between the minimum and the median. The third quartile is the middle value between the median and the maximum. Boxplots give a good representation of central tendency, symmetry, skewness, and outliers (fliers) but can be misleading on multi-modality.

Violin plots are a combination of the box plot and the kernel density estimate as shown in figure 3.2. It shows the descriptive statistics and the distribution of each variable. The white dot represents the mean, the thick black bar represents the interquartile range (25-75 percentile), and the thin black bar represents the rest of the distribution excluding the outliers. Since the violin plot shows the full distribution of the variable in addition to the statistical variables, it is more informative than a box plot.

The box plots and violin plots are made for the GPS code and phase residuals, drag coefficient, solar-scale parameter, and the six empirical acceleration values (constant along-track empirical acceleration estimate is disabled in the orbit configuration) of Sentinel 1A, 1B, 2A, 2B, 3A, and 3B.

3.2.2. MULTIVARIATE ANALYSIS

The statistic that is of interest in the case of multiple variable analysis is the sample correlation and sample correlation matrices. The sample correlation between two variables *X* and *Y* can be computed in the following way.

$$Cor(X,Y) = \frac{\sum_{i=1}^{n} (x_i - \bar{x})(y_i - \bar{y})}{\sqrt{\sum_{i=1}^{n} (x_i - \bar{x})^2} \sqrt{\sum_{i=1}^{n} (y_i - \bar{y})^2}}$$
(3.10)

The correlation is always between -1 and 1, with 1 corresponding to perfect positive correlation, 0 to no correlation in the sample, and -1 to perfect negative correlation. Correlation is the representation of the degree of linear relationship between two variables.

It is important to compute the significance of the correlation coefficients to ensure that the computed correlations are not a result of random variation. Hence, the correlations and the 2-tailed tests of significance are performed in the software IBM SPSS Software.

The concept of correlation is applied to the orbit determination analysis in several ways.

The first type of correlation analysis performed is the correlation between different parameters for one satellite. The correlation matrix is calculated for GPS code and phase

Standard Normal Distribution Histogram + KDE Boxplot Violin plot

Figure 3.2: Violin plot as a combination of boxplot and Kernel Density estimate (Credit: Eryk Lewinson, Violin plots explained)

residuals, drag coefficient, solar scale parameter, β angle, constant radial, and cross-track empirical accelerations, the four once-per-rev accelerations, $F_{10.7}$ flux, Mg II index, S_{10} index, SESC sunspot number, and Ap index for all the Sentinel satellite orbit determination data.

Each Sentinel satellite has a repeat orbit and traces the same ground track after every fixed amount of time. The third type of correlation analysis would be correlating the parameters when the satellites trace the same ground track. The objective of this analysis is to confirm what parameters are dependent on the relative position of the satellite with respect to Earth.

Sentinel missions have pairs of identical satellites, each in the same orbit but some phase apart. For example, the Sentinel 1A and 1B are identical satellites in a sun-synchronous 98.6 minute period, 12-day repeat orbit of 98.18 degree inclination, and 693 km altitude. The 1A and 1B satellites are at 180 degree phase separation. Hence, in the second type of correlation analysis, the parameters of satellite A will be correlated with the parameters of satellite B. This analysis is further sub-divided into two parts - correlation of parameters of two satellites of the same day, and correlation of parameters when satellite B traverses the same ground track as satellite A.

DATA ANALYSIS

4.1. Univariate analysis

In this analysis, the nature of each of the parameters in our database is investigated. The first part of the univariate analysis is the time series and auto-correlation plots of each of the parameters of the satellite. This is followed by an analysis to obtain the statistical distribution of parameters. The mean, median, mode, skewness, and kurtosis are calculated for each of the parameters of all the Sentinel satellites and their distribution is visualized with box plots and violin plots.

4.1.1. TIME SERIES ANALYSIS

Time series and auto-correlation plots for the various parameter in the database for the Sentinel satellites have been plotted for analysis. The missing orbit determination data is filled in with the average parameter value of the day before and after. A one-dimensional n-point Discrete Fourier Transform is performed on the auto-correlation values to obtain the periodogram which will give quantitative information on the periodicity of the parameters, the plots of which are given in the Appendix A.

The time series plots give information about the general trend, periodic variations if any, and the outliers in the parameters. Reasons for the trend, periodic variation, and outliers if observed are speculated. The periodic variations observed are further confirmed by auto-correlation plots.

SENTINEL 1

The percentage of code and phase measurements used in the orbit determination for Sentinel 1A and 1B appear to be correlated. The amount of valid code and phase measurements show smaller variations after mid of 2016 for Sentinel 1A. Therefore, in analyses, only the data from the year 2016 have been taken into account. An outlier is observed on day 108 of 2019 for the % code and phase observations of both Sentinel 1A and 1B satellites as shown in figure 4.1, which will be investigated later.

The RMS of code and phase residuals for both satellites appear to follow similar trends, which is clear from the figure 4.1. On day 336 of 2021, a spike in the RMS of

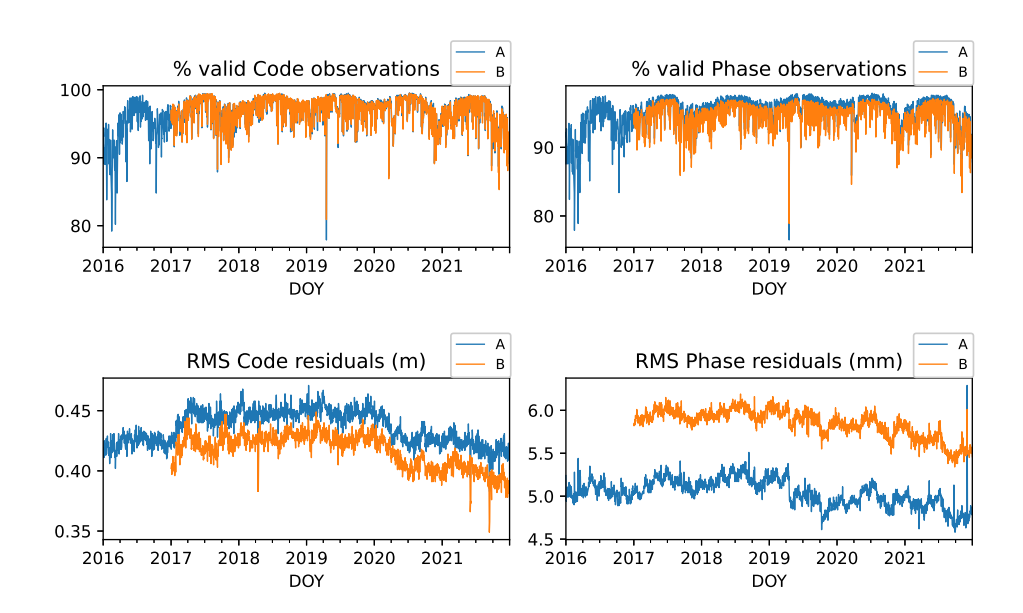


Figure 4.1: Sentinel 1 code and phase time series plots

phase residuals is observed. The code residuals of Sentinel 1B are smaller compared to Sentinel 1A. However, the phase residuals are smaller for Sentinel 1A. The accuracy of the GPS antenna phase center with respect to the Center of Mass (CoM) location affects the modeling of carrier phase observations and thus influences the carrier and phase residuals[38]. Thus, a potential cause of the constant bias in the residuals of Sentinel 1A and 1B could be due to erroneous nominal phase center offset provided by the manufacturer.

Figure 4.2 shows the time series plots for β angle, drag coefficient, and the solar scale factor for Sentinel 1A and 1B. The β angle for satellites 1A and 1B are almost the same, since both the satellite are in the same orbit, and thus have the same orbital plane. The drag coefficient and solar scale factor show a strong correlation for both satellites (strength of the correlation is quantified in the section 4.2.3). The plots 4.3 show the periodic components in β angle, drag coefficient and the solar scale factor. The β angle and drag coefficient show periodicity of 182.5 and 365 days and a small periodic component of 121.7 days. The solar scale factor shows a periodicity of 121.7 and 365 days and small periodic components of 182.5 and 91.25 days.

Figure 4.4 shows the time series plots of the empirical accelerations of Sentinel 1A and 1B. The empirical accelerations for the 2 satellites have a strong correlation, the strength of which is quantified in section 4.2.3.

The constant empirical accelerations of Sentinel 1B are observed to have a smaller number of outliers compared to the Sentinel 1A. The days 256 of 2018, 108 of 2019, and 336 of 2021 are significant outliers (greater than 10 sigmas) in the constant radial acceleration plot of Sentinel 1A. On day 256 of 2018, two maneuvers were performed by

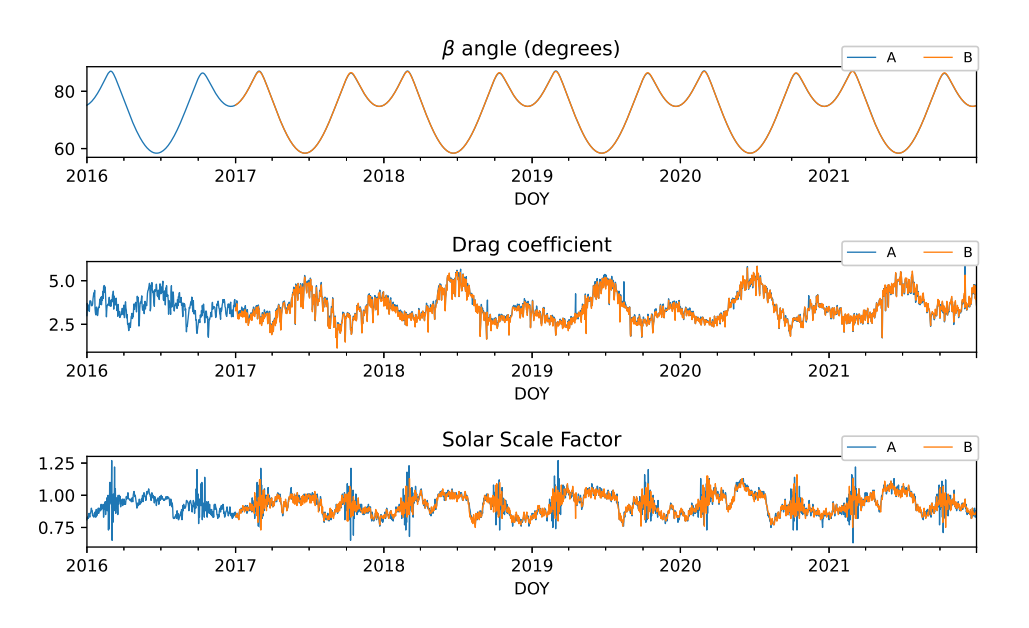


Figure 4.2: Sentinel 1 β angle, drag coefficient, and Solar Scale factor time series plots

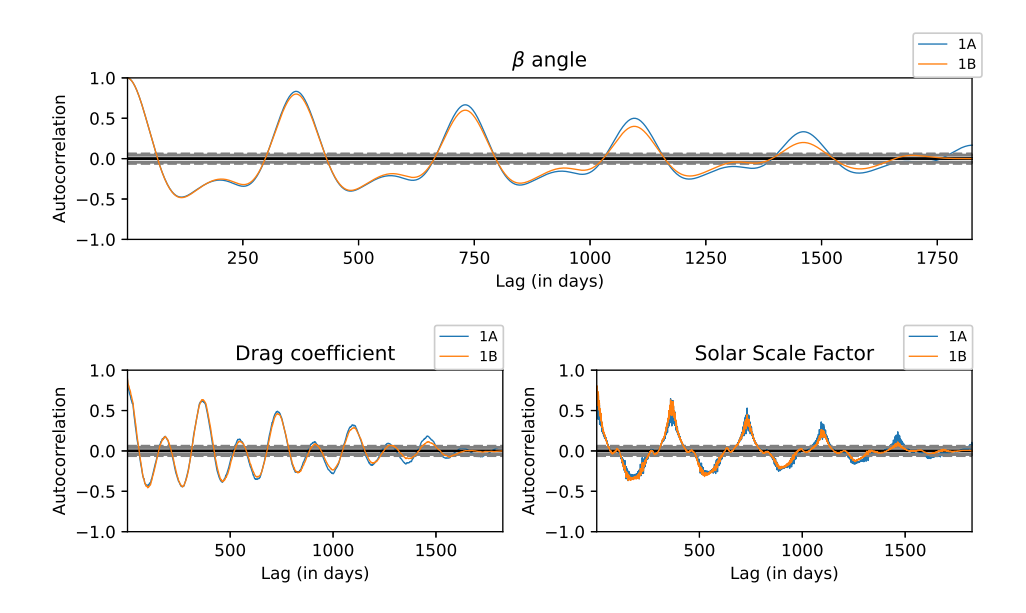


Figure 4.3: Auto-correlation plots for the β angle, drag coefficient, and solar scale factor of Sentinel 1 satellites

Sentinel 1A. The possible reason for the high radial empirical acceleration could be that GIPSYX/RTGx was not able to estimate the maneuvers accurately, which resulted in the error being absorbed by the constant radial empirical acceleration. Day 108 of 2019 contains a small percentage of valid code and phase measurements that were used for the orbit determination (77.9% code and 76.5% phase measurements were usable), which lead to a less optimal estimate of the satellite position. The sub-optimal estimate was compensated by the increased magnitude of the radial empirical acceleration. Day 336 of 2021 reports a relatively high RMS of phase residual (6.29 mm), a less than ideal percentage of valid phase measurements used for the orbit determination (89.8 %), and the execution of two maneuvers of the Sentinel 1A, the compound effect of which might have resulted in the dramatically big constant radial acceleration value of 151.7 nm/s^2 . A similarly dramatic high value of the constant radial acceleration on day 336 of 2021 is also observed in Sentinel 1B which can be attributed to similar causes - RMS phase residual of 6.01 mm, 92.4 % phase measurements used in orbit determination, and the execution of two maneuvers.

The periodicity of the empirical accelerations can be deduced from the figure 4.5. The constant radial acceleration shows a periodicity of 182.5 and 365 days. The constant cross-track acceleration shows a periodic variation of 365 days. In the case of the onceper-rev empirical accelerations, sin C shows a periodicity of 182.5 and 365 days, cos C of 14.7, 182.5, and 365 days, and the sin L and cos L of 121.7 (small component), 182.5 and 365 days.

SENTINEL 2

Figure 4.6 shows the percentage of code and phase measurements used in the orbit determination for Sentinel 2 satellites, and the RMS of the code and phase residuals after the position estimation. The percentage of code and phase measurements used appear to be correlated for the two satellites, but the correlation is weaker compared to the Sentinel 1 satellites, mainly in the year 2020. The RMS of the code and phase residuals follow similar trends in Sentinel 2A and 2B, except for the year 2020, which can be attributed to the uncorrelated percentage of valid code and phase measurements. The phase residuals of Sentinel 2B are smaller and have a constant bias from those of Sentinel 2A. This can be due to the error in nominal phase center offset, as in the case of Sentinel 1 satellites. On day 330 of 2019, the figure shows a very low percentage of phase residuals (36%) used for the orbit determination of Sentinel 2B. No outliers were observed in $F_{10.7}$ flux, Mg II index, S_{10} index, sunspot number, Ap index, or the number of solar flares for that day. A corresponding spike in RMS of code (0.54 m) and phase (8.25 mm) residuals are observed on the same day since the low amount of measurements is not enough to make an accurate position estimate of the satellite.

The time series plots of β angle, drag coefficient, and the solar scale factor for Sentinel 2A and 2B are shown in the figure 4.7. The β angle for Sentinel 2A and 2B are almost equal (except for the small variation due to uncertainty in deployment) as expected since they revolve in the same orbit. The drag coefficient and the solar scale factor for Sentinel 2A and 2B have a strong correlation (strength of the correlation is quantified in section 4.2.3). The β angle, drag coefficient, and solar scale factor show periodic variations of 182.5 and 365 days, which can be observed in the auto-correlation plots given in figure 4.8. The solar scale factor also has a small periodic component of 58 days.

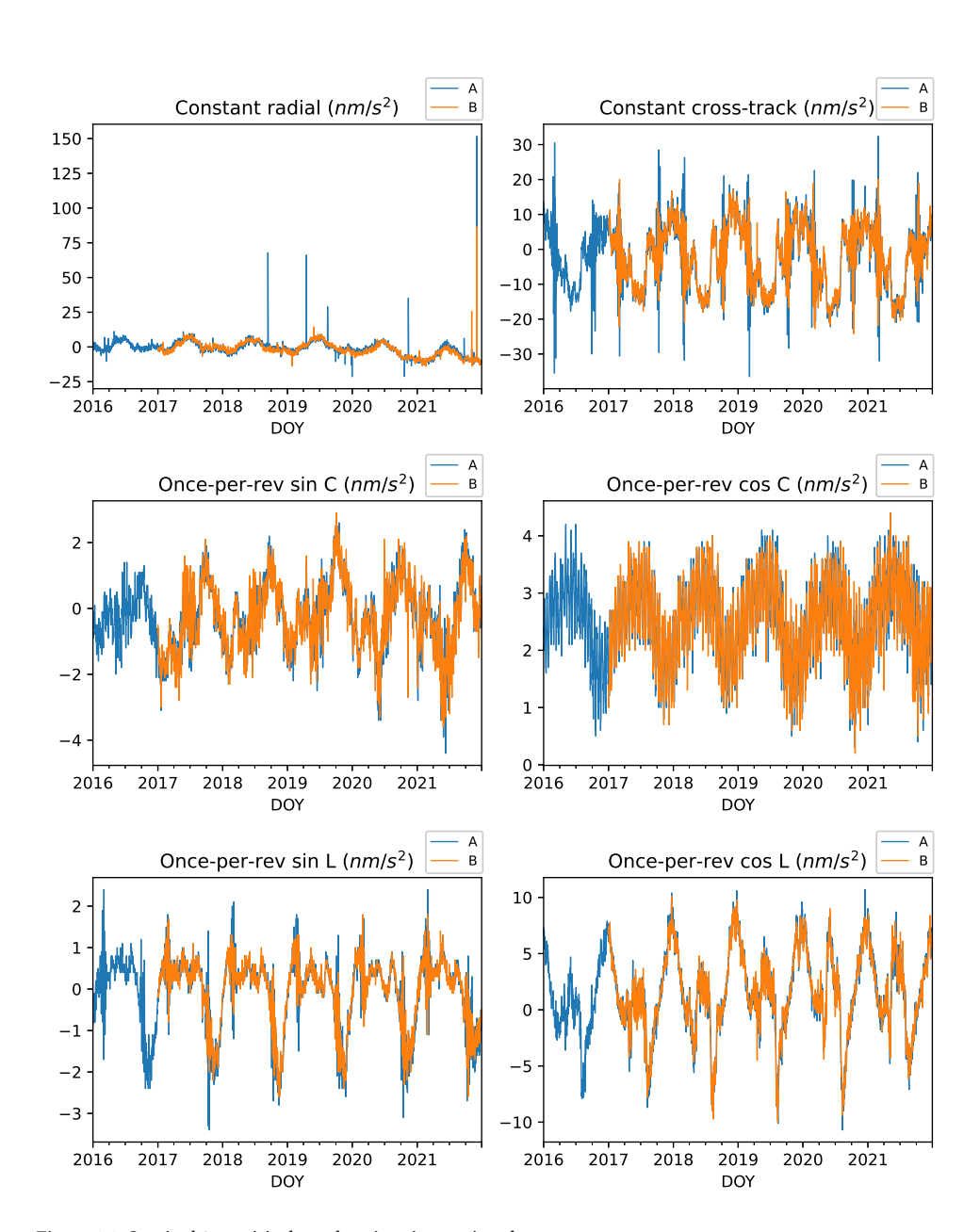


Figure 4.4: Sentinel 1 empirical acceleration time series plots

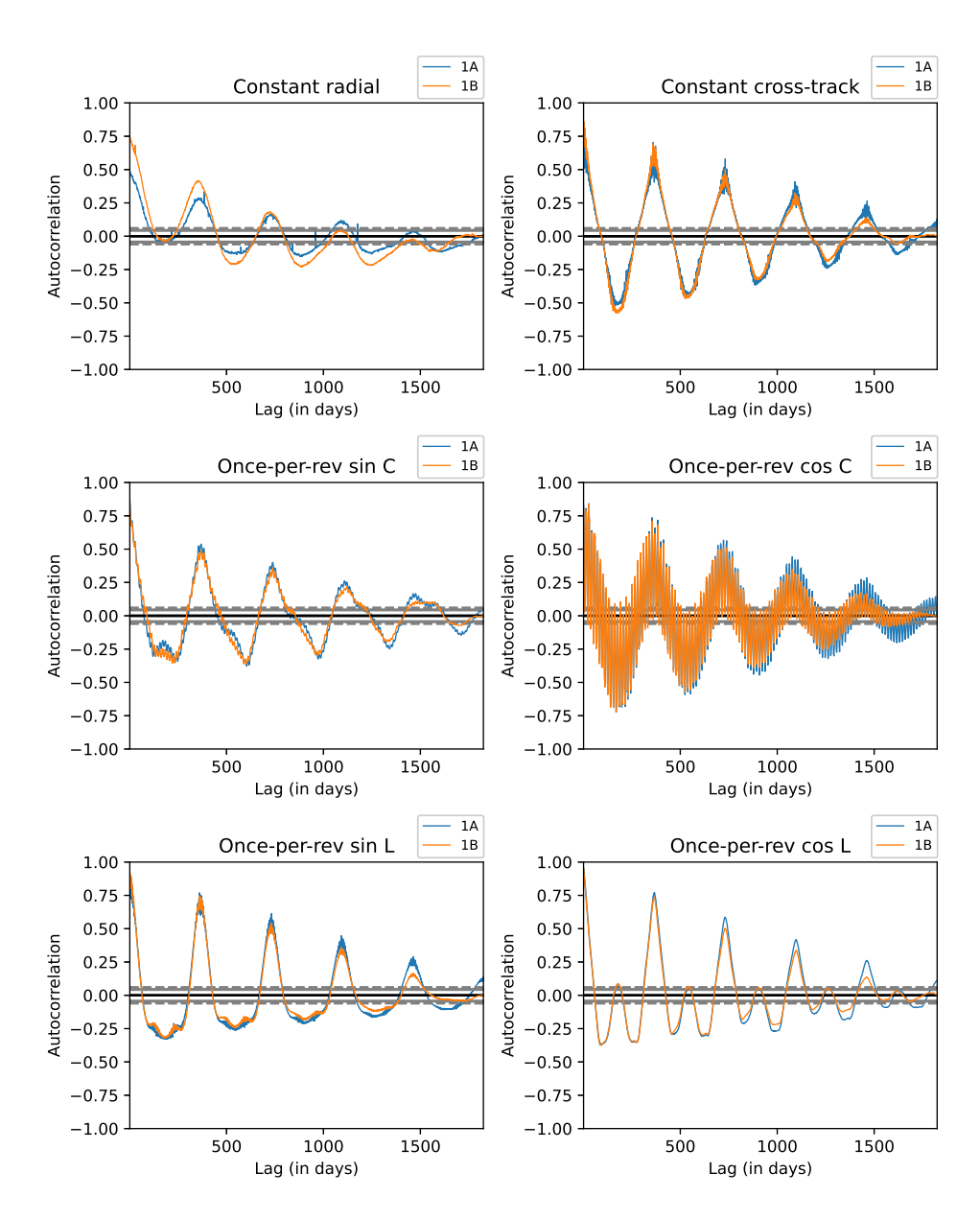


Figure 4.5: Auto-correlation plots for the empirical acceleration of Sentinel 1 satellites

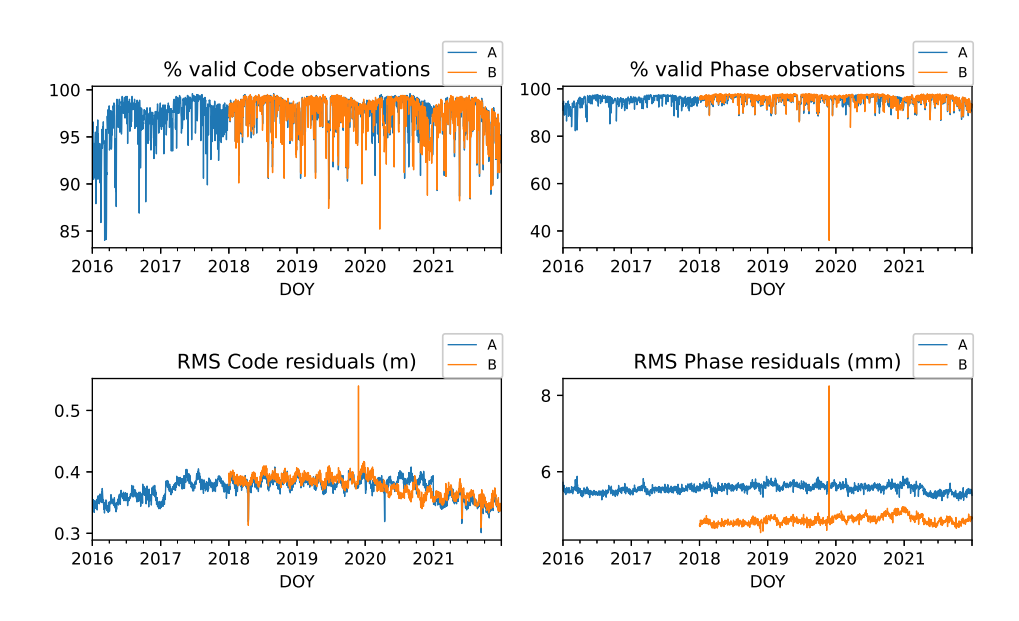


Figure 4.6: Sentinel 2 code and phase time series plots

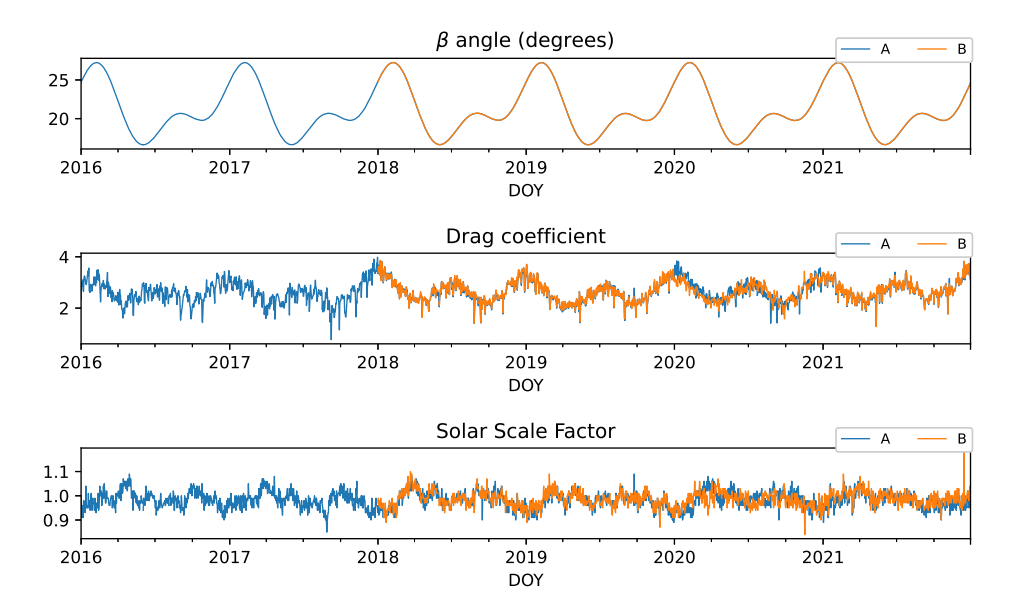


Figure 4.7: Sentinel 2 β angle, drag coefficient, and Solar Scale factor time series plots

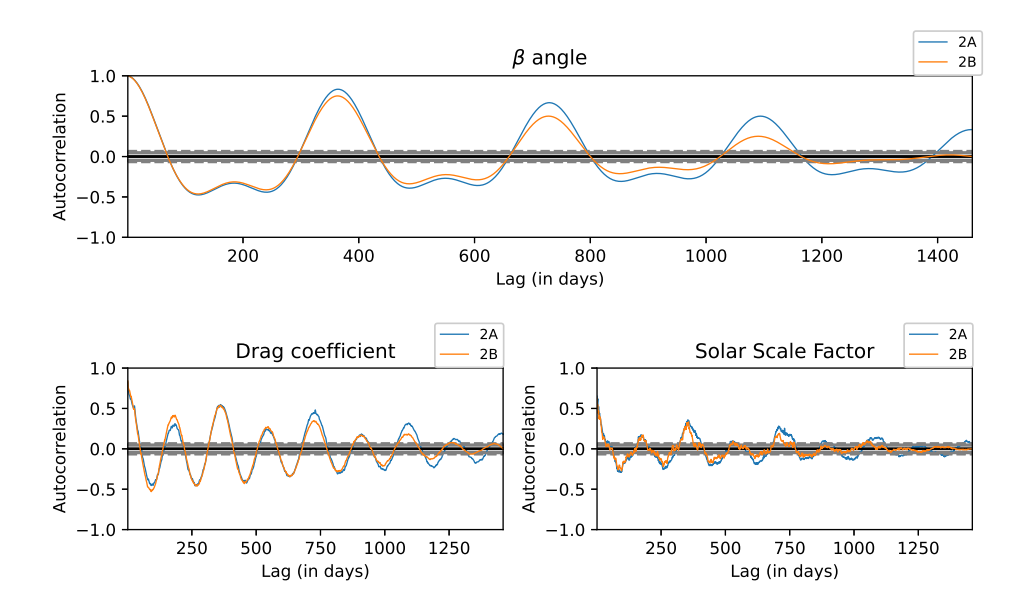


Figure 4.8: Auto-correlation plots for the β angle, drag coefficient, and solar scale factor of Sentinel 2 satellites

Figure 4.9 shows the time series plots of the empirical accelerations estimated for the Sentinel 2 satellites. The empirical accelerations correlate for the Sentinel 2A and 2B except in the year 2020, which can be traced back to weaker correlations in the percentage of valid code and phase observations used for the estimate, RMS of code, and phase residuals, drag coefficient, and the solar scale factor.

The constant radial and cross-track accelerations, and the once-per-revolution sin C and cos C accelerations of Sentinel 2B show significant outliers for the day 330 of 2019, which can be traced back to the very low percentage of valid phase measurements available for the orbit determination. This led to an erroneous fit to the dynamic model of the satellite that was absorbed by the empirical accelerations. Outliers can be seen in constant radial acceleration, once-per-revolution sin L, and cos L acceleration of Sentinel 2B on the day 348 of 2021. A high solar scale factor of 1.18 and a high drag coefficient of 3.83 has also been recorded for the same day. An outlier is observed on the day 267 of 2019, in the constant radial acceleration of Sentinel 2A, the cause of which is not clear.

The periodicity of the empirical accelerations can be deduced from the auto-correlation plots shown in figure 4.10. The constant radial acceleration shows no periodicity in Sentinel 2A but a periodicity of 365 days in the case of Sentinel 2B. The constant cross-track acceleration shows a periodicity of 365 days for 2A but none for 2B. The sin C acceleration has a periodicity of 365 days for both the Sentinel satellites. The cos C acceleration shows periodic variations of 15, 182.4, and 365 days. The sin L acceleration has a periodicity of 182.5 and 365 days, and also a small periodic component of 58 days. The cos L has a periodic variation of 122, 182.5, and 365 days.

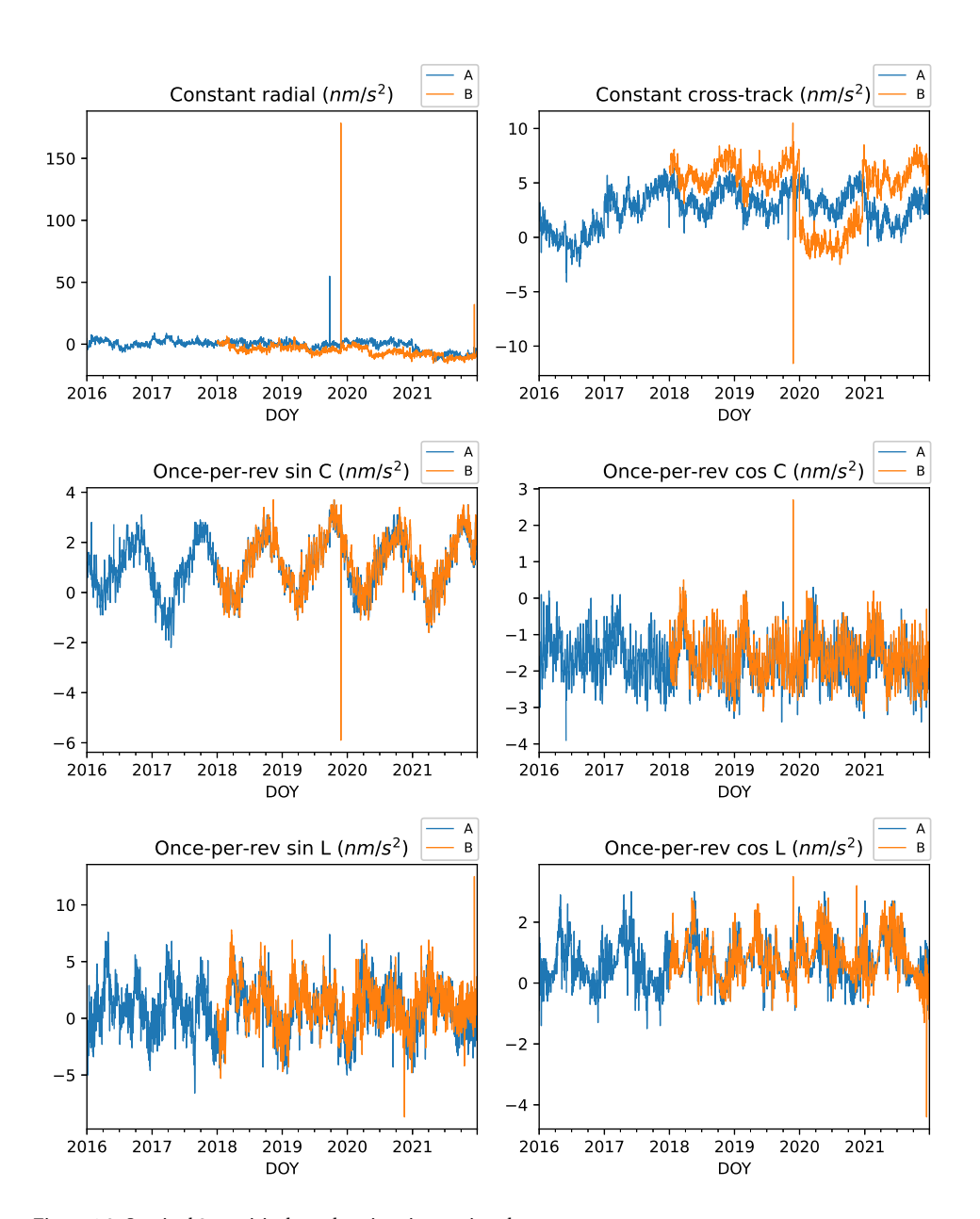


Figure 4.9: Sentinel 2 empirical acceleration time series plots

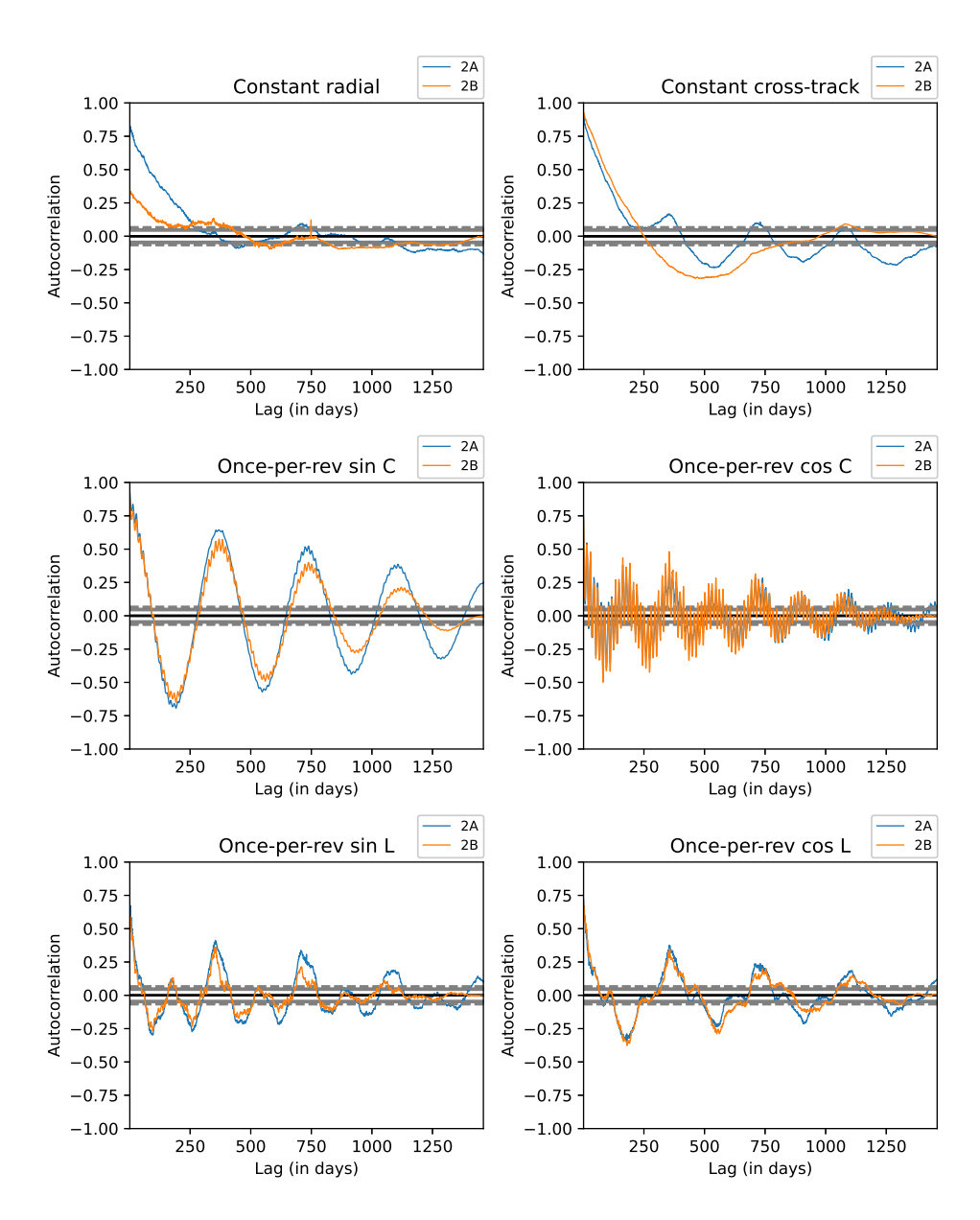


Figure 4.10: Auto-correlation plots for the empirical acceleration of Sentinel 2 satellites

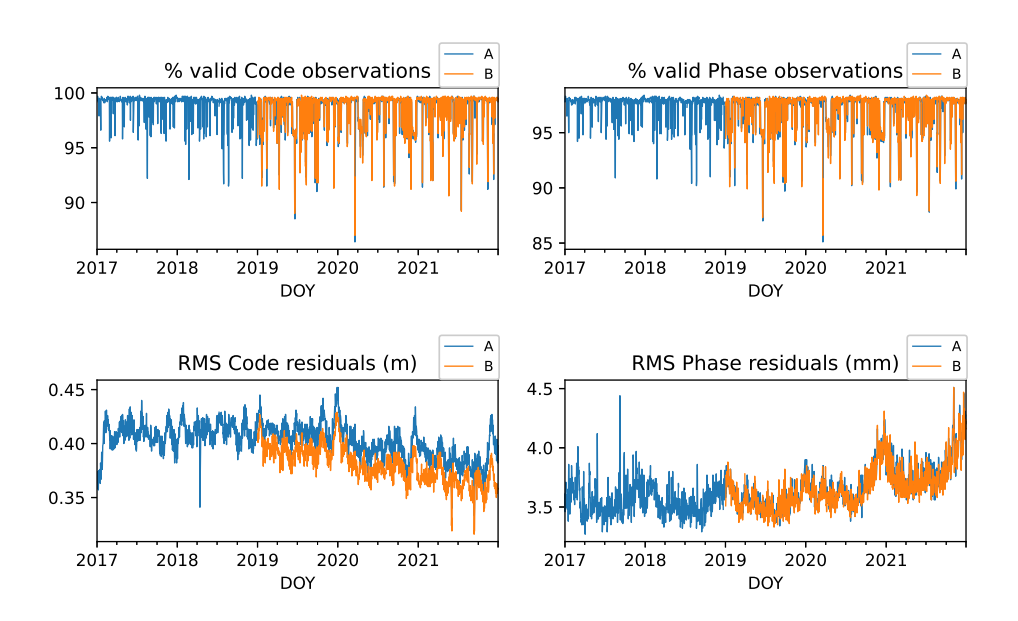


Figure 4.11: Sentinel 3 code and phase time series plots

SENTINEL 3

The time series plots of the percentage of code and phase measurements used in the orbit determination of the Sentinel 3 satellites, and their corresponding RMS of the code and phase residuals after the fit are shown in figure 4.11. All four parameters exhibit a strong correlation among Sentinel 3A and 3B satellites. The constant bias in RMS of code residuals of 3A and 3B can be due to the error in nominal phase center offset. On day 324 of 2018, an outlier is observed on the RMS phase residual plot of Sentinel 3B. This might be because of the execution of 3 maneuvers on the day, which was not estimated accurately in GIPSYX/RTGx.

The β angle, drag coefficient, and solar scale factor time series plots of the Sentinel 3 satellites are shown in figure 4.12. All the three parameters appear to be correlated for Sentinel 3A and 3B (strength of the correlation is given in section 4.2.3). The β angle of the two satellites is almost the same as expected. since the two satellites are in the same orbit. The β angle, drag coefficient, and solar scale factor show periodic variations of periods 182.5 and 365 days which can be confirmed in the auto-correlation plot shown in figure 4.13. The solar scale factor also shows a small component of periodicity of 122 days.

Figure 4.14 shows the time series empirical acceleration plots for Sentinel 3 satellites. The empirical accelerations seem to be correlated for 3A and 3B satellites. The constant empirical accelerations have a clear difference in magnitude, which was not the case for the Sentinel 1 and Sentinel 2 missions. Error in antenna phase center offset of the satellite can be compensated by additional cross-track acceleration. In POD of Sentinel 3A, the error of 9 mm in cross-track component of antenna offset can result in a mean

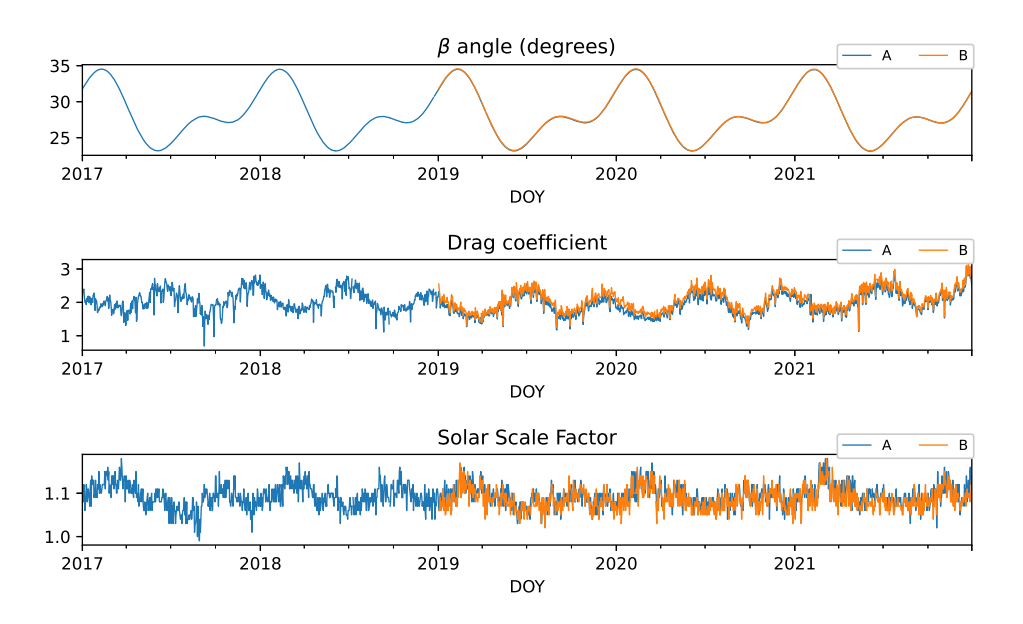


Figure 4.12: Sentinel 3 β angle, drag coefficient, and Solar Scale factor time series plots

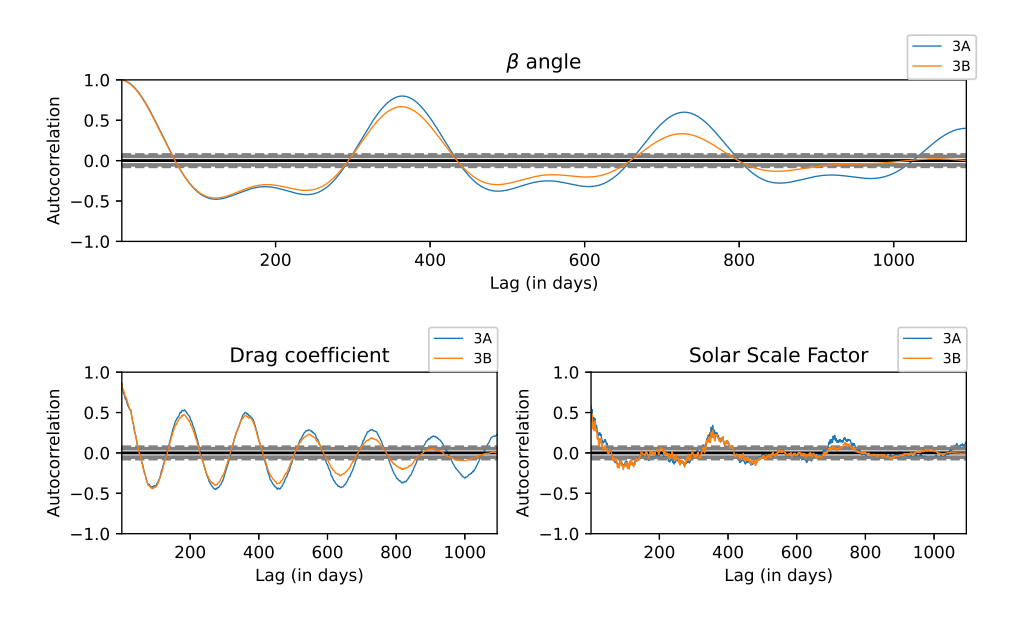


Figure 4.13: Auto-correlation plots for the β angle, drag coefficient, and solar scale factor of Sentinel 3 satellites

cross-track acceleration of $10 \ nm/s^2$ [38]. An increase in radial acceleration can cause a decrease in orbital radius[39]. Thus, an error in the knowledge of CoM location can potentially explain the difference in magnitude of constant empirical acceleration values and the high code residuals of Sentinel 3A compared to Sentinel 3B. On day 324 of 2018, a spike in constant radial empirical acceleration is estimated. The same day showed a spike in the RMS phase residuals. This might be due to the improper estimation of the three maneuvers executed by the satellite on the day. Some part of the error in the estimation of the maneuvers was absorbed by the constant radial empirical acceleration.

The periodic variations of the empirical accelerations can be obtained from the autocorrelation plots given in figure 4.15. The constant radial acceleration exhibits a periodicity of 182.5 and 365 days for Sentinel 3A, and a small periodic component of 182.5 days for Sentinel 3B. The constant cross-track acceleration exhibits the 365-day period for both the Sentinel 3 satellites. The sin C acceleration shows a 365 days periodicity, whereas, the cos C has a periodicity of 15, 182.5, and 365 days. The sin L acceleration shows a periodic variation of 182.5 and 365 days and small periodic components of 15 and 49.5 days. The cos L acceleration has a periodicity of 122, 182.5, and 365 days.

4.1.2. STATISTICAL DISTRIBUTION OF PARAMETERS

The statistical distribution can give insights into the nature of the parameter. For example, we know that "a combination of random fluctuations converges to the Gaussian if no fluctuation tends to dominate" [40]. Hence, if a Gaussian distribution is observed, it can be deduced that the value of the parameter is not a result of dramatic variations of the dependent parameters. Also, a comparison of the distribution of a parameter for the two identical satellites can give some insights into the causes of variations in the parameter.

% of valid Code and Phase measurements

The table 4.1 contains the summary statistics for the percentage of valid code measurements. For sentinel 1 and 2 satellites, the distribution is unimodal, skewed negatively, and positively kurtotic or leptokurtic distribution. Sentinel 3 satellites form a bi-modal distribution. In the figure 4.16, it can be observed that the data distribution of the A and B satellites are similar.

The summary statistics of the percentage of valid phase measurements are given in table 4.2. Similar to the percentage of valid code measurements, the percentage of valid phase measurements shows a uni-modal, negatively skewed, and positively kurtotic (leptokurtic) distribution for Sentinel 1 and 2 satellites, and a bi-modal distribution for the Sentinel 3 satellites. The shape of the distributions for the A and B satellites are similar which can be observed in figure 4.17.

RMS of code and phase residuals

The RMS of code residuals has a bi-modal distribution in all Sentinel satellites as shown in figure 4.18. The standard deviation in all cases is very low (<0.02 m) as shown in table 4.3 which is a good indication of the robustness of the orbit determination procedure. The shape of the data distributions for A and B satellites are similar for Sentinel 1 and 2. The difference in the shape of RMS code distribution might be because of the low amount of data available (3 years - 2019-2021) for Sentinel 3B.

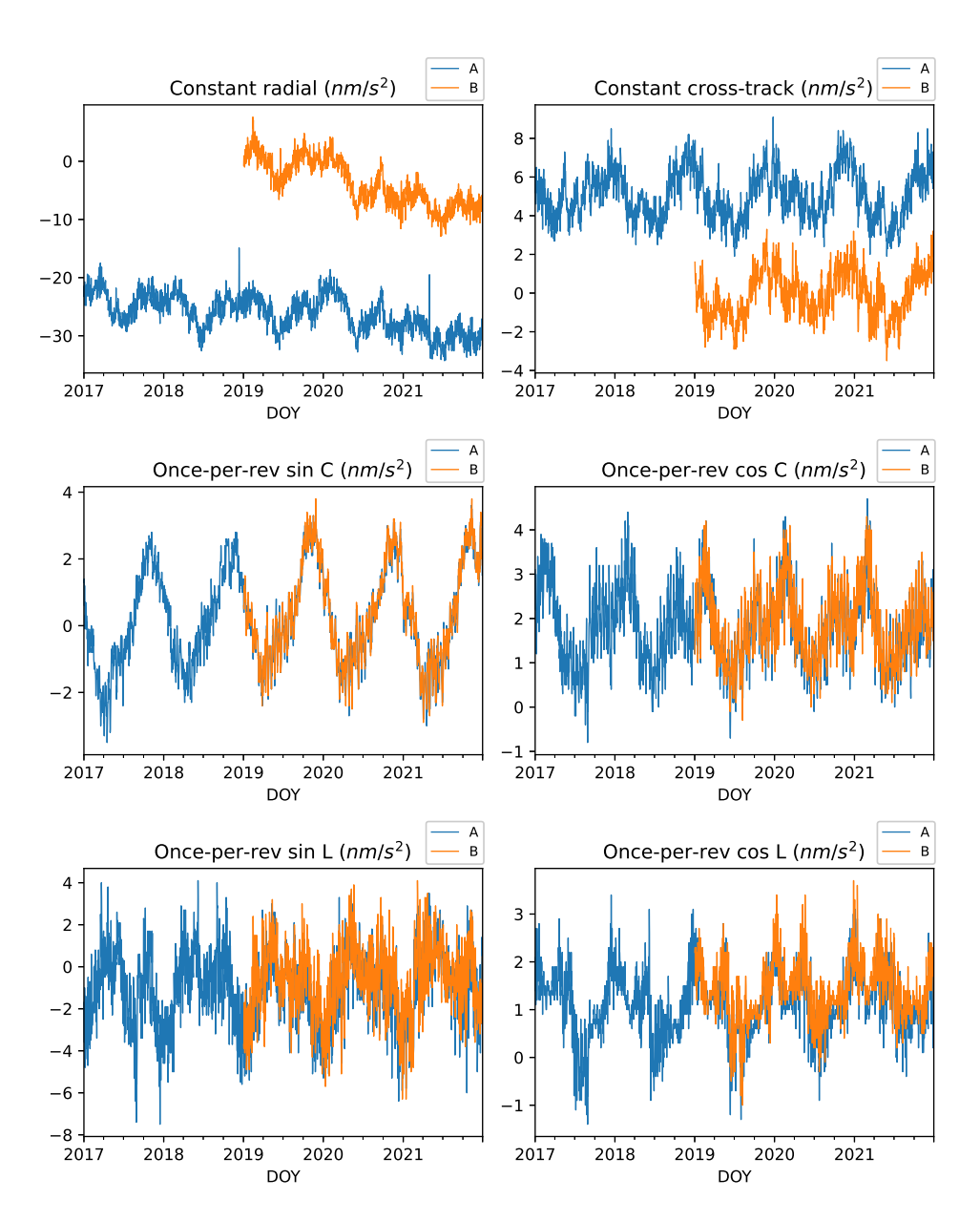


Figure 4.14: Sentinel 3 empirical acceleration time series plots

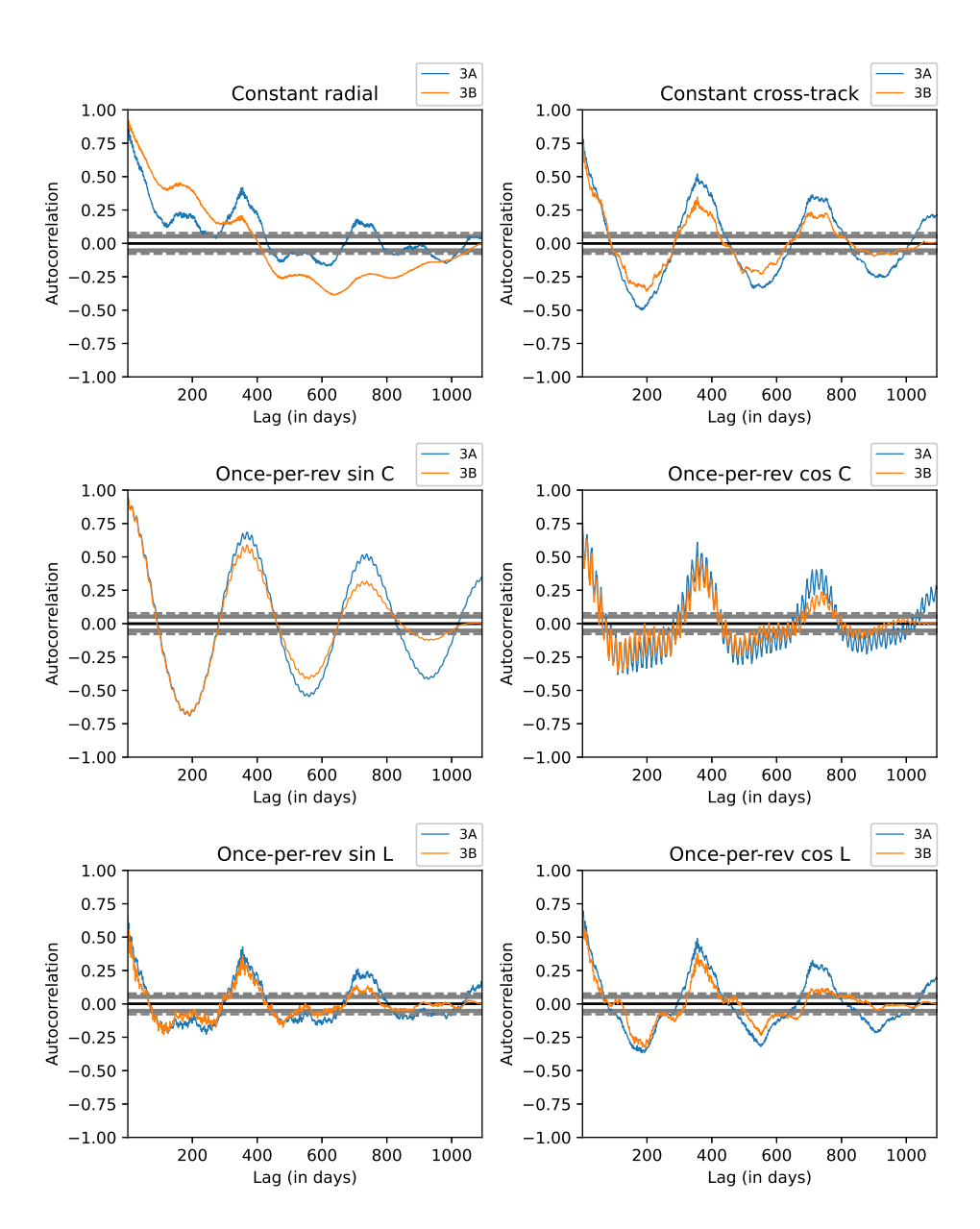


Figure 4.15: Auto-correlation plots for the empirical acceleration of Sentinel 3 satellites

Code %	1A	1B	2A	2B	3A	3B
Mean	96.64	97.00	97.39	97.54	98.71	98.54
Median	97.30	97.60	98.10	98.30	99.30	99.40
Mode	99.00	98.70	99.10	99.20	99.40	99.50
Std. Deviation	2.52	2.01	2.08	2.00	1.57	1.77
Skewness	-1.97	-1.62	-2.08	-1.82	-2.79	-2.36
Std. Error of Skewness	0.05	0.06	0.05	0.06	0.05	0.07
Skewness test statistic	-37.61	-28.33	-39.65	-28.40	-51.95	-32.86
Kurtosis	6.27	4.54	5.84	3.85	9.37	6.42
Std. Error of Kurtosis	0.10	0.11	0.10	0.13	0.11	0.14
Kurtosis test statistic	59.95	39.67	55.82	30.05	87.39	44.72
Minimum	77.90	80.90	84.00	85.20	86.40	87.00
Maximum	99.50	99.50	99.60	99.50	99.80	99.80

Table 4.1: Summary statistics of % of valid code measurements

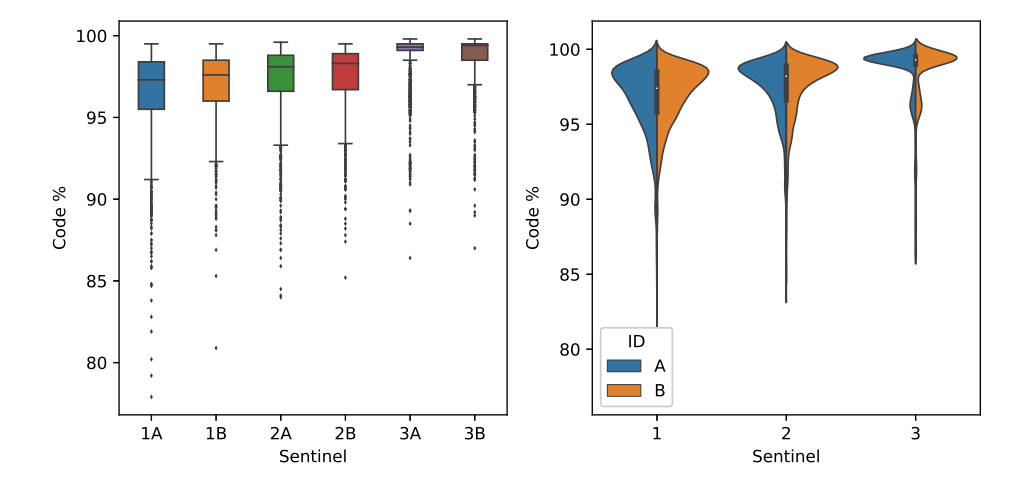


Figure 4.16: Box-plots and violin plots for % valid code measurements

The RMS phase residual data distributions of Sentinel 1 and Sentinel 2 satellites appear slightly different for the A and B satellites, as seen in figure 4.19. The slight difference in the shape might be because of the difference in the number of samples used for obtaining the statistics. The summary statistics of the parameter is given in table 4.4.

The difference in mean and mode of the A and B satellites is a result of the constant bias in the residual values that were observed in the time series plots, which could be caused by the error in nominal phase center offset as speculated in section 4.1.1.

DRAG COEFFICIENT

The distribution of the drag coefficient can be uni-modal or bi-modal since it is not clear from the density plot of the data, which can be seen in 4.20. The data distribution is

Phase %	1A	1B	2A	2B	3A	3B
Mean	95.00	94.61	95.41	95.98	97.28	97.12
Median	95.70	95.10	96.10	96.80	97.90	97.90
Mode	97.20	96.50	97.00	97.50	98.00	98.00
Std. Deviation	2.46	1.94	2.01	2.52	1.55	1.75
Skewness	-1.97	-1.61	-2.09	-10.11	-2.78	-2.36
Std. Error of Skewness	0.05	0.06	0.05	0.06	0.05	0.07
Skewness test statistic	-37.67	-28.13	-40.00	-157.76	-51.92	-32.86
Kurtosis	6.31	4.60	5.97	220.90	9.44	6.49
Std. Error of Kurtosis	0.10	0.11	0.10	0.13	0.11	0.14
Kurtosis test statistic	60.38	40.16	57.08	1724.12	88.07	45.19
Minimum	76.50	78.90	82.30	36.00	85.10	85.70
Maximum	97.90	97.10	97.60	98.00	98.40	98.40

Table 4.2: Summary statistics of % of valid phase measurements

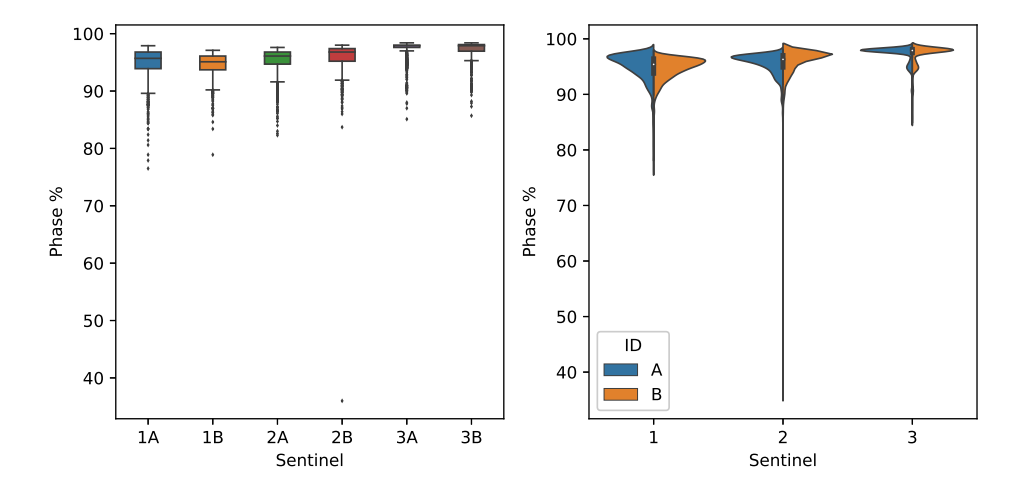


Figure 4.17: Box-plots and violin plots for % valid phase measurements

slightly different for A and B satellites for all Sentinel missions. The difference in shape might be a representation of the drag coefficient following slightly different trends in the first couple of years for the A satellites. The summary statistics are given in table 4.5.

The altitude of Sentinel 1 is 693 km, Sentinel 2 is 786 km, and Sentinel 3 is 814.5 km. As the altitude increases, the atmospheric density decreases. However, the drag coefficient must be the same irrespective of the altitude difference if the atmospheric density is modeled accurately. In case of inaccuracy of the atmospheric density, the shift in the drag coefficient magnitude to compensate for the inaccuracy is higher for satellites at a lower altitude because of the stronger drag forces. This can be observed as the difference in the standard deviation of the drag coefficient values (smallest for Sentinel 3, and largest for Sentinel 1) shown in table 4.5.

RMS_C	1A	1B	2A	2B	3A	3B
Mean	0.44	0.42	0.37	0.38	0.40	0.38
Median	0.44	0.42	0.38	0.38	0.40	0.38
Mode	0.45	0.43	0.38	0.39	0.41	0.39
Std. Deviation	0.01	0.01	0.02	0.02	0.02	0.02
Skewness	-0.22	-0.62	-0.58	0.05	-0.30	-0.06
Std. Error of Skewness	0.05	0.06	0.05	0.06	0.05	0.07
Skewness test statistic	-4.21	-10.91	-10.99	0.83	-5.60	-0.79
Kurtosis	-0.75	0.00	-0.40	4.63	0.21	0.33
Std. Error of Kurtosis	0.10	0.11	0.10	0.13	0.11	0.14
Kurtosis test statistic	-7.20	0.02	-3.80	36.14	1.95	2.28
Minimum	0.38	0.35	0.30	0.31	0.33	0.32
Maximum	0.47	0.45	0.41	0.54	0.45	0.43

Table 4.3: Summary statistics of RMS of code residuals

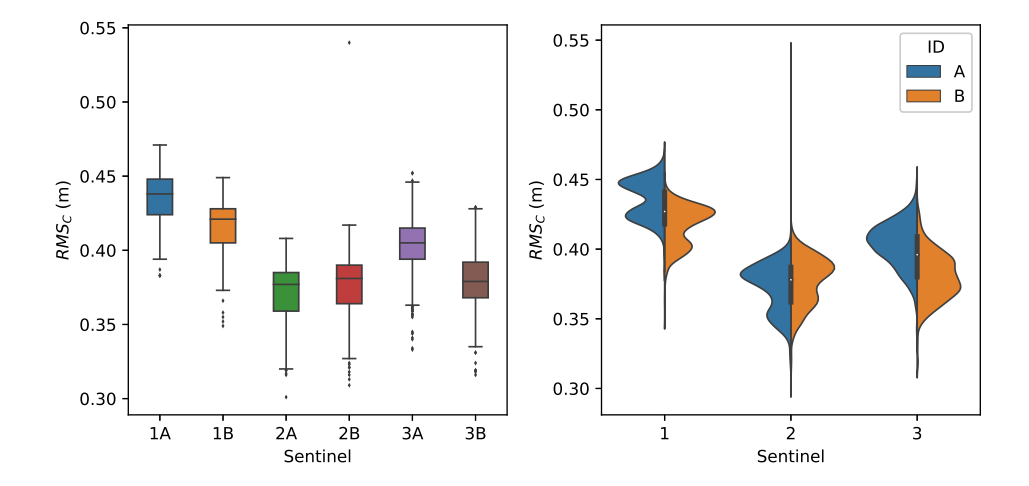


Figure 4.18: Box-plots and violin plots for RMS of code residuals

SOLAR SCALE FACTOR

The solar scale factor for the Sentinel 1 satellites has a bi-modal distribution. For Sentinel 2 satellites, the modality is not clear from the plot 4.21. The data distribution for A and B satellites is similar. The summary statistics of the solar scale factor are given in 4.6.

CONSTANT EMPIRICAL ACCELERATIONS

The summary statistics of constant radial empirical acceleration is given in table 4.7. The distribution of the constant radial accelerations for Sentinel 1 satellites has the same shape for the A and B satellites. In the case of the Sentinel 2 and Sentinel 3 satellites, the distribution differs in shape for A and B satellites, as observed in 4.22. The distributions of constant radial acceleration of Sentinel 1, 2, and 3B satellites are positively skewed

RMS_P	1A	1B	2A	2B	3A	3B
Mean	5.04	5.85	5.56	4.74	3.63	3.67
Median	5.04	5.89	5.56	4.72	3.60	3.63
Mode	5.01	5.89	5.58	4.69	3.56	3.58
Std. Deviation	0.15	0.16	0.10	0.14	0.18	0.18
Skewness	0.02	-0.82	-0.10	11.23	1.13	1.22
Std. Error of Skewness	0.05	0.06	0.05	0.06	0.05	0.07
Skewness test statistic	0.47	-14.27	-1.94	175.13	21.09	16.95
Kurtosis	1.44	0.09	-0.07	277.19	1.99	2.35
Std. Error of Kurtosis	0.10	0.11	0.10	0.13	0.11	0.14
Kurtosis test statistic	13.74	0.77	-0.64	2163.47	18.59	16.39
Minimum	4.58	5.34	5.24	4.40	3.27	3.33
Maximum	6.29	6.19	5.88	8.25	4.51	4.72

Table 4.4: Summary statistics of RMS of phase residuals

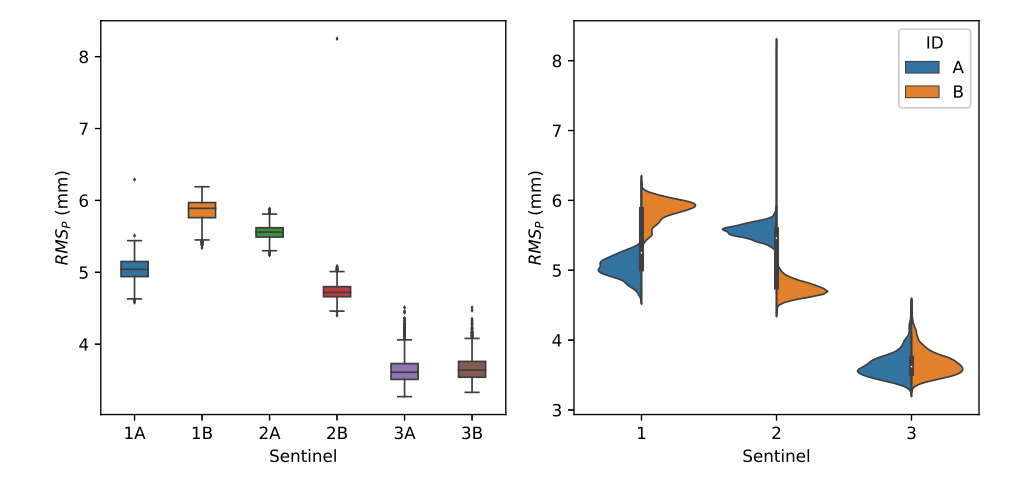


Figure 4.19: Box-plots and violin plots for RMS of phase residuals $\,$

and leptokurtotic. The mean, median, and mode for Sentinel 3 satellites differ by >20 nm/s^2 , the cause for which could be the error in the location of CoM, as stated in the section 4.1.1.

The summary statistics of the constant cross-track acceleration is given in table 4.8. The shape of the distributions of the constant cross-track accelerations for the A and B satellites of the Sentinel 1 and 3 missions is the same as shown in figure 4.25, however, there is a difference in the central tendency (mean, median, mode) of the Sentinel 3 satellites due to the error in Antenna phase center offset (addressed in section 4.1.1). For the Sentinel 2 mission, the shape of data distribution for A and B satellites is different.

The constant radial and cross-track acceleration distributions for the A and B satellites of the Sentinel 2 and Sentinel 3 missions are very different from each other. In the-

C_d	1A	1B	2A	2B	3A	3B
Mean	3.49	3.44	2.63	2.67	2.02	2.08
Median	3.38	3.29	2.61	2.65	2.02	2.07
Mode	3.39	3.30	2.68	2.60	2.06	2.39
Std. Deviation	0.75	0.78	0.41	0.38	0.33	0.32
Skewness	0.54	0.62	0.05	0.13	0.07	0.20
Std. Error of Skewness	0.05	0.06	0.05	0.06	0.05	0.07
Skewness test statistic	10.37	10.76	1.05	1.98	1.32	2.80
Kurtosis	-0.12	-0.23	0.28	-0.15	-0.37	-0.35
Std. Error of Kurtosis	0.10	0.11	0.10	0.13	0.11	0.14
Kurtosis test statistic	-1.19	-2.01	2.71	-1.18	-3.49	-2.45
Minimum	1.16	1.14	0.77	1.28	0.69	1.16
Maximum	5.86	5.82	3.98	3.87	3.07	3.16

Table 4.5: Summary statistics of drag coefficient

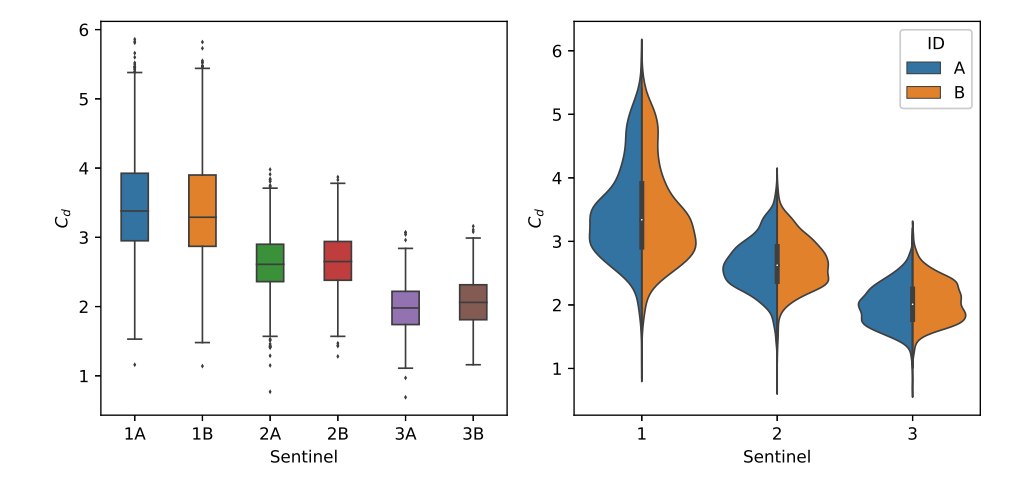


Figure 4.20: Box-plots and violin plots for drag coefficient

ory, the A and B satellites are identical and are acted upon by similar external forces. Hence a difference in the distributions points to sources of modeling errors specific to the satellite. Some of the possibilities of error sources are - errors in the center of mass, GPS antenna position relative to CoM, mass distribution, orientation, motor burn model, etc.

ONCE-PER-REVOLUTION EMPIRICAL ACCELERATIONS

The summary statistics of the sin C acceleration are given in table 4.9. The distributions are multi-modal, as shown in figure 4.24, because of which the skewness and kurtosis are not taken into account in the analysis since they can be misleading. The mean, median, mode, and standard deviation match for the A and B satellites for Sentinel 1, 2, and 3.

Solar scale factor	1A	1B	2A	2B	3A	3B
Mean	0.93	0.93	0.98	0.99	1.09	1.09
Median	0.92	0.92	0.98	0.99	1.09	1.08
Mode	0.87	0.88	0.98	0.99	1.09	1.08
Std. Deviation	80.0	0.07	0.03	0.03	0.03	0.02
Skewness	0.27	0.18	0.03	0.16	0.17	0.44
Std. Error of Skewness	0.05	0.06	0.05	0.06	0.05	0.07
Skewness test statistic	5.12	3.13	0.66	2.48	3.19	6.13
Kurtosis	0.16	-0.62	-0.09	1.23	0.36	0.18
Std. Error of Kurtosis	0.10	0.11	0.10	0.13	0.11	0.14
Kurtosis test statistic	1.57	-5.44	-0.89	9.62	3.35	1.28
Minimum	0.63	0.73	0.85	0.84	0.99	1.02
Maximum	1.27	1.16	1.09	1.18	1.18	1.18

Table 4.6: Summary statistics of Solar Scale factor

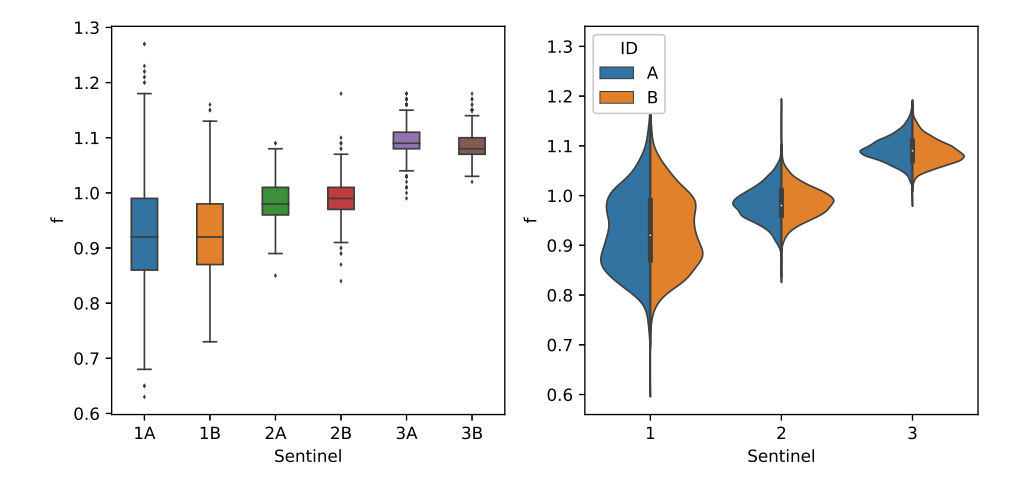


Figure 4.21: Box-plots and violin plots for Solar Scale factor

The shape of distributions for A and B satellites of Sentinel 1 and 2 missions are similar.

The cos C acceleration summary statistics for all the satellites are given in table 4.10. The mean, median, and standard deviations of the A and B satellites are similar. However, the central tendency of cos C for Sentinel 2 satellites is on the negative side, whereas it is on the positive side for the Sentinel 1 and 3 satellites. From the figure 4.25, it can be observed that the distributions are uni-modal and similar for the A and B satellites. In the case of Sentinel 1 satellites, the distribution is negatively skewed, whereas that of Sentinel 2 and 3 satellites are positively skewed. All the distributions except for that of Sentinel 2B are platykurtic.

The table 4.11 shows slight differences in the mean, median, and standard deviation for the once-per-revolution sin L acceleration for the A and B satellites. It can be ob-

Constant Radial	1A	1B	2A	2B	3A	3B
Mean	-0.87	-1.63	-0.56	-5.30	-25.84	-3.47
Median	-0.80	-1.70	0.40	-5.40	-25.70	-3.90
Mode	-1.50	-2.10	1.60	-3.30	-22.70	-6.90
Std. Deviation	6.09	5.19	4.22	6.29	3.17	4.33
Skewness	8.40	2.71	0.13	17.32	-0.20	1.61
Std. Error of Skewness	0.05	0.06	0.05	0.06	0.05	0.07
Skewness test statistic	160.70	47.27	2.45	270.25	-3.65	22.44
Kurtosis	193.50	44.75	13.72	502.20	-0.61	18.22
Std. Error of Kurtosis	0.10	0.11	0.10	0.13	0.11	0.14
Kurtosis test statistic	1850.91	390.79	131.14	3919.64	-5.66	126.83
Minimum	-21.40	-13.80	-14.00	-15.60	-34.30	-12.90
Maximum	151.70	86.50	54.90	178.50	-14.90	49.80

Table 4.7: Summary statistics of Constant radial acceleration

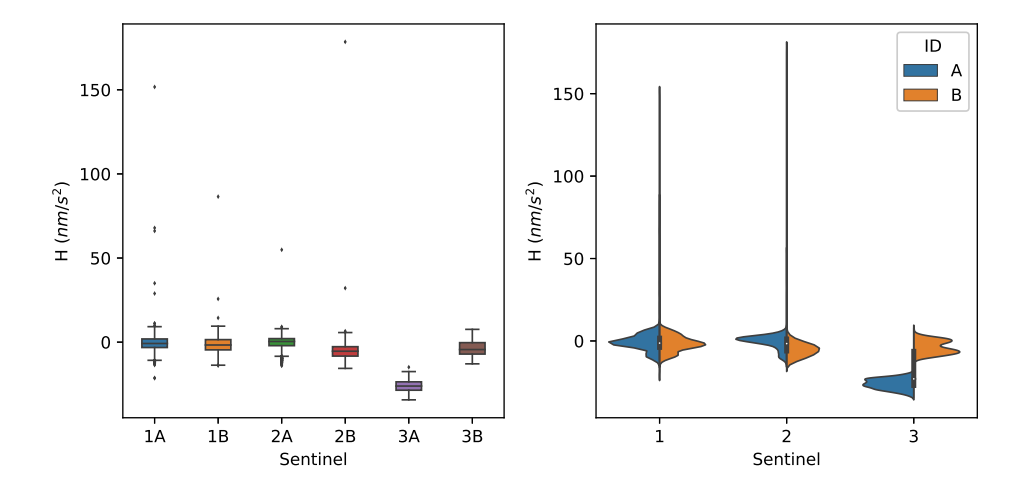


Figure 4.22: Box-plots and violin plots for Constant radial acceleration

served in figure 4.26 that the modality of the distributions cannot be deduced from the available data. Since the data distribution might not be uni-modal, the skewness and kurtosis are not taken into account for analysis. The distribution for A and B satellites is similar for Sentinel 1 and 2 missions.

The figure 4.27 shows that the data forms a uni-modal distribution and are similar in shape for the A and B satellites. The summary statistics of cos L acceleration are given in table 4.12. In the case of Sentinel 1 and 3 satellites, the data is skewed negatively, whereas in the case of Sentinel 2A, the data is positively skewed, and the skewness for the case of Sentinel 2B is inconclusive from the available data. The cos L accelerations of Sentinel 2B, 3A, and 3B show positive excess kurtosis (leptokurtic), whereas the kurtosis of the other satellites is inconclusive.

Constant cross-track	1A	1B	2A	2B	3A	3B
Mean	-2.56	-2.38	2.71	4.43	5.03	-0.01
Median	-1.70	-1.60	2.90	5.40	5.00	0.00
Mode	-12.50	3.00	2.70	6.10	4.20	-0.70
Std. Deviation	9.32	8.67	1.72	2.84	1.25	1.23
Skewness	-0.09	-0.13	-0.45	-1.00	0.19	0.04
Std. Error of Skewness	0.05	0.06	0.05	0.06	0.05	0.07
Skewness test statistic	-1.73	-2.25	-8.68	-15.56	3.47	0.52
Kurtosis	-0.40	-0.93	-0.19	0.13	-0.57	-0.55
Std. Error of Kurtosis	0.10	0.11	0.10	0.13	0.11	0.14
Kurtosis test statistic	-3.87	-8.11	-1.77	0.98	-5.34	-3.85
Minimum	-36.50	-24.20	-4.10	-11.60	1.90	-3.50
Maximum	32.40	20.10	6.40	10.50	9.10	3.30

Table 4.8: Summary statistics of Constant cross-track acceleration

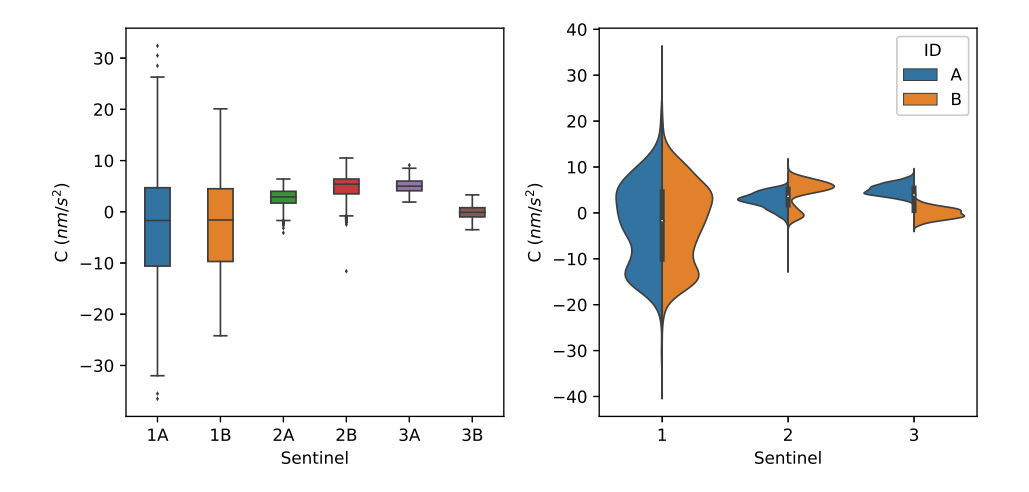


Figure 4.23: Box-plots and violin plots for Constant cross-track acceleration

The distribution of the four once per revolution accelerations for the A and B satellites of the Sentinel 1, 2, and 3 missions are similar, except for the sin C and sin L accelerations of Sentinel 3 satellites, as observed in violin plots in the figures 4.24, 4.25, 4.26, and 4.27. The slight difference in the Sentinel 3 sin C and sin L distributions is because of the low amount of available data, which is subject to the differences in statistics due to the section of the periodic variation in the database. For example, sin C has a periodic variation of 365 days. The sin C data in Sentinel 3A has 6 crests and 6 troughs, and that of Sentinel 3B has 4 crests and 3 troughs. Hence, the shape of the distribution varies slightly.

Once-per-rev sin C	1A	1B	2A	2B	3A	3B
Mean	-0.24	-0.26	1.07	1.22	0.25	0.48
Median	-0.30	-0.30	1.10	1.20	0.10	0.30
Mode	-0.10	-0.50	1.00	0.60	-0.60	-0.30
Std. Deviation	1.04	1.05	1.09	1.10	1.43	1.48
Skewness	-0.11	-0.03	-0.15	-0.27	0.09	0.09
Std. Error of Skewness	0.05	0.06	0.05	0.06	0.05	0.07
Skewness test statistic	-2.13	-0.51	-2.92	-4.15	1.70	1.30
Kurtosis	0.01	-0.31	-0.68	0.30	-0.88	-1.01
Std. Error of Kurtosis	0.10	0.11	0.10	0.13	0.11	0.14
Kurtosis test statistic	0.12	-2.69	-6.49	2.31	-8.21	-7.01
Minimum	-4.40	-3.60	-2.20	-5.90	-3.50	-2.90
Maximum	2.70	2.90	3.70	3.70	3.60	3.80

Table 4.9: Summary statistics of Once-per-revolution sin C acceleration

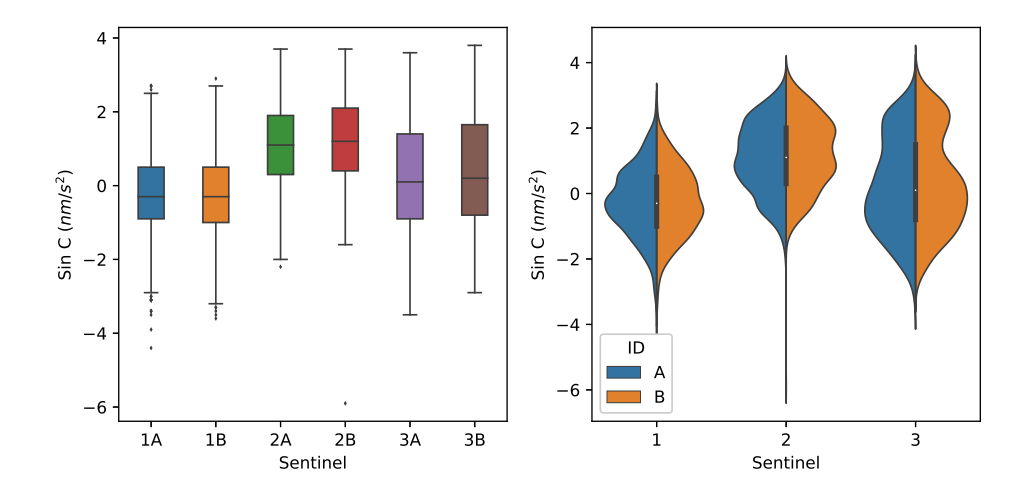


Figure 4.24: Box-plots and violin plots for Once-per-revolution sin C acceleration

4.2. MUTIVARIATE ANALYSIS

In this analysis, the correlation coefficient for two pairs of variables are calculated to obtain insights into the relative behaviour of the two variables. The correlation in the range of 0.2-0.4 is weak, 0.4-0.6 is moderate, 0.6-0.8 is strong, and greater than 0.8 is very strong. The significance of each of the correlation coefficients is also calculated and only the ones with more than 95% confidence (significant at the 0.05 level) are taken into account in the analysis.

4.2.1. CORRELATION ACROSS PARAMETERS OF EACH SATELLITE

The goal of this correlation analysis is to find out the dependence of a parameter on other variables. For example, if the estimated drag coefficient is observed highly corre-

Once-per-rev cos C	1A	1B	2A	2B	3A	3B
Mean	2.52	2.52	-1.67	-1.58	1.79	1.89
Median	2.60	2.50	-1.70	-1.60	1.70	1.80
Mode	2.40	2.50	-2.00	-1.70	1.40	1.20
Std. Deviation	0.72	0.70	0.63	0.64	0.85	0.82
Skewness	-0.30	-0.29	0.20	0.49	0.25	0.31
Std. Error of Skewness	0.05	0.06	0.05	0.06	0.05	0.07
Skewness test statistic	-5.72	-5.02	3.77	7.65	4.74	4.35
Kurtosis	-0.36	-0.34	-0.22	1.08	-0.26	-0.34
Std. Error of Kurtosis	0.10	0.11	0.10	0.13	0.11	0.14
Kurtosis test statistic	-3.41	-3.00	-2.06	8.40	-2.40	-2.40
Minimum	0.30	0.20	-3.90	-3.10	-0.80	-0.30
Maximum	4.40	4.40	0.30	2.70	4.70	4.30

Table 4.10: Summary statistics of Once-per-revolution cos C acceleration

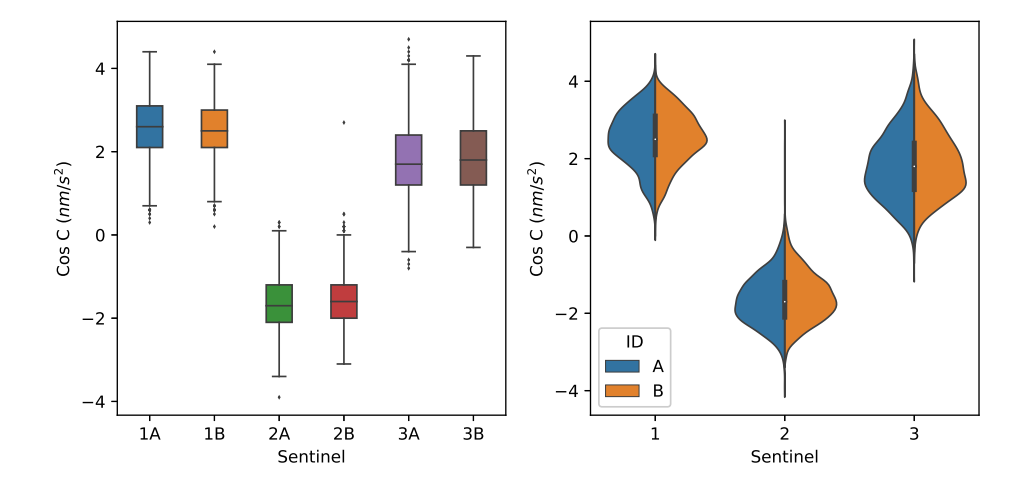


Figure 4.25: Box-plots and violin plots for Once-per-revolution cos C acceleration

lated with $F_{10.7}$ flux, it would mean that the dynamic model does not take into account the effect of the $F_{10.7}$ flux which is then reflected in the estimated drag coefficient. The $F_{10.7}$ flux should ideally be taken into account in the atmospheric density model and should not affect the drag coefficient of the satellite. The correlation across all parameters for each satellite is included in the Appendix A. In this section, a comparison of the correlations across relevant parameters for all satellites will be presented.

% OF VALID CODE AND PHASE MEASUREMENTS

The percentage valid code measurements have a negative correlation with $F_{10.7}$, Mg II index, S_{10} index, Ap index, and Sunspot number for Sentinel 1 and 2 satellites as shown in table 4.13. The percentage valid phase measurements have a weak negative correla-

Once-per-rev sin L	1A	1B	2A	2B	3A	3B
Mean	-0.09	-0.05	0.80	1.13	-0.98	-0.69
Median	0.20	0.20	0.80	1.20	-0.90	-0.60
Mode	0.40	0.40	1.20	.7	0.10	-0.70
Std. Deviation	0.87	0.78	2.19	1.97	1.85	1.74
Skewness	-1.02	-1.05	-0.01	0.05	-0.10	-0.27
Std. Error of Skewness	0.05	0.06	0.05	0.06	0.05	0.07
Skewness test statistic	-19.56	-18.26	-0.10	0.78	-1.95	-3.74
Kurtosis	0.40	0.37	-0.15	1.12	-0.14	-0.10
Std. Error of Kurtosis	0.10	0.11	0.10	0.13	0.11	0.14
Kurtosis test statistic	3.86	3.19	-1.39	8.75	-1.27	-0.72
Minimum	-3.40	-2.60	-6.60	-8.70	-7.50	-6.30
Maximum	2.40	1.80	7.60	12.50	5.00	4.10

Table 4.11: Summary statistics of Once-per-revolution sin L acceleration

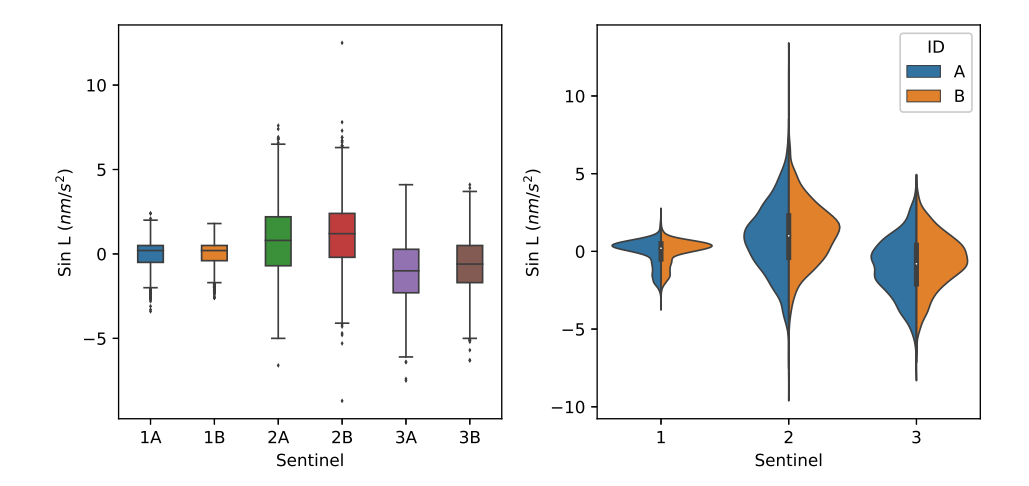


Figure 4.26: Box-plots and violin plots for Once-per-revolution $\sin L$ acceleration

tion with $F_{10.7}$, Mg II index, S_{10} index, Ap index, and Sunspot number for Sentinel 1B, 2A, and 2B, and a moderate correlation for Sentinel 1A as shown in table 4.14. This is consistent with observations reported in the existing literature about solar and geomagnetic activity causing ionospheric disturbances that lead to degradation of GPS measurements [41], [42].

The correlations obtained for Sentinel 3B are insignificant and hence nothing conclusive can be said about the computed correlations. However, the correlations of percentage valid code measurements with $F_{10.7}$ flux, S_{10} index and sunspot number, and the percentage valid phase measurement with S_{10} index for Sentinel 3A are significant, but the strength of the correlation is very weak (negligible). The orbits of Sentinel 1 and 2 satellites are sun-synchronous whereas the Sentinel 3 satellites are not. This might be

Once-per-rev cos L	1A	1B	2A	2B	3A	3B
Mean	1.48	1.63	0.70	0.79	1.12	1.41
Median	1.30	1.50	0.60	0.70	1.10	1.40
Mode	0.10	0.50	0.50	0.50	.9a	1.40
Std. Deviation	3.75	3.60	0.69	0.71	0.70	0.62
Skewness	-0.29	-0.37	0.35	0.10	-0.11	0.19
Std. Error of Skewness	0.05	0.06	0.05	0.06	0.05	0.07
Skewness test statistic	-5.58	-6.48	6.69	1.50	-2.11	2.61
Kurtosis	-0.04	0.07	0.03	1.92	0.39	0.52
Std. Error of Kurtosis	0.10	0.11	0.10	0.13	0.11	0.14
Kurtosis test statistic	-0.34	0.60	0.29	14.98	3.62	3.62
Minimum	-10.70	-10.00	-1.50	-4.40	-1.40	-1.00
Maximum	10.70	10.10	3.00	3.50	3.40	3.70

Table 4.12: Summary statistics of Once-per-revolution cos L acceleration

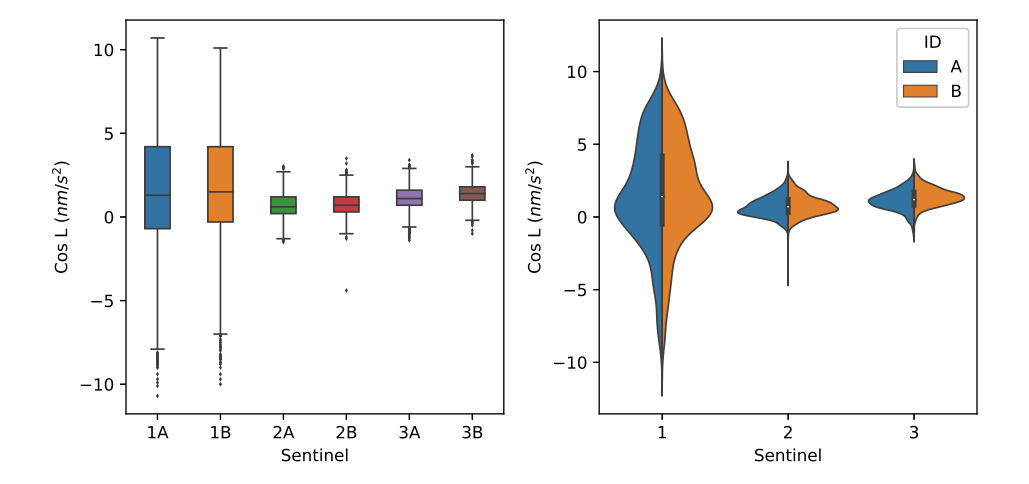


Figure 4.27: Box-plots and violin plots for Once-per-revolution cos L acceleration

the reason for the difference in correlations observed.

RMS of code and phase residuals

The RMS of code residuals exhibits a positive correlation with constant radial acceleration, and negative correlations with $F_{10.7}$ flux, Mg II index, S_{10} index, and the sunspot number for all satellites, which is given in table 4.15. This points to the fact that increased solar activity corresponds to an increase in RMS of code residuals which shows a reduction in the accuracy of the orbit estimation.

The RMS of phase residuals are positively correlated with constant radial accelerations for Sentinel 1 and 2 satellites but negatively correlated for Sentinel 3 satellites. It is negatively correlated with $F_{10.7}$ flux, Mg II index, and sunspot number for 1B, and 2A,

Code %	1A	1B	2A	2B	3A	3B
RMS_C	.356**	.248**	.315**	.180**	017	048
β	362**	343**	229**	100**	.014	.028
C_d	.192**	.258**	028	080**	.037	025
f	.125**	.151**	.067**	.096**	.019	015
H	.165**	.339**	.039	.097**	.073**	006
C	225**	257**	.107**	072**	005	.023
SinC	076**	148**	041	129**	032	.006
CosC	.133**	.223**	002	.097**	.041	.028
SinL	.207**	.290**	.122**	.132**	.003	031
CosL	116**	175**	.196**	.168**	.055*	.056
$F_{10.7}$	519**	405**	370**	325**	.045*	.026
Mg II	468**	368**	350**	280**	.022	.040
S_{10}	537**	332**	400**	201**	.095**	.043
Ap	426**	391**	364**	218**	.045*	.037
R	413**	330**	320**	253**	.044*	.031

^{**.} Correlation is significant at the 0.01 level (2-tailed).

Table 4.13: Correlation of % valid code measurements with other parameters

Phase %	1A	1B	2A	2B	3A	3B
RMS_P	.113**	.208**	009	490**	042	.022
β	367**	369**	241**	078**	.011	.021
C_d	.197**	.290**	040	087**	.034	027
f	.127**	.167**	.079**	.136**	.016	017
Н	.143**	.327**	.027	410**	.065**	010
C	228**	277**	.076**	.042	007	.019
SinC	080**	158**	054*	.007	035	.003
CosC	.133**	.231**	.002	036	.038	.024
SinL	.207**	.281**	.135**	.126**	.004	026
CosL	112**	167**	.202**	.065*	.053*	.053
$F_{10.7}$	513**	378**	344**	239**	.031	.019
Mg II	457**	319**	321**	201**	.014	.035
S_{10}	531**	292**	365**	135**	.080**	.037
Ap	430**	397**	356**	156**	.025	.028
R	407**	297**	292**	180**	.032	.027

^{**.} Correlation is significant at the 0.01 level (2-tailed).

Table 4.14: Correlation of % valid phase measurements with other parameters

^{*.} Correlation is significant at the 0.05 level (2-tailed).

^{*.} Correlation is significant at the 0.05 level (2-tailed).

RMS_C	1A	1B	2A	2B	3A	3B
β	.030	.128**	088**	.112**	.138**	.251**
C_d	142**	245**	072**	.005	108**	236**
f	044*	058*	.054*	074**	050*	041
Н	.239**	.382**	.471**	.570**	.244**	.648**
C	.054*	.085**	.457**	.064*	.011	.017
SinC	.009	.019	.042	134**	029	.091**
CosC	001	023	.009	.077**	.017	.094**
SinL	.056**	.050*	.078**	045	140**	216**
CosL	.021	011	.038	.077**	.003	001
$F_{10.7}$	482**	446**	504**	541**	354**	482**
Mg II	663**	676**	618**	666**	487**	642**
S_{10}	516**	462**	574**	539**	423**	639**
Ap	073**	.016	115**	050	034	034
R	434**	414**	478**	483**	321**	476**

^{**.} Correlation is significant at the 0.01 level (2-tailed).

Table 4.15: Correlation of RMS code residuals with other parameters

but positively correlated for 3A and 3B. The correlations of RMS phase residuals with other parameters cannot be determined conclusively, since it is not consistent with all satellites as shown in table 4.16.

A correlation between β angle with GPS triple differenced data residuals was observed for GOCE and GRACE-A satellites but no clear correlation was observed for GRACE-B and CHAMP satellites by Van den IJssel [35]. In this analysis, weak negative correlations were observed between β angle and RMS of phase residuals for Sentinel 1 satellites. However, weak positive correlations were observed for Sentinel 2A and 3A satellites and correlations of negligible strength were observed for Sentinel 2B and 3B. A weak positive correlation was observed between β angle and RMS of code residuals only for Sentinel 3B and negligible correlations were observed for the rest of the satellites. There was no consistency observed in the correlations of β angle and GPS residuals across all satellites. From this analysis it can be concluded that there is no correlation between the β angle and GPS residuals in orbits computed by the orbit determination strategy described in section 2.3.

DRAG COEFFICIENT

The correlation coefficients of the drag coefficient with other parameters are given in the table 4.17. The drag coefficient is negatively correlated to the Ap index (moderate correlation for Sentinel 1 and 2, and weak correlation for Sentinel 3) for all the Sentinel satellites. This points to the improper modeling of the effect of geomagnetic activity in the atmospheric density model DTM2000.

^{*.} Correlation is significant at the 0.05 level (2-tailed).

RMS_P	1A	1B	2A	2B	3A	3B
β	266**	225**	.206**	.154**	.209**	.154**
C_d	.129**	.045	.064**	.118**	.022	.264**
f	.062**	.004	129**	186**	.119**	.093**
Н	.510**	.587**	.318**	.445**	288**	392**
C	129**	079**	.432**	372**	.330**	.347**
SinC	219**	176**	.005	092**	.320**	.335**
CosC	.208**	.120**	059**	.066*	.167**	.116**
SinL	.240**	.220**	159**	180**	152**	135**
CosL	063**	002	010	.107**	.260**	.230**
$F_{10.7}$	147**	367**	353**	.115**	.395**	.676**
Mg II	320**	610**	451**	.069**	.495**	.668**
S_{10}	024	354**	405**	094**	.146**	.664**
Ap	.135**	.053*	064**	069**	.302**	.315**
R	122**	332**	359**	004	.321**	.550**

^{**.} Correlation is significant at the 0.01 level (2-tailed).

Table 4.16: Correlation of RMS phase residuals with other parameters

C_d	1A	1B	2A	2B	3A	3B
β	734**	784**	.362**	.302**	368**	375**
f	.227**	.249**	425**	364**	300**	349**
Н	.388**	.383**	056**	.020	336**	413**
C	375**	432**	.129**	.085**	079**	.024
SinC	271**	223**	023	.058*	.055*	.144**
CosC	.270**	.270**	194**	136**	367**	417**
SinL	.149**	.125**	486**	423**	047*	105**
CosL	.120**	.129**	.053*	113**	.022	004
$F_{10.7}$.007	.011	.037	.240**	.212**	.351**
Mg II	.198**	.236**	.091**	.199**	.360**	.461**
S_{10}	.121**	.186**	.086**	.226**	.372**	.440**
Ap	412**	412**	466**	459**	367**	369**
R	.058**	.058*	.014	.150**	.234**	.334**

^{**.} Correlation is significant at the 0.01 level (2-tailed).

Table 4.17: Correlation of drag coefficient with other parameters

^{*.} Correlation is significant at the 0.05 level (2-tailed).

^{*.} Correlation is significant at the 0.05 level (2-tailed).

f	1A	1B	2A	2B	3A	3B
β	312**	316**	193**	064*	.340**	.322**
C_d	.227**	.249**	425**	364**	300**	349**
Н	.256**	.285**	.220**	.024	.403**	.217**
С	952**	941**	359**	103**	227**	227**
SinC	199**	236**	188**	217**	139**	060*
CosC	.319**	.310**	.552**	.504**	.685**	.674**
SinL	.273**	.253**	.981**	.978**	.650**	.668**
CosL	.005	.044	.173**	.104**	.311**	.073*
$F_{10.7}$	048*	077**	041	063*	.045*	.094**
Mg II	.030	.039	032	029	025	.009
S_{10}	018	.007	016	.026	.019	.018
Ap	006	.009	.104**	.120**	.092**	.151**
R	016	009	020	018	.039	.063*

^{**.} Correlation is significant at the 0.01 level (2-tailed).

Table 4.18: Correlation of solar scale factor with other parameters

SOLAR SCALE FACTOR

The correlation coefficients of the solar scale factor with other parameters are given in the table 4.18. The solar scale factor exhibits a very strong negative correlation with constant cross-track acceleration for Sentinel 1 satellites and a very strong positive correlation with sin L for Sentinel 2 satellites. A weak positive correlation is observed with constant radial acceleration for all satellites (nothing can be said about correlation in 2B as the computed correlation is not significant). It is correlated positively with cos C and sin L accelerations for all satellites. Negligible correlation is observed with $F_{10.7}$ flux (Sentinel 2A correlation is insignificant), which is expected if the $F_{10.7}$ flux is modeled accurately in the solar radiation pressure model. Most of the correlations with the rest of the parameters representing solar activity (Mg II index, S_{10} index, and sunspot number) are insignificant.

No consistency in the correlations of solar scale factor with β angle was observed across all satellites. The correlation between the solar scale parameter and β angle observed by Hackel et al [1], with the same solar radiation pressure model, was not replicated in this analysis. This indicates a successful implementation of the shadow model in the GIPSYX/RTGx software.

CONSTANT EMPIRICAL ACCELERATIONS

The constant radial empirical acceleration exhibits a positive correlation with the cos C acceleration, which can be seen in table 4.19. Since the empirical accelerations are calculated independently in the POD process, it might mean that the two accelerations are compensating for a common source of error. The radial acceleration is negatively correlated to Mg II index for all satellites except 1A.

The constant cross-track acceleration is negatively correlated to $\sin L$ for all satellites except 2B as shown in table 4.20.

^{*.} Correlation is significant at the 0.05 level (2-tailed).

Н	1A	1B	2A	2B	3A	3B
β	501**	575**	.237**	.269**	.463**	.385**
C	355**	440**	.140**	108**	.049*	.038
SinC	152**	140**	180**	281**	018	.064*
CosC	.266**	.306**	.272**	.291**	.504**	.325**
SinL	.219**	.223**	.196**	.047	.032	064*
CosL	118**	186**	.002	.055*	.148**	032
$F_{10.7}$	134**	319**	123**	276**	094**	451**
Mg II	153**	352**	385**	425**	396**	665**
S_{10}	.016	222**	034	311**	.048*	657**
Ap	.015	.032	.053*	025	.145**	007
R	076**	227**	174**	265**	107**	429**

^{**.} Correlation is significant at the 0.01 level (2-tailed).

Table 4.19: Correlation of constant radial acceleration with other parameters

С	1A	1B	2A	2B	3A	3B
β	.529**	.561**	.166**	.050	.306**	.257**
Н	355**	440**	.140**	108**	.049*	.038
SinC	.178**	.245**	.195**	.194**	.627**	.636**
CosC	420**	426**	229**	154**	.143**	.103**
SinL	370**	364**	382**	118**	581**	522**
CosL	.163**	.134**	095**	250**	.169**	.191**
$F_{10.7}$.068**	.103**	304**	.096**	.096**	.239**
Mg II	042*	051*	370**	.085**	004	.113**
S_{10}	.023	.004	541**	.224**	062**	.077**
Ap	.016	.003	102**	.112**	007	.000
R	.011	.006	308**	.147**	.002	.116**

^{**.} Correlation is significant at the 0.01 level (2-tailed).

Table 4.20: Correlation of constant cross-track acceleration with other parameters

^{*.} Correlation is significant at the 0.05 level (2-tailed).

^{*.} Correlation is significant at the 0.05 level (2-tailed).

sin C	1A	1B	2A	2B	3A	3B
β	.301**	.328**	281**	219**	.097**	.123**
Н	152**	140**	180**	281**	018	.064*
C	.178**	.245**	.195**	.194**	.627**	.636**
CosC	233**	276**	231**	245**	.112**	.172**
SinL	375**	487**	160**	207**	362**	292**
CosL	366**	239**	513**	536**	170**	174**
$F_{10.7}$.034	.056*	.050*	.167**	.126**	.274**
Mg II	.058**	.076**	.146**	.220**	.152**	.193**
S_{10}	068**	131**	024	.034	.028	.127**
Ap	.069**	.054*	.007	.019	.015	.018
R	.001	015	.035	.113**	.048*	.155**

^{**.} Correlation is significant at the 0.01 level (2-tailed).

Table 4.21: Correlation of sin C acceleration with other parameters

ONCE-PER-REV EMPIRICAL ACCELERATIONS

The sin C acceleration is negatively correlated to sin L for all satellites except for 2A (very weak correlation), which is shown in table 4.21. The cos C acceleration is positively correlated to radial acceleration for all satellites as given in table 4.22. The sin L acceleration exhibits a negative correlation with β angle for all satellites, which is shown in table 4.23. It also exhibits a negative correlation with cross-track acceleration for all satellites except Sentinel 2B. The correlation coefficients of cos L with other parameters for all satellites are given in table 4.24.

4.2.2. CORRELATION WHEN SATELLITE REPEATS ORBIT

The goal of this analysis is to find out if the position of the satellite with respect to Earth exerts any influence on the parameters. The Sentinel 1 satellites repeat their orbits every 12 days, the Sentinel 2 satellites every 10 days, and the Sentinel 3 satellites every 27 days. The table 4.25 shows the correlation of parameters with themselves when the satellites repeat their orbits.

The drag coefficient has a positive correlation for all the Sentinel satellites (strong correlation for Sentinel 1 and 3, and moderate correlation for Sentinel 3 satellites). The solar scale factor is positively correlated for all satellites except 3B. The weaker correlation of drag and solar scale factor for Sentinel 3 satellites compared to the Sentinel 1 and 2 satellites are expected due to the comparatively larger repeat period of the orbit. All the empirical accelerations are positively correlated for all satellites.

This analysis shows that the drag coefficient, solar scale factor, and empirical accelerations are influenced by the relative position of the satellite with respect to Earth.

4.2.3. Correlation of parameters of A and B satellites

Since the A and B satellites are identical and are in the same orbits around the Earth, a comparison of the behaviour of the parameters of the two satellites can throw some light

^{*.} Correlation is significant at the 0.05 level (2-tailed).

cos C	1A	1B	2A	2B	3A	3B
β	453**	454**	.263**	.338**	.671**	.644**
Н	.266**	.306**	.272**	.291**	.504**	.325**
C	420**	426**	229**	154**	.143**	.103**
SinC	233**	276**	231**	245**	.112**	.172**
SinL	.518**	.472**	.505**	.470**	.091**	.125**
CosL	286**	262**	.005	010	.247**	.065*
$F_{10.7}$	019	068**	.000	113**	.008	.072*
Mg II	.031	017	077**	149**	131**	078**
S_{10}	.026	053*	.057**	098**	038	088**
Ap	.043*	.035	.099**	.065*	.081**	.109**
R	.046*	.022	015	106**	033	002

^{**.} Correlation is significant at the 0.01 level (2-tailed).

Table 4.22: Correlation of cos C acceleration with other parameters

sin L	1A	1B	2A	2B	3A	3B
β	359**	345**	324**	201**	451**	452**
Н	.219**	.223**	.196**	.047	.032	064*
C	370**	364**	382**	118**	581**	522**
SinC	375**	487**	160**	207**	362**	292**
CosC	.518**	.472**	.505**	.470**	.091**	.125**
CosL	371**	347**	.194**	.151**	.013	147**
$F_{10.7}$	047*	147**	063**	113**	.051*	028
Mg II	063**	163**	039	046	.128**	.082**
S_{10}	.020	091**	038	.017	.128**	.096**
Ap	.009	.020	.093**	.106**	.071**	.088**
R	.008	049*	028	043	.095**	.059*

^{**.} Correlation is significant at the 0.01 level (2-tailed).

Table 4.23: Correlation of sin L acceleration with other parameters

^{*.} Correlation is significant at the 0.05 level (2-tailed).

^{*.} Correlation is significant at the 0.05 level (2-tailed).

cos L	1A	1B	2A	2B	3A	3B
β	.086**	.073**	104**	191**	.299**	.273**
Н	118**	186**	.002	.055*	.148**	032
C	.163**	.134**	095**	250**	.169**	.191**
SinC	366**	239**	513**	536**	170**	174**
CosC	286**	262**	.005	010	.247**	.065*
SinL	371**	347**	.194**	.151**	.013	147**
$F_{10.7}$.011	.076**	126**	159**	.039	.132**
Mg II	015	.039	089**	096**	013	.040
S_{10}	006	.151**	116**	008	.042	.092**
Ap	137**	140**	136**	107**	063**	052
R	066**	001	072**	103**	.018	.057

^{**.} Correlation is significant at the 0.01 level (2-tailed).

Table 4.24: Correlation of cos L acceleration with other parameters

	1A	1B	2A	2B	3A	3B
Cd	.607**	.765**	.638**	.706**	.559**	.553**
f	.573**	.628**	$.427^{**}$.395**	.238**	$.142^{**}$
Н	.471**	$.707^{**}$	$.769^{**}$.310**	$.640^{**}$.753**
C	.676**	.743**	.814**	$.876^{**}$.517**	.449**
SinC	.683**	$.694^{**}$	$.799^{**}$	$.746^{**}$.812**	.812**
CosC	.661**	.643**	.257**	.284**	.532**	$.472^{**}$
SinL	.805**	.846**	$.496^{**}$	$.440^{**}$.348**	.263**
CosL	.795**	$.784^{**}$	$.499^{**}$.533**	$.397^{**}$.314**

^{**.} Correlation is significant at the 0.01 level (2-tailed).

Table 4.25: Correlation of parameters of all Sentinel satellites when they repeat their orbits

^{*.} Correlation is significant at the 0.05 level (2-tailed).

	1	2	3
Cd	.992**	.928**	.983**
f	.578**	$.606^{**}$	$.649^{**}$
Н	.822**	$.374^{**}$.751**
C	.652**	.112**	.848**
SinC	.921**	.902**	.992**
CosC	.853**	.596**	.836**
SinL	.792**	$.646^{**}$	$.714^{**}$
CosL	.967**	.641**	$.743^{**}$

^{**.} Correlation is significant at the 0.01 level (2-tailed).

Table 4.26: Correlation of parameters of A and B satellites for same day data pairs

on the source of modeling errors.

The table 4.26 shows the correlation of parameters of A and B satellites of the Sentinel mission for the same day pairs of data. A very strong positive correlation is observed for the drag coefficient and once-per-revolution sin C empirical acceleration data in the case of all the Sentinel missions. The solar scale factor is positively correlated in all satellites. The radial acceleration has a very strong positive correlation for Sentinel 1, a weak positive correlation for Sentinel 2, and a strong positive correlation in the case of Sentinel 3. The cross-track acceleration is positively correlated only in Sentinel 1 and 3. The cos C acceleration is strongly positively correlated for Sentinel 1 and 3 and has a moderate positive correlation for Sentinel 2. The sin L and cos L acceleration are positively correlated for all satellites and the correlation is very strong for Sentinel 1 cos L acceleration.

The table 4.27 shows the correlation of parameters of A and B satellites of the Sentinel mission when they cover the same ground track. The Sentinel 1B repeats the orbit of the corresponding B satellite in 6 days, the Sentinel 2B in 5 days, and the Sentinel 3B in 11 days. The drag is strongly and positively correlated for all the Sentinel 1, 2, and 3 satellites. However, the correlation is smaller than the same-day correlations. The solar scale factor exhibits a moderate positive correlation in Sentinel 1 and a weak positive correlation for Sentinel 2 and 3 satellites. The radial acceleration has a moderate positive correlation for Sentinel 1, a weak correlation for Sentinel 2, and a strong positive correlation for Sentinel 3. The cross-track acceleration has a very strong positive correlation for Sentinel 1, a strong correlation for Sentinel 3, and no correlation for the case of Sentinel 2. The sin C acceleration has a strong positive correlation for Sentinel 1 and 2 and a very strong correlation for Sentinel 3. The cos C has a weak positive correlation for Sentinel 2, a moderate positive correlation for Sentinel 3, and a negligible correlation for Sentinel 1. The sin L acceleration has a very strong correlation for Sentinel 1, and moderate positive correlations for Sentinel 2 and 3. The cos L acceleration has a very strong correlation for Sentinel 1 and moderate correlations for Sentinel 2 and 3.

In the correlation analysis of the parameters of satellites A and B, negligible correlations were observed for Sentinel 2 cross-track acceleration in the case of same-day correlations, and Sentinel 2 cross-track, and Sentinel 1 cos C accelerations for the case of correlations when covering the same ground track.

	1	2	3
Cd	.801**	.720**	.730**
f	.797**	.412**	.385**
Н	.545**	$.374^{**}$	$.719^{**}$
С	.857**	.063*	$.629^{**}$
SinC	.726**	.787**	.880**
CosC	$.171^{**}$.253**	$.568^{**}$
SinL	.921**	$.472^{**}$	$.497^{**}$
CosL	.890**	.509**	$.569^{**}$

^{**.} Correlation is significant at the 0.01 level (2-tailed).

Table 4.27: Correlation of parameters of A and B satellites when they cover the same ground track.

5

CONCLUSION AND RECOMMENDATIONS

For the success of the Earth observation missions, high precision knowledge of satellite position is essential. Hence, this thesis was taken up with the objective to improve the strategy of orbit determination of Sentinel satellites at TU Delft. The main focus of this research was on identifying the unmodeled / miss-modeled forces, which are the major sources of errors in the orbit determination process. This thesis presents the design of a framework to analyze the forces estimated in the orbit determination, interpretation of the results of the analysis, and recommendations for further analysis and improvement of the force models.

A thorough study of the different aspects of the orbit determination at TU Delft was done and a set of parameters were selected which will be used in the analysis. A database of relevant parameters of the orbit determination data is created for each satellite. The data analysis methods are split into two types - Univariate and multivariate analysis. The univariate analysis consists of time series plots, autocorrelation plots, summary statistics, box plots, and violin plots of the individual parameters of the database. The multivariate analysis consists of different kinds of correlation analysis - correlation of different parameters for each satellite, correlation of parameters of a satellite when it repeats its orbit, correlation of parameters of A and B satellites for same days data pairs, and correlation of parameters of A and B satellites when they cover the same ground track. Thus, the research objective of developing a data analysis framework for the analysis of precise orbit determination of Sentinel satellites was achieved.

The other objectives of this research were to apply the developed data analysis framework to the database created for Sentinel satellites, utilize the results of the analysis to infer the sources of errors in the orbit determination from the observed trends, and issue recommendations for improving orbit determination strategy and for further analysis of the data. The results of the data analysis were presented and the major observations and their interpretations are given in the following sections. Multiple reasons for certain observations were speculated. The analysis needed to confirm the speculations are given

as recommendations since they could not be carried out due to time constraints in the research.

5.1. Univariate analysis conclusions

The constant bias observed between the RMS code and phase residuals of A and B satellites of Sentinel 1, 2, and 3 missions can be a result of the error in the nominal antenna phase center offset. To confirm this hypothesis, further analysis needs to be carried out. The phase center offsets are to be manipulated by a constant amount for all measurements, and POD is to be performed on the updated phase center offset values. The resulting RMS code and phase residuals need to be plotted for the A and B satellites to look for any changes in the RMS residuals. A few iterations might be needed to find the accurate amount of shift in the nominal phase center offset to bring the RMS residuals of the A and B satellites to the same range. If no change in RMS residuals is observed with a change in the phase center offset, then the hypothesis can be proved to be false. The phase center offsets can also be calculated at TU Delft using the GIPSYX/RTGx instead of using the data from the CPOD Service.

The percentage of valid code and phase measurements of Sentinel 2A and 2B satellites are correlated except for the year 2020. This effect is seen extending to RMS of code and phase residuals, solar scale factor, radial, and cross-track acceleration. However, no consistent correlations (across all satellites under consideration) were observed between the percentage valid code and phase measurements with RMS of code and phase residuals, solar scale factor, radial, and cross-track accelerations. Hence, the non-correlation in the percentage code and phase measurements for 2A and 2B satellites is not the reason for the non-correlation in RMS of code and phase residuals, solar scale factor, and radial and cross-track accelerations of Sentinel 2 satellites for the year 2020. Another possible reason can be an error in the antenna phase center offsets or the phase center variations for the year 2020. To confirm this, POD needs to be performed by using phase center offsets from other sources to see if the same effect is observed. Another possible test will be to perform POD after lowering the apriori sigmas for radial and cross-track accelerations and checking if the effect still exists. Restricting the apriori sigmas might limit the sudden variation in the accelerations observed towards the end of 2019 and the beginning of 2022. If the anomaly in the year 2020 is removed, then the changes in other plots can be investigated, which will give more insights into the source of the effect observed.

The radial and cross-track accelerations of Sentinel 3 satellites show a big difference in magnitude (>20 nm/s^2 for radial and 5 nm/s^2 for cross-track). This was attributed to an error in CoM location of the satellite (for radial) and antenna phase center offset (for cross-track). The hypothesis can be tested by changing the CoM location and cross-track component of the antenna phase center offset slightly and observing the results after performing POD using the new values.

The drag coefficient, solar scale factor, and all the once per rev empirical accelerations have a periodicity of one year and half years. This could be due to their dependence on seasons or the distance between Earth and Sun. The dependence on the distance between Earth and Sun can be investigated by correlating the drag coefficient and the solar scale factor with the orbit angle of Earth around the Sun. The Earth's orbit has a very low eccentricity of 0.0167 (leading to a difference in perihelion and aphelion distance of ap-

proximately $5x10^6$ km), which makes it less probable to cause a statistically significant variation in drag coefficient and the solar scale factor.

The shape of the data distribution of the radial and cross-track accelerations of the Sentinel 2 mission might be representative of modeling errors specific to the satellite. To confirm that the difference in shape is not due to the difference in the number of samples used, the violin plots need to be made for the same time periods for both satellites (2018-2021). If the difference in shape is still observed, the other source of error that needs to be investigated is the anomaly observed in the constant empirical accelerations in the year 2020. This will be done using phase center offsets from different sources or lowering of the apriori sigmas of the radial and cross-track accelerations, whichever works to remove the anomaly observed. If the anomaly is successfully removed, looking at the violin plots can confirm if the data distribution was different because of the uncorrelated data in the year 2020. Investigating the change in other parameters due to the removal of the anomaly (if successful) can give more insights into the error source. Some other possibilities of error sources are - errors in the CoM due to changes or errors in the knowledge of mass distribution and orientation.

5.2. MULTIVARIATE ANALYSIS CONCLUSIONS

The percentage valid code and phase measurements have a negative correlation with $F_{10.7}$, Mg II index, S_{10} index, Ap index, and Sunspot number for Sentinel 1 and 2 satellites. These correlations for Sentinel 3B were insignificant and the strength of the correlations for Sentinel 3A was negligibly weak. The possible reason for this observation might be that the Sentinel 1 and 2 satellites are in sun-synchronous orbits and are thus more prone to degradation of GPS measurements due to solar and geomagnetic activity compared to Sentinel 3 satellites whose orbits are not sun-synchronous. This hypothesis can be validated by calculating these correlations for other satellites in sun-synchronous and non-sun-synchronous orbits.

The RMS code residuals are negatively correlated to $F_{10.7}$ flux, Mg II index, S_{10} index, sunspot number. This indicates the inaccuracies in modeling the effects of solar activity on the satellite since the quality of the fit is affected by it.

The drag coefficient is negatively correlated to the Ap index. Hence, it can be concluded that the effects of geomagnetic activity have not been included accurately in the DTM2000 atmospheric density model. Hence, a more accurate atmospheric density model should be used to improve the drag estimate.

The solar scale factor is positively correlated with $\sin L$ empirical acceleration and the $\sin L$ acceleration, in turn, is negatively correlated to the β angle. However, no consistent correlations across satellites were observed for the solar scale factor and the β angle. The β angle is accounted for in the solar radiation pressure model by being included in the shadow model. To confirm the independence of the solar scale factor on the β angle, correlation analysis needs to be performed for the days when no shadows are observed.

Drag coefficient exhibits higher correlation for same-day data pairs of the A and B satellites compared to correlation when the satellites traverse the same ground track. The DTM2000 atmospheric density model accounts for latitude, longitude, solar local time, solar flux, and geomagnetic activity. This observation shows that the latitude and longitude terms must have a smaller influence on the atmospheric density compared to

the others.

5.3. RECOMMENDATIONS FOR FUTURE WORK

The short time available of this research constrained the amount of analysis that could be performed. Hence, the following recommendations are issued for future work to extend the analysis further.

- GIPSYX/RTGx is sub-optimal with the estimation of maneuvers. Hence, a similar analysis should be carried out on days when there are no maneuvers. Most likely, there will not be any statistically significant difference in the results of the analyses.
- 2. Other parameters like SLR residuals, and orbit overlaps should be included in the analysis.
- 3. The orbits in this analysis were computed after disabling the estimation of along-track acceleration. Enabling it might provide more insights, especially on the drag force model.
- 4. Enabling the estimation of Earth Radiation Scale factor in the POD can throw some light into the modeling of the Earth Radiation Pressure.
- 5. Investigation of the daily variation of the parameters like the empirical accelerations can bring into light smaller variations and sources of error than what were significant in this analysis.

BIBLIOGRAPHY

- [1] S. Hackel, O. Montenbruck, P. Steigenberger, U. Balss, C. Gisinger, and M. Eineder, "Model improvements and validation of TerraSAR-x precise orbit determination," *Journal of Geodesy*, vol. 91, no. 5, pp. 547–562, Dec. 2016. DOI: 10.1007/s00190-016-0982-x.
- [2] J. IJssel, GPS-based precise orbit determination and accelerometry for low flying satellites. S.l: s.n, 2014, ISBN: 9789462591363.
- [3] H. Peter, A. Jäggi, J. Fernández, *et al.*, "Sentinel-1A–First precise orbit determination results," *Advances in space research*, vol. 60, no. 5, pp. 879–892, 2017.
- [4] M. Zijlstra, S. Theil, and S. Scheithauer, "Model for short-term atmospheric density variations," in *Earth Observation with CHAMP*, Springer-Verlag, pp. 489–494. DOI: 10.1007/3-540-26800-6 77.
- [5] W. Bertiger, Y. Bar-Sever, A. Dorsey, *et al.*, "GipsyX/RTGx, a new tool set for space geodetic operations and research," *Advances in Space Research*, vol. 66, no. 3, pp. 469–489, Aug. 2020. DOI: 10.1016/j.asr.2020.04.015.
- [6] JPL. "GCORE Algorithm Description Document RTGx/GIPSYX." (Jul. 2020), [Online]. Available: https://gipsy-oasis.jpl.nasa.gov/docs/index.php.
- [7] O. Montenbruck, E. Gill, and F. Lutze, "Satellite Orbits: Models, Methods, and Applications," *Applied Mechanics Reviews*, vol. 55, no. 2, B27, 2002. DOI: 10.1115/1.1451162.
- [8] A. Hattori and T. Otsubo, "Time-varying solar radiation pressure on Ajisai in comparison with LAGEOS satellites," *Advances in Space Research*, vol. 63, no. 1, pp. 63–72, 2019.
- [9] J. A. Marshall and S. B. Luthcke, "Modeling radiation forces acting on TOPEX/Poseidon for precision orbit determination," *Journal of Spacecraft and Rockets*, vol. 31, no. 1, pp. 99–105, 1994.
- [10] C. Rodriguez-Solano, U. Hugentobler, and P. Steigenberger, "Adjustable box-wing model for solar radiation pressure impacting GPS satellites," *Advances in Space Research*, vol. 49, no. 7, pp. 1113–1128, Apr. 2012. DOI: 10.1016/j.asr.2012.01.016.
- [11] Q. Zhao, X. Wang, X. Hu, *et al.*, "An Enhanced Box-Wing Solar Radiation pressure model for BDS and initial results," in *EGU General Assembly Conference Abstracts*, ser. EGU General Assembly Conference Abstracts, Apr. 2016, EPSC2016-16562, EPSC2016-16562.
- [12] Y. Bar-Sever and D. Kuang, "New Empirically Derived Solar Radiation Pressure Model for Global Positioning System Satellites During Eclipse Seasons," *IPN Progress Report*, pp. 42–160, 2005.

64 BIBLIOGRAPHY

[13] A. Sibthorpe, W. Bertiger, S. D. Desai, B. Haines, N. Harvey, and J. P. Weiss, "An Evaluation of Solar Radiation Pressure Strategies for the GPS Constellation," *Journal of Geodesy*, vol. 85, no. 8, pp. 505–517, 2011.

- [14] G. Beutler, E. Brockmann, W. Gurtner, *et al.*, "Extended orbit modeling techniques at the CODE processing center of the international GPS service for geodynamics (IGS): theory and initial results," *Manuscripta geodaetica*, vol. 19, no. 6, pp. 367–386, 1994.
- [15] D. Arnold, M. Meindl, G. Beutler, *et al.*, "CODE's new solar radiation pressure model for GNSS orbit determination," *Journal of geodesy*, vol. 89, no. 8, pp. 775–791, 2015.
- [16] W. J. L. J.R. Wertz, Space Mission Analysis and Design. Springer, Sep. 30, 1999, 976 pp., ISBN: 0792359011. [Online]. Available: https://www.ebook.de/de/product/3800213/j_r_wertz_wiley_j_larson_space_mission_analysis_and_design.html.
- [17] L. G. Jacchia, "Revised Static Models of the Thermosphere and Exosphere with Empirical Temperature Profiles," *SAO Special Report*, vol. 332, May 1971.
- [18] A. E. Hedin, "Extension of the MSIS Thermosphere Model into the middle and lower atmosphere," *Journal of Geophysical Research: Space Physics*, vol. 96, no. A2, pp. 1159–1172, Feb. 1991. DOI: 10.1029/90ja02125.
- [19] M. Storz, B. Bowman, and J. Branson, "High Accuracy Satellite Drag Model (HASDM)," in *AIAA/AAS Astrodynamics Specialist Conference and Exhibit*, American Institute of Aeronautics and Astronautics, Aug. 2002. DOI: 10.2514/6.2002-4886.
- [20] M. Colace, S. Hackel, M. Kirschner, R. Kahle, and C. Circi, "Atmospheric density models comparison and impact on orbit solutions of GRACE-1, Sentinel-1A, TerraSAR-X," *EGUGA*, p. 9820, 2017.
- [21] J. M. Picone, A. E. Hedin, D. P. Drob, and A. C. Aikin, "NRLMSISE-00 empirical model of the atmosphere: Statistical comparisons and scientific issues," *Journal of Geophysical Research: Space Physics*, vol. 107, no. A12, SIA 15–1–SIA 15–16, Dec. 2002. DOI: 10.1029/2002ja009430.
- [22] B. Bowman, W. K. Tobiska, F. Marcos, C. Huang, C. Lin, and W. Burke, "A New Empirical Thermospheric Density Model JB2008 Using New Solar and Geomagnetic Indices," in AIAA/AAS Astrodynamics Specialist Conference and Exhibit, American Institute of Aeronautics and Astronautics, Aug. 2008. DOI: 10.2514/6.2008-6438.
- [23] C. F. Martin and D. P. Rubincam, "Effects of Earth albedo on the LAGEOS I satellite," Journal of Geophysical Research: Solid Earth, vol. 101, no. B2, pp. 3215–3226, 1996.
- [24] P. KNOCKE, J. RIES, and B. TAPLEY, "Earth Radiation Pressure Effects on Satellites," in *Astrodynamics Conference*, American Institute of Aeronautics and Astronautics, Aug. 1988. DOI: 10.2514/6.1988-4292.
- [25] S. P. Wyatt, "The Effect of Terrestrial Radiation Pressure on Satellite Orbits," in *Dynamics of Satellites/Dynamique des Satellites*, Springer, 1963, pp. 180–196.
- [26] A. Milani, A. M. Nobili, and P. Farinella, *Non-gravitational perturbations and satellite geodesy.* 1987.

BIBLIOGRAPHY 65

[27] K. F. Tapping, "The 10.7 cm solar radio flux (F10.7)," *Space Weather*, vol. 11, no. 7, pp. 394–406, Jul. 2013. DOI: 10.1002/swe.20064.

- [28] Space Weather Prediction Center Data, National Oceanic and Atmospheric Administration. [Online]. Available: http://www.swpc.noaa.gov/.
- [29] M. Snow, W. E. Mcclintock, T. N. Woods, O. R. White, J. W. Harder, and G. Rottman, "The Mg II Index from SORCE," *Solar Physics*, vol. 230, no. 1-2, pp. 325–344, Aug. 2005. DOI: 10.1007/s11207-005-6879-0.
- [30] Bremen Mg II composite data, Universität Bremen Satellite and Data Science Group. [Online]. Available: http://www.iup.uni-bremen.de/UVSAT/Datasets/mgii.
- [31] W. K. Tobiska, S. D. Bouwer, and B. R. Bowman, "The development of new solar indices for use in thermospheric density modeling," *Journal of Atmospheric and Solar-Terrestrial Physics*, vol. 70, no. 5, pp. 803–819, Mar. 2008. DOI: 10.1016/j.jastp.2007.11.001.
- [32] Archive of solar and geomagnetic indices for drag calculation, Heliogeophysical Prediction Service Laboratory. [Online]. Available: https://esc.cbk.waw.pl/search/select.php#.
- [33] D. Pangburn, "Influence of sunspots on global mean surface temperature," *Energy & Environment*, vol. 25, no. 8, pp. 1455–1471, Dec. 2014. DOI: 10.1260/0958-305x.25.8.1455.
- [34] Geomagnetic Observatory Niemegk, GFZ German Research Centre for Geosciences, Potsdam, Germany. [Online]. Available: ftp://ftp.gfz-potsdam.de/pub/home/obs/Kp_ap_Ap_SN_F107/.
- [35] J. Van Den IJssel, "Gps-based precise orbit determination and accelerometry for low flying satellites," Ph.D. dissertation, 2014. DOI: 10.4233/UUID: 9AABCDOF-D984-4D7F-8567-677689E07C85.
- [36] K.-S. C. Jonathan D. Cryer, *Time Series Analysis*. Springer-Verlag GmbH, Mar. 2008, 491 pp., ISBN: 9780387759593. [Online]. Available: https://www.ebook.de/de/product/24984080/jonathan_d_cryer_kung_sik_chan_time_series_analysis.html.
- [37] D. Cramer, Fundamental statistics for social research: step-by-step calculations and computer techniques using SPSS for Windows. London England: New York Routledge, 1998, ISBN: 9780415172042.
- [38] O. Montenbruck, S. Hackel, and A. Jäggi, "Precise orbit determination of the Sentinel-3A altimetry satellite using ambiguity-fixed GPS carrier phase observations," *Journal of Geodesy*, vol. 92, no. 7, pp. 711–726, Nov. 2017. DOI: 10.1007/s00190-017-1090-2.
- [39] O. Montenbruck, S. Hackel, M. Wermuth, and F. Zangerl, "Sentinel-6A precise orbit determination using a combined GPS/Galileo receiver," *Journal of Geodesy*, vol. 95, no. 9, Sep. 2021. DOI: 10.1007/s00190-021-01563-z.
- [40] S. A. FRANK, "The common patterns of nature," *Journal of Evolutionary Biology*, vol. 22, no. 8, pp. 1563–1585, Jul. 2009. DOI: 10.1111/j.1420-9101.2009.01775.x.

66 Bibliography

[41] P. V. S. R. Rao, S. G. Krishna, J. V. Prasad, S. N. V. S. Prasad, D. S. V. V. D. Prasad, and K. Niranjan, "Geomagnetic storm effects on GPS based navigation," *Annales Geophysicae*, vol. 27, no. 5, pp. 2101–2110, May 2009. DOI: 10.5194/angeo-27-2101-2009.

[42] R. Warnant, I. Kutiev, P. Marinov, M. Bavier, and S. Lejeune, "Ionospheric and geomagnetic conditions during periods of degraded GPS position accuracy: 1. monitoring variability in TEC which degrades the accuracy of real-time kinematic GPS applications," *Advances in Space Research*, vol. 39, no. 5, pp. 875–880, 2007. DOI: 10.1016/j.asr.2006.03.044.



APPENDIX

The Discrete Fourier Transform (DFT) of the auto-correlation plots of parameters are plotted in figures A.1, A.2, A.3, A.4, A.5, and A.6. The x-axis represents the lag in days and the amplitude of the DFT in y-axis.

The tables A.1, A.2, A.3, A.4, A.5, and A.6 show the correlation across all parameters of each satellite.

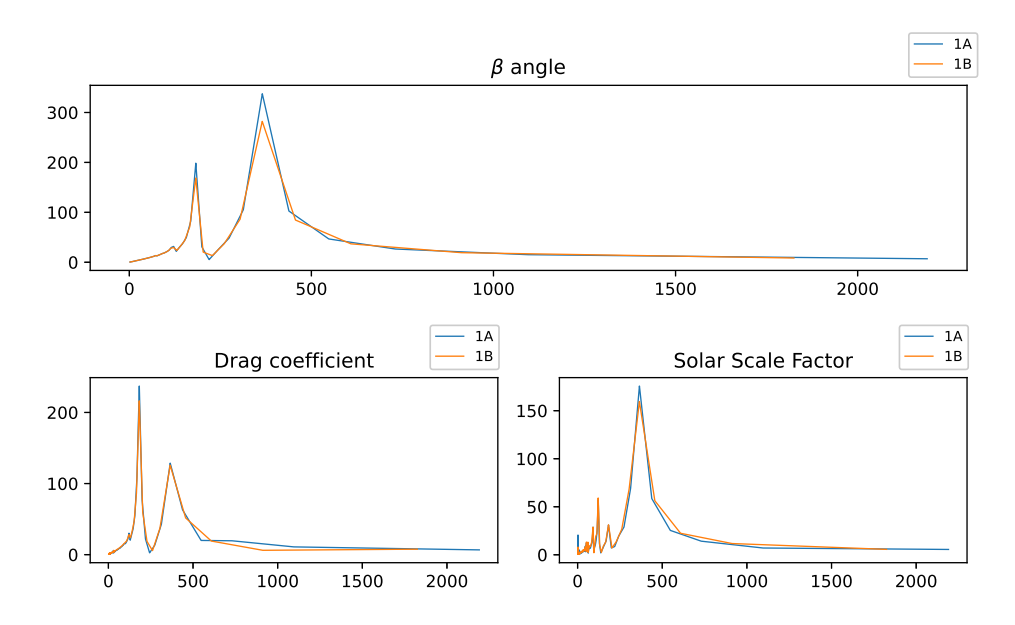


Figure A.1: Periodgram plots for the β angle, drag coefficient, and solar scale factor of Sentinel 1 satellites

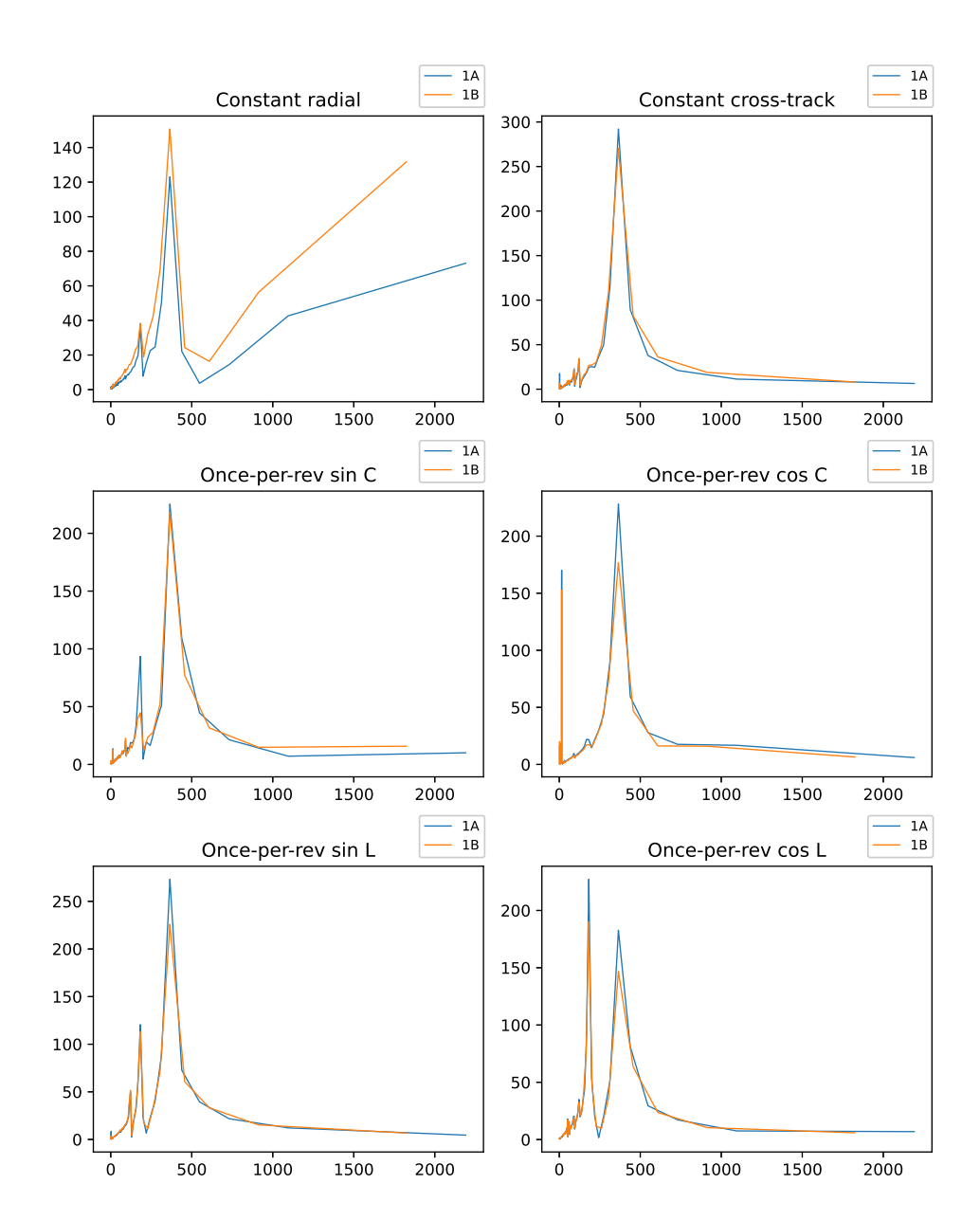


Figure A.2: Periodgram plots for the empirical acceleration of Sentinel 1 satellites

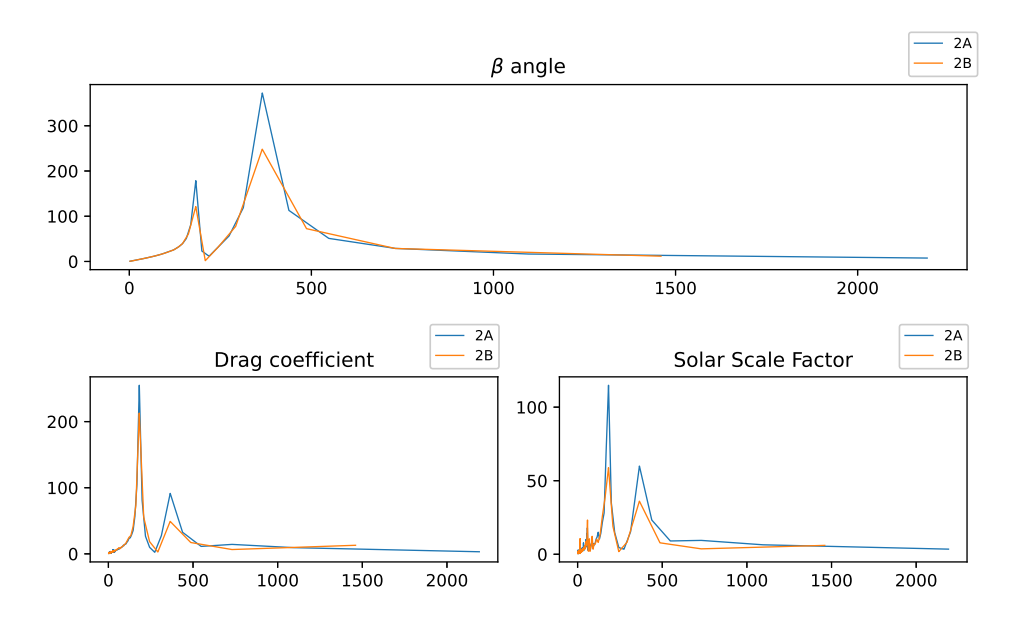


Figure A.3: Periodgram plots for the β angle, drag coefficient, and solar scale factor of Sentinel 2 satellites

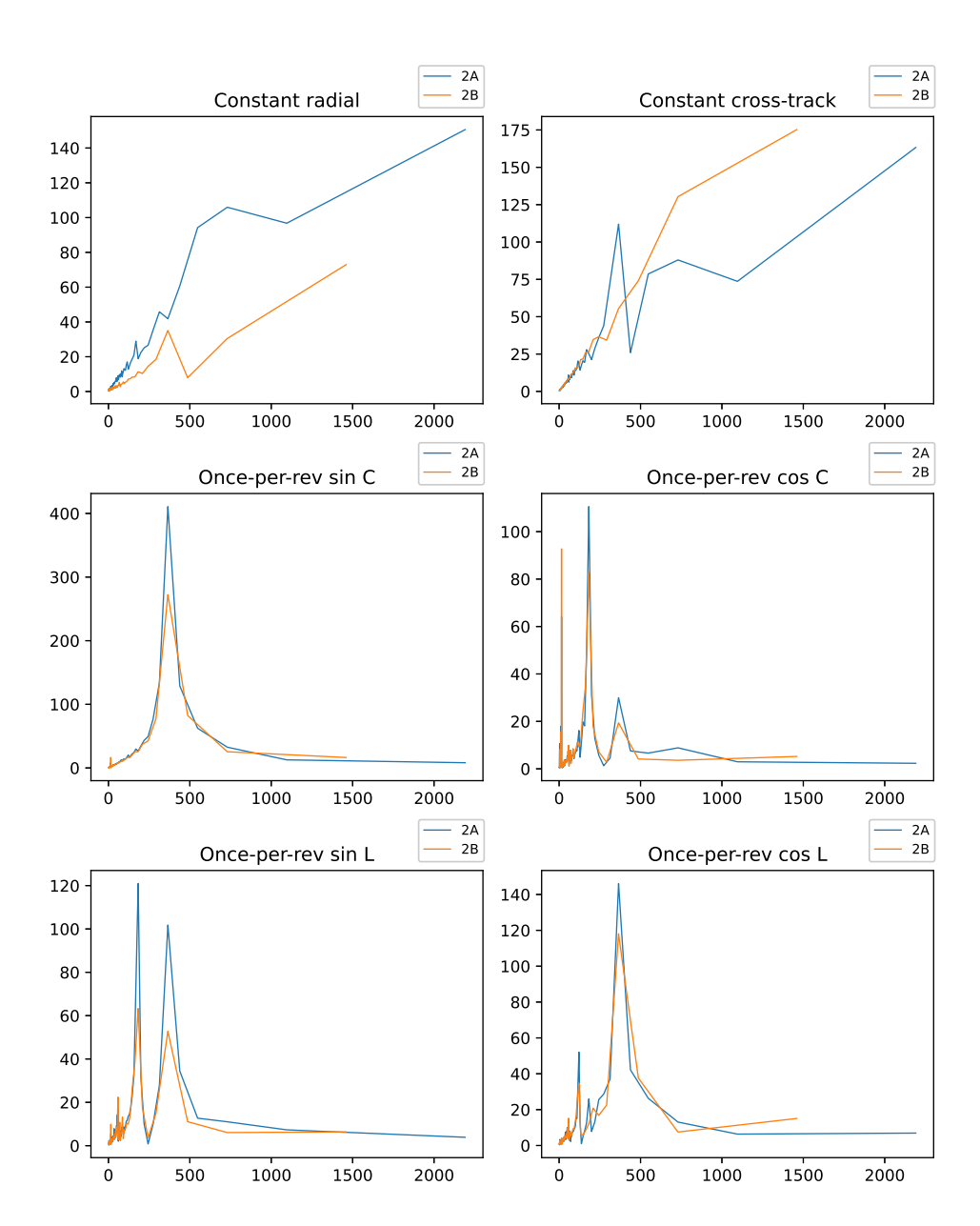


Figure A.4: Periodgram plots for the empirical acceleration of Sentinel 2 satellites

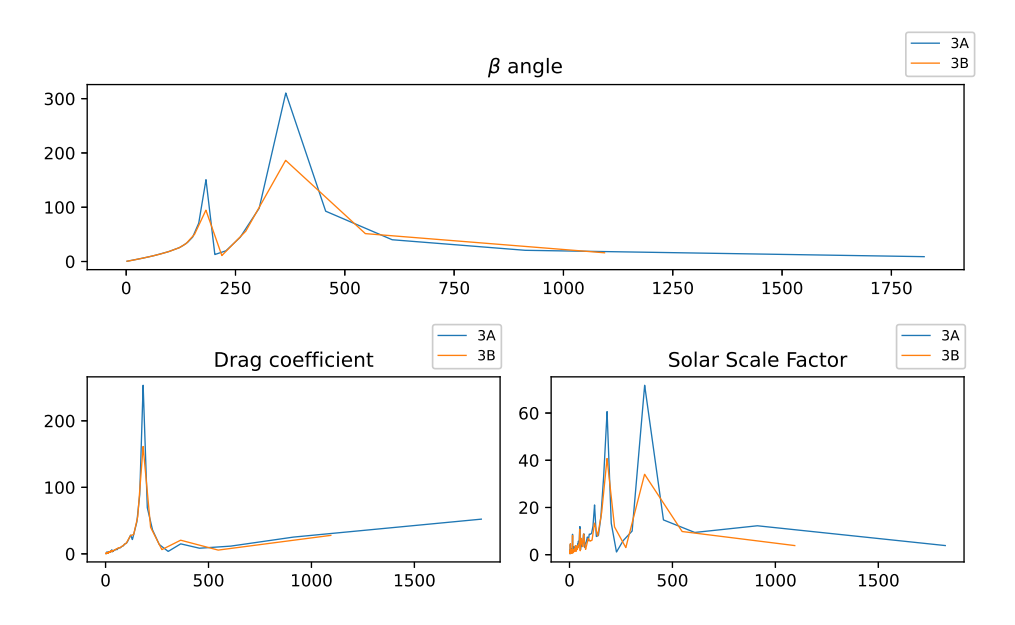


Figure A.5: Periodgram plots for the β angle, drag coefficient, and solar scale factor of Sentinel 3 satellites

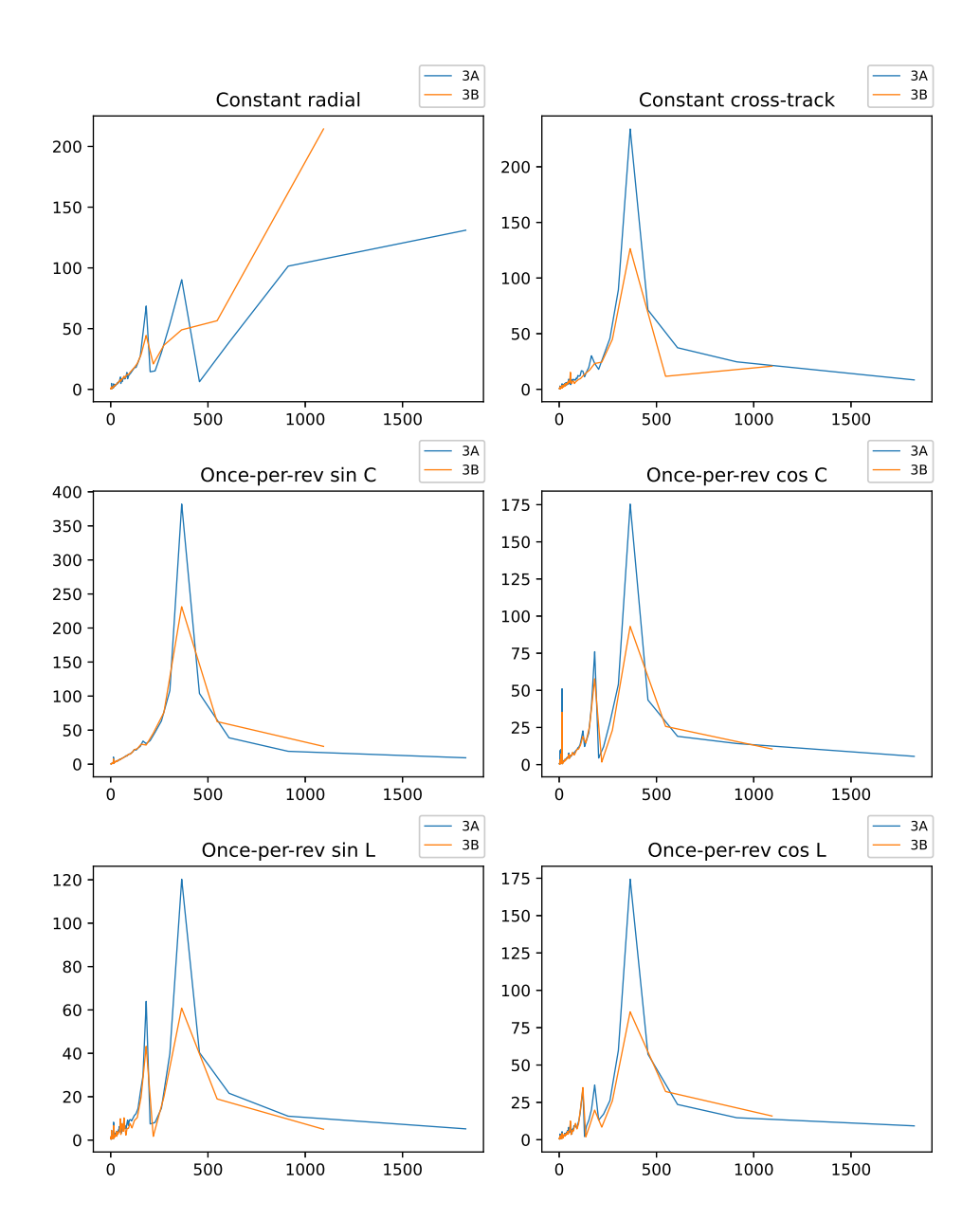


Figure A.6: Periodgram plots for the empirical acceleration of Sentinel 3 satellites

	%C	%P	C_rms	P_rms	β	Cd	f	Н	С
%C	1	.999**	.555**	368**	285**	-0.003	0.031	.050*	135**
%P	.999**	1	$.548^{**}$	388**	286**	-0.002	0.031	.041*	135**
C_rms	.555**	$.548^{**}$	1	0.010	-0.013	159**	057**	.151**	.043*
P_rms	368**	388**	0.010	1	052**	.080**	.047*	$.170^{**}$	048*
β	285**	286**	-0.013	052**	1	644**	287**	477**	.519**
Cd	-0.003	-0.002	159**	$.080^{**}$	644**	1	$.208^{**}$.378**	334**
f	0.031	0.031	057**	.047*	287**	.208**	1	.241**	948**
Н	.050*	.041*	$.151^{**}$	$.170^{**}$	477**	.378**	.241**	1	331**
С	135**	135**	.043*	048*	.519**	334**	948**	331**	1
SinC	0.003	0.003	0.027	173**	.251**	255**	167**	121**	.136**
CosC	054**	056**	074**	.212**	433**	.264**	.319**	.246**	415**
SinL	.199**	$.198^{**}$	$.092^{**}$	$.111^{**}$	389**	$.127^{**}$.266**	$.187^{**}$	380**
CosL	0.022	0.027	$.062^{**}$	156**	$.087^{**}$	$.097^{**}$	-0.021	065**	.181**
F10.7	771**	770**	609**	.316**	$.057^{**}$	$.099^{**}$	0.001	0.013	0.029
Mg_II	745**	743**	695**	.239**	-0.027	.248**	$.052^{**}$	0.011	042*
S10	626**	623**	582**	$.192^{**}$.072**	.151**	-0.029	0.011	.048*
Ap	391**	391**	151**	$.186^{**}$	$.104^{**}$	393**	0.013	056**	0.002
R	613**	611**	550**	.201**	-0.003	$.097^{**}$	0.006	0.019	-0.003

^{**.} Correlation is significant at the 0.01 level (2-tailed).

^{*.} Correlation is significant at the 0.05 level (2-tailed).

	SinC	CosC	SinL	CosL	F10.7	Mg_II	S10	Ap	R
%C	0.003	054**	.199**	0.022	771**	745**	626**	391**	613**
%P	0.003	056**	$.198^{**}$	0.027	770**	743**	623**	391**	611**
C_rms	0.027	074**	$.092^{**}$.062**	609**	695**	582**	151**	550**
P_rms	173**	.212**	.111**	156**	.316**	.239**	$.192^{**}$	$.186^{**}$.201**
β	.251**	433**	389**	$.087^{**}$	$.057^{**}$	-0.027	$.072^{**}$	$.104^{**}$	-0.003
Cd	255**	$.264^{**}$	$.127^{**}$	$.097^{**}$	$.099^{**}$.248**	$.151^{**}$	393**	.097**
f	167**	.319**	.266**	-0.021	0.001	$.052^{**}$	-0.029	0.013	0.006
Н	121**	.246**	$.187^{**}$	065**	0.013	0.011	0.011	056**	0.019
C	.136**	415**	380**	$.181^{**}$	0.029	042*	.048*	0.002	-0.003
SinC	1	197**	302**	351**	-0.015	-0.004	074**	$.078^{**}$	-0.017
CosC	197**	1	.503**	316**	$.126^{**}$	$.167^{**}$.047*	$.070^{**}$.132**
SinL	302**	.503**	1	385**	073**	068**	085**	-0.012	-0.027
CosL	351**	316**	385**	1	087**	109**	050*	149**	126**
F10.7	-0.015	.126**	073**	087**	1	.926**	$.759^{**}$	$.196^{**}$.884**
Mg_II	-0.004	$.167^{**}$	068**	109**	.926**	1	$.746^{**}$	$.137^{**}$.834**
S10	074**	.047*	085**	050*	$.759^{**}$	$.746^{**}$	1	.201**	.705**
Ap	.078**	$.070^{**}$	-0.012	149**	$.196^{**}$	$.137^{**}$.201**	1	.189**
R	-0.017	.132**	-0.027	126**	.884**	.834**	.705**	.189**	1

^{**.} Correlation is significant at the 0.01 level (2-tailed).

Table A.1: Correlation matrix for Sentinel 1A

^{*.} Correlation is significant at the 0.05 level (2-tailed).

74

	%C	%P	C_rms	P_rms	β	Cd	f	Н	С
%C	1	.995**	.248**	.270**	343**	.258**	.151**	.339**	257**
%P	.995**	1	$.197^{**}$.208**	369**	$.290^{**}$	$.167^{**}$	$.327^{**}$	277**
C_rms	.248**	$.197^{**}$	1	$.659^{**}$.128**	245**	058*	.382**	.085**
P_rms	.270**	.208**	$.659^{**}$	1	225**	.045	.004	.587**	079**
β	343**	369**	.128**	225**	1	784**	316**	575**	.561**
Cd	.258**	$.290^{**}$	245**	.045	784**	1	.249**	.383**	432**
f	.151**	$.167^{**}$	058*	.004	316**	.249**	1	.285**	941**
Н	.339**	$.327^{**}$.382**	$.587^{**}$	575**	.383**	.285**	1	440**
С	257**	277**	.085**	079**	.561**	432**	941**	440**	1
SinC	148**	158**	.019	176**	.328**	223**	236**	140**	.245**
CosC	.223**	.231**	023	$.120^{**}$	454**	$.270^{**}$.310**	.306**	426**
SinL	.290**	.281**	.050*	$.220^{**}$	345**	.125**	.253**	.223**	364**
CosL	175**	167**	011	002	.073**	$.129^{**}$.044	186**	$.134^{**}$
F10.7	405**	378**	446**	367**	$.084^{**}$.011	077**	319**	.103**
Mg_II	368**	319 ^{**}	676**	610**	085**	.236**	.039	352**	051*
S10	332**	292**	462**	354**	.001	$.186^{**}$.007	222**	.004
Ap	391**	397**	.016	.053*	$.116^{**}$	412**	.009	.032	.003
R	330**	297**	414**	332**	012	.058*	009	227**	.006

^{**.} Correlation is significant at the 0.01 level (2-tailed).

^{*.} Correlation is significant at the 0.05 level (2-tailed).

	SinC	CosC	SinL	CosL	F10.7	Mg_II	S10	Ap	R
%C	148**	.223**	.290**	175**	405**	368**	332**	391**	330**
%P	158**	.231**	.281**	167**	378**	319**	292**	397**	297**
C_rms	.019	023	.050*	011	446**	676**	462**	.016	414**
P_rms	176**	.120**	.220**	002	367**	610**	354**	.053*	332**
β	.328**	454**	345**	.073**	$.084^{**}$	085**	.001	$.116^{**}$	012
Cd	223**	.270**	.125**	$.129^{**}$.011	.236**	$.186^{**}$	412**	.058*
f	236**	.310**	.253**	.044	077**	.039	.007	.009	009
H	140**	.306**	.223**	186**	319**	352**	222**	.032	227**
C	.245**	426**	364**	$.134^{**}$.103**	051*	.004	.003	.006
SinC	1	276**	487**	239**	.056*	$.076^{**}$	131**	.054*	015
CosC	276**	1	$.472^{**}$	262**	068**	017	053*	.035	.022
SinL	487**	$.472^{**}$	1	347**	147**	163**	091**	.020	049*
CosL	239**	262**	347**	1	$.076^{**}$.039	.151**	140**	001
F10.7	.056*	068**	147**	$.076^{**}$	1	.813**	.626**	$.129^{**}$.864**
Mg_II	.076**	017	163**	.039	.813**	1	$.674^{**}$.058*	.763**
S10	131**	053*	091**	.151**	.626**	$.674^{**}$	1	$.098^{**}$.614**
Ap	.054*	.035	.020	140**	.129**	.058*	$.098^{**}$	1	.153**
R	015	.022	049*	001	.864**	.763**	.614**	.153**	1

^{**.} Correlation is significant at the 0.01 level (2-tailed).

Table A.2: Correlation matrix for Sentinel 1B

^{*.} Correlation is significant at the 0.05 level (2-tailed).

	%C	%P	C_rms	P_rms	β	Cd	f	Н	С
%C	1	.997**	.315**	.040	229**	028	.067**	.039	.107**
%P	.997**	1	$.279^{**}$	009	241**	040	$.079^{**}$.027	.076**
C_rms	.315**	$.279^{**}$	1	$.474^{**}$	088**	072**	.054*	$.471^{**}$.457**
P_rms	.040	009	$.474^{**}$	1	.206**	$.064^{**}$	129**	.318**	.432**
β	229**	241**	088**	.206**	1	.362**	193**	.237**	.166**
Cd	028	040	072**	$.064^{**}$.362**	1	425**	056**	.129**
f	.067**	$.079^{**}$.054*	129**	193**	425**	1	.220**	359**
Н	.039	.027	$.471^{**}$.318**	.237**	056**	.220**	1	$.140^{**}$
С	.107**	$.076^{**}$	$.457^{**}$.432**	$.166^{**}$	$.129^{**}$	359**	$.140^{**}$	1
SinC	041	054*	.042	.005	281**	023	188**	180**	.195**
CosC	002	.002	.009	059**	.263**	194**	.552**	.272**	229**
SinL	.122**	.135**	$.078^{**}$	159**	324**	486**	$.981^{**}$	$.196^{**}$	382**
CosL	.196**	.202**	.038	010	104**	.053*	.173**	.002	095**
F10.7	370**	344**	504**	353**	.092**	.037	041	123**	304**
Mg_II	350**	321**	618**	451**	088**	$.091^{**}$	032	385**	370**
S10	400**	365**	574**	405**	$.089^{**}$.086**	016	034	541**
Ap	364**	356**	115**	064**	.023	466**	$.104^{**}$.053*	102**
R	320**	292**	478**	359**	.012	.014	020	174**	308**

^{**.} Correlation is significant at the 0.01 level (2-tailed).

^{*.} Correlation is significant at the 0.05 level (2-tailed).

	SinC	CosC	SinL	CosL	F10.7	Mg_II	S10	Ap	R
%C	041	002	.122**	.196**	370**	350**	400**	364**	320**
%P	054*	.002	.135**	.202**	344**	321**	365**	356**	292**
C_rms	.042	.009	$.078^{**}$.038	504**	618**	574**	115**	478**
P_rms	.005	059**	159**	010	353**	451**	405**	064**	359**
β	281**	.263**	324**	104**	$.092^{**}$	088**	$.089^{**}$.023	.012
Cd	023	194**	486**	.053*	.037	$.091^{**}$	$.086^{**}$	466**	.014
f	188**	.552**	.981**	.173**	041	032	016	$.104^{**}$	020
Н	180**	.272**	$.196^{**}$.002	123**	385**	034	.053*	174**
С	.195**	229**	382**	095**	304**	370**	541**	102**	308**
SinC	1	231**	160**	513**	.050*	$.146^{**}$	024	.007	.035
CosC	231**	1	.505**	.005	.000	077**	$.057^{**}$	$.099^{**}$	015
SinL	160**	.505**	1	$.194^{**}$	063**	039	038	.093**	028
CosL	513**	.005	$.194^{**}$	1	126**	089**	116**	136**	072**
F10.7	.050*	.000	063**	126**	1	$.854^{**}$	$.741^{**}$.163**	.854**
Mg_II	.146**	077**	039	089**	$.854^{**}$	1	.713**	$.099^{**}$.793**
S10	024	$.057^{**}$	038	116**	.741**	.713**	1	.163**	.642**
Ap	.007	$.099^{**}$	$.093^{**}$	136**	.163**	$.099^{**}$.163**	1	.161**
R	.035	015	028	072**	.854**	.793**	.642**	.161**	1

^{**.} Correlation is significant at the 0.01 level (2-tailed).

Table A.3: Correlation matrix of Sentinel 2A

^{*.} Correlation is significant at the 0.05 level (2-tailed).

	%C	%P	C_rms	P_rms	β	Cd	f	Н	С
%C	1	.776**	.180**	085**	100**	080**	.096**	.097**	072**
%P	.776**	1	020	490**	078**	087**	.136**	410**	.042
C_rms	.180**	020	1	.055*	.112**	.005	074**	.570**	.064*
P_rms	085**	490**	.055*	1	$.154^{**}$	$.118^{**}$	186**	.445**	372**
β	100**	078**	.112**	$.154^{**}$	1	$.302^{**}$	064*	.269**	.050
Cd	080**	087**	.005	$.118^{**}$.302**	1	364**	.020	.085**
f	.096**	$.136^{**}$	074**	186**	064*	364**	1	.024	103**
Н	.097**	410**	$.570^{**}$	$.445^{**}$.269**	.020	.024	1	108**
C	072**	.042	.064*	372**	.050	.085**	103**	108**	1
SinC	129**	.007	134**	092**	219**	.058*	217**	281**	$.194^{**}$
CosC	.097**	036	$.077^{**}$.066*	.338**	136**	$.504^{**}$.291**	154**
SinL	.132**	$.126^{**}$	045	180**	201**	423**	$.978^{**}$.047	118**
CosL	.168**	.065*	$.077^{**}$	$.107^{**}$	191**	113**	$.104^{**}$.055*	250**
F10.7	325**	239**	541**	$.115^{**}$.042	.240**	063*	276**	$.096^{**}$
Mg_II	280**	201**	666**	$.069^{**}$	188**	$.199^{**}$	029	425**	.085**
S10	201**	135**	539**	094**	156**	.226**	.026	311**	.224**
Ap	218**	156**	050	069**	.029	459**	.120**	025	.112**
R	253**	180**	483**	004	059*	$.150^{**}$	018	265**	$.147^{**}$

^{**.} Correlation is significant at the 0.01 level (2-tailed).

^{*.} Correlation is significant at the 0.05 level (2-tailed).

	SinC	CosC	SinL	CosL	F10.7	Mg_II	S10	Ap	R
%C	129**	.097**	.132**	.168**	325**	280**	201**	218**	253**
%P	.007	036	$.126^{**}$.065*	239**	201**	135**	156**	180**
C_rms	134**	$.077^{**}$	045	$.077^{**}$	541**	666**	539**	050	483**
P_rms	092**	.066*	180**	$.107^{**}$.115**	$.069^{**}$	094**	069**	004
β	219**	.338**	201**	191**	.042	188**	156**	.029	059*
Cd	.058*	136**	423**	113**	$.240^{**}$	$.199^{**}$.226**	459**	$.150^{**}$
f	217**	.504**	$.978^{**}$	$.104^{**}$	063*	029	.026	.120**	018
Н	281**	.291**	.047	.055*	276**	425**	311**	025	265**
C	.194**	154**	118**	250**	$.096^{**}$.085**	$.224^{**}$.112**	$.147^{**}$
SinC	1	245**	207**	536**	$.167^{**}$.220**	.034	.019	.113**
CosC	245**	1	$.470^{**}$	010	113**	149**	098**	.065*	106**
SinL	207**	$.470^{**}$	1	$.151^{**}$	113**	046	.017	$.106^{**}$	043
CosL	536**	010	.151**	1	159**	096**	008	107**	103**
F10.7	.167**	113**	113**	159**	1	.882**	.752**	.040	.876**
Mg_II	.220**	149**	046	096**	.882**	1	.813**	.043	.808**
S10	.034	098**	.017	008	.752**	.813**	1	.049	$.719^{**}$
Ap	.019	.065*	$.106^{**}$	107**	.040	.043	.049	1	$.074^{**}$
R	.113**	106**	043	103**	.876**	.808**	.719**	.074**	1

^{**.} Correlation is significant at the 0.01 level (2-tailed).

Table A.4: Correlation matrix of Sentinel 2B

^{*.} Correlation is significant at the 0.05 level (2-tailed).

	%C	%P	C_rms	P_rms	β	Cd	f	Н	С
%C	1	.998**	017	028	.014	.037	.019	.073**	005
%P	.998**	1	018	042	.011	.034	.016	$.065^{**}$	007
C_rms	017	018	1	186**	.138**	108**	050*	.244**	.011
P_rms	028	042	186**	1	.209**	.022	$.119^{**}$	288**	.330**
β	.014	.011	.138**	.209**	1	368**	.340**	.463**	.306**
Cd	.037	.034	108**	.022	368**	1	300**	336**	079**
f	.019	.016	050*	.119**	$.340^{**}$	300**	1	$.403^{**}$	227**
Н	.073**	$.065^{**}$	$.244^{**}$	288**	$.463^{**}$	336**	$.403^{**}$	1	.049*
С	005	007	.011	.330**	.306**	079**	227**	.049*	1
SinC	032	035	029	.320**	$.097^{**}$.055*	139**	018	.627**
CosC	.041	.038	.017	$.167^{**}$	$.671^{**}$	367**	.685**	$.504^{**}$	$.143^{**}$
SinL	.003	.004	140**	152**	451**	047*	$.650^{**}$.032	581**
CosL	.055*	.053*	.003	.260**	$.299^{**}$.022	.311**	$.148^{**}$	$.169^{**}$
F10.7	.045*	.031	354**	.395**	051*	.212**	.045*	094**	$.096^{**}$
Mg_II	.022	.014	487**	.495**	249**	.360**	025	396**	004
S10	.095**	$.080^{**}$	423**	$.146^{**}$	160**	.372**	.019	.048*	062**
Ap	.045*	.025	034	.302**	.019	367**	$.092^{**}$	$.145^{**}$	007
R	.044*	.032	321**	.321**	091**	.234**	.039	107**	.002

^{**.} Correlation is significant at the 0.01 level (2-tailed).

^{*.} Correlation is significant at the 0.05 level (2-tailed).

	SinC	CosC	SinL	CosL	F10.7	Mg_II	S10	Ap	R
%C	032	.041	.003	.055*	.045*	.022	.095**	.045*	.044*
%P	035	.038	.004	.053*	.031	.014	.080**	.025	.032
C_rms	029	.017	140**	.003	354**	487**	423**	034	321**
P_rms	.320**	$.167^{**}$	152**	.260**	.395**	$.495^{**}$	$.146^{**}$.302**	.321**
β	.097**	.671**	451**	.299**	051*	249**	160**	.019	091**
Cd	.055*	367**	047*	.022	.212**	$.360^{**}$.372**	367**	.234**
f	139**	.685**	$.650^{**}$.311**	.045*	025	.019	$.092^{**}$.039
Н	018	.504**	.032	$.148^{**}$	094**	396**	.048*	$.145^{**}$	107**
С	.627**	.143**	581**	$.169^{**}$	$.096^{**}$	004	062**	007	.002
SinC	1	.112**	362**	170**	$.126^{**}$.152**	.028	.015	.048*
CosC	.112**	1	$.091^{**}$	$.247^{**}$.008	131**	038	.081**	033
SinL	362**	$.091^{**}$	1	.013	.051*	.128**	$.128^{**}$	$.071^{**}$.095**
CosL	170**	.247**	.013	1	.039	013	.042	063**	.018
F10.7	.126**	.008	.051*	.039	1	.824**	.663**	$.157^{**}$.849**
Mg_II	.152**	131**	.128**	013	.824**	1	$.647^{**}$.081**	.771**
S10	.028	038	$.128^{**}$.042	.663**	$.647^{**}$	1	$.169^{**}$.616**
Ap	.015	$.081^{**}$.071**	063**	$.157^{**}$.081**	$.169^{**}$	1	.153**
R	.048*	033	.095**	.018	.849**	.771**	.616**	.153**	1

^{**.} Correlation is significant at the 0.01 level (2-tailed).

Table A.5: Correlation matrix of Sentinel 3A

^{*.} Correlation is significant at the 0.05 level (2-tailed).

	%C	%P	C_rms	P_rms	β	Cd	f	Н	С
%C	1	.998**	048	.040	.028	025	015	006	.023
%P	.998**	1	049	.022	.021	027	017	010	.019
C_rms	048	049	1	326**	.251**	236**	041	$.648^{**}$.017
P_rms	.040	.022	326**	1	$.154^{**}$.264**	.093**	392**	$.347^{**}$
β	.028	.021	.251**	$.154^{**}$	1	375**	.322**	.385**	.257**
Cd	025	027	236**	.264**	375**	1	349**	413**	.024
f	015	017	041	.093**	.322**	349**	1	.217**	227**
Н	006	010	.648**	392**	.385**	413**	.217**	1	.038
C	.023	.019	.017	$.347^{**}$.257**	.024	227**	.038	1
SinC	.006	.003	.091**	.335**	.123**	$.144^{**}$	060*	.064*	.636**
CosC	.028	.024	$.094^{**}$	$.116^{**}$.644**	417**	$.674^{**}$.325**	.103**
SinL	031	026	216**	135**	452**	105**	.668**	064*	522**
CosL	.056	.053	001	.230**	.273**	004	.073*	032	$.191^{**}$
F10.7	.026	.019	482**	$.676^{**}$.050	.351**	$.094^{**}$	451**	.239**
Mg_II	.040	.035	642**	.668**	183**	$.461^{**}$.009	665**	.113**
S10	.043	.037	639**	$.664^{**}$	177**	$.440^{**}$.018	657**	$.077^{**}$
Ap	.037	.028	034	.315**	.062*	369**	.151**	007	.000
R	.031	.027	476**	$.550^{**}$	063*	.334**	.063*	429**	$.116^{**}$

^{**.} Correlation is significant at the 0.01 level (2-tailed).

^{*.} Correlation is significant at the 0.05 level (2-tailed).

	SinC	CosC	SinL	CosL	F10.7	Mg_II	S10	Ap	R
%C	.006	.028	031	.056	.026	.040	.043	.037	.031
%P	.003	.024	026	.053	.019	.035	.037	.028	.027
C_rms	.091**	$.094^{**}$	216**	001	482**	642**	639**	034	476**
P_rms	.335**	$.116^{**}$	135**	.230**	$.676^{**}$.668**	.664**	.315**	.550**
β	.123**	.644**	452**	.273**	.050	183**	177**	.062*	063*
Cd	.144**	417**	105**	004	.351**	$.461^{**}$	$.440^{**}$	369**	.334**
f	060*	$.674^{**}$.668**	.073*	$.094^{**}$.009	.018	$.151^{**}$.063*
Н	.064*	.325**	064*	032	451**	665**	657**	007	429**
C	.636**	.103**	522**	$.191^{**}$.239**	.113**	$.077^{**}$.000	$.116^{**}$
SinC	1	$.172^{**}$	292**	174**	$.274^{**}$	$.193^{**}$	$.127^{**}$.018	.155**
CosC	.172**	1	.125**	.065*	.072*	078**	088**	$.109^{**}$	002
SinL	292**	.125**	1	147**	028	$.082^{**}$	$.096^{**}$.088**	.059*
CosL	174**	.065*	147**	1	.132**	.040	$.092^{**}$	052	.057
F10.7	.274**	.072*	028	$.132^{**}$	1	.885**	.840**	.070*	.886**
Mg_II	.193**	078**	$.082^{**}$.040	.885**	1	$.945^{**}$.083**	.830**
S10	.127**	088**	$.096^{**}$	$.092^{**}$	$.840^{**}$	$.945^{**}$	1	$.089^{**}$.803**
Ap	.018	$.109^{**}$.088**	052	.070*	.083**	.089**	1	.082**
R	.155**	002	.059*	.057	.886**	.830**	.803**	.082**	1

^{**.} Correlation is significant at the 0.01 level (2-tailed).

Table A.6: Correlation matrix of Sentinel 3B

^{*.} Correlation is significant at the 0.05 level (2-tailed).